NBS SPECIAL PUBLICATION 400-38

U.S. DEPARTMENT OF COMMERCE / National Bureau of Standards

Semiconductor Measurement Technology

Progress Report
October 1, 1976 to March 31, 1977

NATIONAL BUREAU OF STANDARDS

The National Bureau of Standards[1] was established by an act of Congress on March 3, 1901. The Bureau's overall goal is to strengthen and advance the Nation's science and technology and facilitate their effective application for public benefit. To this end, the Bureau conducts research and provides: (1) a basis for the Nation's physical measurement system, (2) scientific and technological services for industry and government, (3) a technical basis for equity in trade, and (4) technical services to promote public safety. The Bureau's technical work is performed by the National Measurement Laboratory, the National Engineering Laboratory, and the Institute for Computer Sciences and Technology.

THE NATIONAL MEASUREMENT LABORATORY provides the national system of physical and chemical and materials measurement; coordinates the system with measurement systems of other nations and furnishes essential services leading to accurate and uniform physical and chemical measurement throughout the Nation's scientific community, industry, and commerce; conducts materials research leading to improved methods of measurement, standards, and data on the properties of materials needed by industry, commerce, educational institutions, and Government; provides advisory and research services to other Government agencies; develops, produces, and distributes Standard Reference Materials; and provides calibration services. The Laboratory consists of the following centers:

Absolute Physical Quantities[2] — Radiation Research — Thermodynamics and Molecular Science — Analytical Chemistry — Materials Science.

THE NATIONAL ENGINEERING LABORATORY provides technology and technical services to the public and private sectors to address national needs and to solve national problems; conducts research in engineering and applied science in support of these efforts; builds and maintains competence in the necessary disciplines required to carry out this research and technical service; develops engineering data and measurement capabilities; provides engineering measurement traceability services; develops test methods and proposes engineering standards and code changes; develops and proposes new engineering practices; and develops and improves mechanisms to transfer results of its research to the ultimate user. The Laboratory consists of the following centers:

Applied Mathematics — Electronics and Electrical Engineering[2] — Mechanical Engineering and Process Technology[2] — Building Technology — Fire Research — Consumer Product Technology — Field Methods.

THE INSTITUTE FOR COMPUTER SCIENCES AND TECHNOLOGY conducts research and provides scientific and technical services to aid Federal agencies in the selection, acquisition, application, and use of computer technology to improve effectiveness and economy in Government operations in accordance with Public Law 89-306 (40 U.S.C. 759), relevant Executive Orders, and other directives; carries out this mission by managing the Federal Information Processing Standards Program, developing Federal ADP standards guidelines, and managing Federal participation in ADP voluntary standardization activities; provides scientific and technological advisory services and assistance to Federal agencies; and provides the technical foundation for computer-related policies of the Federal Government. The Institute consists of the following centers:

Programming Science and Technology — Computer Systems Engineering.

[1]Headquarters and Laboratories at Gaithersburg, MD, unless otherwise noted; mailing address Washington, DC 20234.
[2]Some divisions within the center are located at Boulder, CO 80303.

Semiconductor Measurement Technology
October 1, 1976 to March 31, 1977

W. Murray Bullis, Editor

Electron Devices Division
Center for Electronics and Electrical Engineering
National Engineering Laboratory
National Bureau of Standards
Washington, D.C. 20234

Jointly supported by:
The National Bureau of Standards
The Navy Strategic Systems Projects Office
The Defense Nuclear Agency
The Defense Advanced Research Projects Agency
The Energy Research and Development Administration, and
The Naval Ocean Systems Center

U.S. DEPARTMENT OF COMMERCE
Luther H. Hodges, Jr., Under Secretary
Jordan J. Baruch, Assistant Secretary for Science and Technology
NATIONAL BUREAU OF STANDARDS, Ernest Ambler, Director

Issued November 1979

National Bureau of Standards Special Publication 400-38
Nat. Bur. Stand. (U.S.), Spec. Publ. 400-38, 95 pages (Nov. 1979)
CODEN: XNBSAV

U.S. GOVERNMENT PRINTING OFFICE
WASHINGTON: 1979

For sale by the Superintendent of Documents, U.S. Government Printing Office, Washington, D.C. 20402
Stock No. 003-003-02139-3 Price $3.50

(Add 25 percent additional for other than U.S. mailing).

☆ U.S. GOVERNMENT PRINTING OFFICE: 1979 O—311-065 (272)

TABLE OF CONTENTS

SEMICONDUCTOR MEASUREMENT TECHNOLOGY

LIST OF FIGURES

LIST OF FIGURES

LIST OF TABLES

PREFACE

The Semiconductor Technology Program serves to focus NBS research to enhance the performance, interchangeability, and reliability of discrete semiconductor devices and integrated circuits through improvements in measurement technology for use in specifying materials and devices in national and international commerce and for use by industry in controlling device fabrication processes. This research leads to carefully evaluated and well documented test procedures and associated technology. Special emphasis is placed on the dissemination of the results of the research to the electronics community. Application of these results by industry will contribute to higher yields, lower cost, and higher reliability of semiconductor devices. Improved measurement technology also leads to greater economy in government procurement by providing a common basis for the purchase specifications of government agencies, and, in addition, provides a basis for controlled improvements in fabrication processes and in essential device characteristics.

During this reporting period, the Program received direct financial support principally from two major sponsors: the Defense Advanced Research Projects Agency (ARPA)* and the National Bureau of Standards (NBS).† In addition, the Program received support from the Defense Nuclear Agency (DNA),§ the Navy Strategic Systems Project Office,¶ the Energy Research and Development Administration,# and the Naval Ocean Systems Center.× The ARPA-supported portion of the Program, Advancement of Reliability, Processing, and Automation for Integrated Circuits with the National Bureau of Standards (ARPA/IC/NBS), addresses critical Defense Department problems in the yield, reliability, and availability of digital monolithic integrated circuits. Other portions of the Program emphasize aspects of the work which relate to the specific needs of the supporting agency. Measurement-oriented research appropriate to the mission of NBS is an essential aspect in all parts of the Program.

Essential assistance to the Program is also received from the semiconductor industry through cooperative experiments and technical exchanges. NBS interacts with industrial users and suppliers of semiconductor devices through participation in standardizing organizations; through direct consultations with device and material suppliers, government agencies, and other users; and through scheduled symposia and workshops. In addition to progress reports such as this one, more detailed reports such as state-of-the-art reviews, literature compilations, and summaries of technical efforts conducted within the Program are issued as these activities are completed. Reports of this type which are published by NBS appear in the NBS Special Publication 400 subseries.

Another means of interaction with the electronics community is by direct contact. In particular, comments from readers regarding the usefulness of the results reported herein or relating to directions of future activity in the Program are always welcome.

Disclaimer

Certain commercially available materials or instruments are identified in this publication for the purpose of providing a complete description of the work performed. The experiments reported do not constitute a complete evaluation of the performance characteristics of the products so identified. In no case does such identification imply recommendation or endorsement by the National Bureau of Standards nor does it imply that the items identified are necessarily the best available for the purpose.

---

* Through ARPA Order 2397, Program Code 7D10 (NBS Cost Center 4257555). Unless otherwise noted, work was funded from this source.

† Principally through the Electronic Technology Program (Cost Center 4257100). Additional funding through the Dimensional Metrology Program (Cost Center 2131119).

§ Through Inter-Agency Cost Reimbursement Order 77-809 (NBS Cost Center 4259522).

¶ Code SP-23, through project order N0016476WR70036 administered by Naval Weapons Support Center, Crane, Indiana (NBS Cost Center 4251533).

Through ERDA Task Order A021-EES (NBS Cost Center 4259561).

× Through Order N0095377M009005 (NBS Cost Center 4259563).

SEMICONDUCTOR MEASUREMENT TECHNOLOGY

PROGRESS REPORT
October 1, 1976 to March 31, 1977

Abstract: This progress report describes NBS activities directed toward the development of methods of measurement for semiconductor materials, process control, and devices. Both in-house and contract efforts are included. The emphasis is on silicon device technologies. Principal accomplishments during this reporting period included (1) refinement and extension of the analysis of the nondestructive, photovoltaic method for measuring radial resistivity variation of silicon slices; (2) development of a donor-addition technique for testing for the presence of X-levels in indium-doped silicon; (3) development of a precision, wet chemical etching procedure for use in conjunction with x-ray photoelectron spectroscopy for profiling silicon dioxide-silicon interfaces; (4) completion of thermodynamic calculations of equilibrium sodium density in oxidation atmospheres contained in polycrystalline silicon tubes; (5) initial extensions of the line-width measurement procedure to partially transparent and reflecting specimens and to submicrometer dimensions; and (6) completion of the development of a test pattern for characterizing a large-scale-integration, silicon-on-sapphire process. Also reported is other ongoing work on materials characterization by electrical and physical analysis methods, materials and procedures for wafer processing, photolithography, test patterns, and device inspection and test procedures. Supplementary data concerning staff and publications are included as appendices.

Key Words: Auger electron spectroscopy; die attachment; electrical properties; electronics; hermeticity; indium-doped silicon; infrared reflectance; integrated circuits; line-width measurements; oxidation; photolithography; photovoltaic method; power-device grade silicon; radioisotope leak test; resistivity variations; resistors, sheet; scanning acoustic microscope; semiconductor materials; semiconductor process control; silicon; silicon dioxide; silicon-on-sapphire; sodium contamination; test patterns; test structures; thermally stimulated current and capacitance; transistors; ultraviolet reflectance; $V_{CE(SAT)}$; x-ray photoelectron spectroscopy.

1. INTRODUCTION

This is a report to the sponsors of the Semiconductor Technology Program on work carried out during the thirty-fourth and thirty-fifth quarters of the Program. The report summarizes research on a wide variety of measurement methods for semiconductor materials, process control, and devices that are being studied at the National Bureau of Standards (NBS). The Program, which emphasizes silicon-based device technologies, is a continuing one, and the results and conclusions reported here are subject to modification and refinement.

The Program is divided into a number of task areas, each directed toward the study of a particular material or device property or measurement technique. This report is subdivided according to these tasks. Highlights of activity during the reporting period are given in section 2. This section provides a management-level overview of the entire effort. Subsequent sections deal with each specific task area. References cited are listed in the final section of the report.

The report of each task includes a narrative description of progress made during this reporting period. Additional information concerning the material reported may be obtained directly from individual staff members identified with the task in the report. Organizational locations for Program staff members at the end of the reporting period, listed in Appendix A, are given for record purposes only; many changes have occurred because of a reorganization of the NBS which took place on April 9, 1978.

Background material on the Program and individual tasks may be found in earlier progress reports as listed in Appendix B. From time to time, publications are prepared that describe some aspect of the program in greater detail. Because of the long delay between the end of the reporting period and the issuance of this report, reports of this type are not listed herein. A complete listing of publications issued by the Program is available in NBS List of Publications LP72, Semiconductor Measurement Technology, which can be obtained on request to Electron Devices Division, National Bureau of Standards, Washington, D.C. 20234; telephone (301) 921-3786.

This is the next to last of these comprehensive progress reports. Work carried out after October 1, 1977 is reported in condensed form under the title, Semiconductor Technology Program, Progress Briefs, in the NBSIR series. The work carried out between April 1 and September 30, 1977 will be reported in NBS Special Publication 400-45.

2. HIGHLIGHTS

Highlights of progress in the various technical task areas of the Program are listed in this section. Particularly significant accomplishments during this reporting period included:

(1) refinement and extension of the analysis of the nondestructive, photovoltaic method for measuring radial resistivity variation of silicon slices;

(2) development of a donor-addition technique for testing for the presence of X-levels in indium-doped silicon;

(3) development of a precision, wet chemical etching procedure for use in conjunction with x-ray photoelectron spectroscopy for profiling silicon dioxide-silicon interfaces;

(4) completion of thermodynamic calculations of equilibrium sodium density in oxidation atmospheres contained in polycrystalline silicon tubes;

(5) initial extensions of the line-width measurement procedure to partially transparent and reflecting specimens and to submicrometer dimensions; and

(6) completion of the development of a test pattern for characterizing a large-scale-integration, silicon-on-sapphire process.

Unless another organization is identified, the work described in the following paragraphs was performed at the National Bureau of Standards.

Materials Characterization by Electrical Methods — Automation of the photovoltaic scanning apparatus to measure radial resistivity variations of circular semiconductor slices was completed. It was found that the most repeatable results and profiles most like those determined by the four-probe method could be obtained on surfaces lapped with 12-μm aluminum grit. A spread of less than 3 percent of the average resistivity was obtained in a preliminary set of eight measurements made over a period of 4 days along the diameter of a single slice. This reproducibility is expected to be adequate for use in evaluating incoming float-zoned slices. The previous analysis of the photovoltaic and photoconductive signals was refined and extended. The algebraic simplification achieved through the use of a modified transformation equation made it possible to improve the treatment of the nature of the light spot in the analysis; it was found that the expression for the gradient of the resistivity along the scanning diameter should be 4/3 times the previously obtained expression. In addition, it was possible to derive expressions for cases where the current and voltage probes are arbitrarily placed around the edge of the slice instead of being restricted to the ends of the scanning diameter.

The newly developed hot/cold wafer probing apparatus was used to map the densities of the electrically active gold donor and the boron acceptor centers in silicon as a function of position across a processed wafer. The gold donor map was made by making thermally stimulated capacitance measurements on n^+p diodes. Preliminary experiments to study the feasibility of forming mesa diode structures by ultrasonic machining and plasma etching was completed. Although neither technique is, at the present time, fully satisfactory, neither can be ruled out for eventual use. To facilitate subsequent experiments of this kind, a photomask set of a test pattern which includes mesa diodes of various sizes, with and without guard rings, together with other related structures was designed.

An electrical method, based on the addition of donor centers, has been devised to verify the existence of the X-level which adversely affects the operation of indium-doped silicon in infrared detector arrays. This method was used to confirm that the X-level hypothesis is appropriate for describing a specimen which was thought to contain these levels on the basis of Hall coefficient data. Further experiments to test both the effectiveness of the method and the X-level hypothesis are underway.

Materials Characterization by Physical Analysis Methods — Study of limitations on the resolution of interface width in Auger-sputter profiling continued at Stanford University. The analysis of the effects of electron escape depth was extended to the geometry of the real cylindrical mirror analyzer system. Results of measurements on a group of silicon dioxide-silicon interfaces prepared by dry oxidation were analyzed with this technique. These results suggest that the transition region between the silicon and the oxide consists of an undulating connective region with a period less than 100 μm, a width no greater than 0.8 nm, and excursions of about 2 nm. The results further suggest that any of the suboxides of silicon (SiO_x) occur only within the 0.8-nm wide connective region. In related studies, it is suggested that experimentally observed differences in implanted profiles measured by ion microprobe mass anal-

ysis and Auger-sputter profiling could be explained by broadening due to ion-beam effects.

In the continuing study of x-ray photoelectron spectroscopy and other techniques for chemical diagnostics in semiconductor processing at the Jet Propulsion Laboratory, a precision wet etching procedure was devised and successfully employed for profiling silicon dioxide films thermally grown on single-crystal silicon substrates. Work also continued on the development of data reduction and presentation procedures for use with x-ray photoelectron spectroscopy.

Initial correlations were made at RCA Laboratories between electrical properties of devices fabricated on silicon films grown on sapphire substrates and the infrared and ultraviolet reflectance ratios of the substrate surfaces and silicon films, respectively. It was observed that the drain current measured on MOS transistors and the Hall mobility measured on gated Hall effect devices reached a saturation value at an intermediate value of infrared reflectance ratio characteristic of an intermediate level of polishing. No further improvement in these electrical characteristics was noted on more highly polished substrates. On the other hand no saturation trend was observed for these parameters as a function of ultraviolet reflectance ratios of the silicon films; improved device performance can therefore be expected from improved film crystallinity. These data suggest that substrate surface finishing is not the ultimate limiting factor in determining film quality and that it may be possible to reduce the cost of sapphire substrates by reducing the amount of polishing.

Materials and Procedures for Wafer Processing — Thermodynamic calculations for equilibrium concentrations of sodium and sodium compounds in oxidation furnaces were extended to the case of furnaces with silicon tubes. Although these tubes begin with much lower concentrations of sodium than do the previously analyzed fused silica tubes, they can become contaminated with sodium from external sources. As in the case of fused silica tubes, the presence of extremely small quantities of water vapor in the furnace atmosphere enhances the leaching of sodium from the oxidation tube and increases the sodium equilibrium density in the furnace.

Photolithography — Initial line-width calibration measurements were made on several black-chromium, photomask-like artifacts using the NBS scanning photometric microscope. The three-sigma standard deviation around the mean of nine line-width measurements (three measurements on each of three days) on a single line was typically between 0.03 and 0.09 μm. This relatively high variability is attributed to edge raggedness in the measured lines and focus displacements during scanning. In addition, procedures for making accurate line-width measurements using these calibrated artifacts have been developed. These procedures are intended primarily for use on an optical microscope equipped with a filar or image-shearing micrometer eyepiece. Comparison of line-width measurements made after an initial line-scale calibration showed that the systematic differences between measurements by the various eyepieces can be eliminated with the use of the line-width calibration.

Line-width measurements were made with the scanning photometric microscope on silicon and iron-oxide photomasks. Line-image profiles for these see-through masks were calculated for the case in which the numerical aperture of the condenser lens is sufficiently smaller than that of the objective lens. For this case, an expression can be derived for the transmittance threshold which corresponds to line-edge location. For see-through masks, the phase difference between light transmitted through the clear and background regions must be considered in calculating the transmittance threshold.

Conventional bright-field and dark-field microscope systems were evaluated for their suitability for making line-width measurements in reflected light. For a bright-field reflected-light system, there is no analytic expression to relate line-edge location to a transmittance threshold. Analytic expressions can be obtained for a dark-field reflected-light system by utilizing a newly developed computation technique. However, it was found that the calibration curve for actual line width as a function of measured line width is nonlinear and dependent on the numerical apertures of the condenser and objective lenses. Consequently, neither conventional system appears suitable for making accurate line-width measurements on silicon wafers.

Line-image profiles were calculated for lines less than 1 μm wide scanned with the photometric microscope. The calculations showed the system can measure line widths on a black-chromium photomask as small as 0.4 μm with an error of 0.05 μm. For masks with a higher background transmittance, the measurement ca-

pability extends only to 0.5 μm; for narrower lines, the line-image profiles change so rapidly that the transmittance threshold corresponding to edge location can no longer be utilized. Preliminary measurements were made on an exposed resist pattern on a silicon wafer. For the multiple 0.5-μm wide lines and spaces on this pattern, the results showed that the pattern features could be well resolved optically. Criteria for locating the test optics at the position of best focus were also established. For isolated lines, best focus occurs when the edge profile has its steepest slope; for multiple lines, the best focus appears to occur when the transmittance at the center of the line or space (whichever has the lower transmittance or reflectance) reaches the same relative background transmittance level as the larger semiopaque or clear areas of the test object.

The width of 1- and 3-μm wide clear and opaque lines was measured with a primary linewidth measurement system based on a scanning electron microscope (SEM) with an *in situ* polarization interferometer. A model was developed to describe the interactions of the electron beam with the material line. The line-edge trace calculated from the model agrees closely with the experimental SEM trace in the regions of the edge. The results of measurements on the opaque lines were almost identical with those obtained using the scanning photometric microscope. For the clear lines, however, differences were encountered which are greater than those expected from the measurement uncertainties associated with the two measurement systems. The cause of this anomaly is currently under investigation.

Test Patterns — A new test pattern was designed and fabricated for use in the reevaluation of the resistivity-dopant density relationship in silicon. The principal feature of this pattern was the inclusion of square-array four-probe resistor structures with various pipe sizes in order to permit measurements on wafers covering a wide range of resistivity. In addition, two new mask levels were added to the four used in earlier test patterns of this type. One of these is to facilitate contacting *n*-type base regions with aluminum metallizations for fabricating *p*-*n*-*p* structures. The second mask permits delineation of high-quality gate oxides for MOS devices.

Sheet resistance measurements were made with the six van der Pauw and two bridge base sheet resistors on the new test pattern. For measurements on low resistivity wafers, the results were as expected; all of the van der Pauw structures gave essentially the same sheet resistance, and the bridge structures gave lower sheet resistance because over-etch and lateral-diffusion effects caused the width of the latter structures to be greater than the design value which was used to calculate the sheet resistance. However, the presence of an inverted collector surface layer on a high resistivity *p*-type wafer caused the various van der Pauw structures to yield markedly different values for sheet resistance and the bridge structures to yield lower than expected values. This experiment reaffirmed the importance of controlling the surface layer characteristics in making electrical measurements on high resistivity *p*-type wafers.

A new test structure was designed to provide a rapid way to estimate the amount of overetching of a processed wafer from microscopical observations. The structure contains a built-in distance scale which allows one to calculate the amount of over-etching without knowing the magnification of the microscope used to observe the structure on the wafer.

Development work was completed on the software package for transforming test structure designs into working photomasks. Use of these computer programs is expected to facilitate development of a catalog of well characterized, modular test structures which can be combined easily into test pattern arrays for specific applications.

A specially designed test pattern containing arrays of various size contact pads was used to test the feasibility of probing the 2- by 10-pad array. It was found to be possible to probe 60-μm square pads with 100-percent reliability across a 2-in. (50-mm) diameter wafer; this pad size is smaller than the 80-μm square pads selected for the initial modular test patterns. It was also shown to be possible to combine the 2 by N modular layout of test structures with structures connected to contacts around the periphery of a die arranged in the same manner as those of the integrated circuit being fabricated. This combination is particularly useful when a test pattern die is inserted at selected points on a product wafer.

Design and layout were completed at the Westinghouse Advanced Technology Laboratories of an array of advanced test structures which include ancillary integral circuitry to permit measurement of very low currents at speeds

compatible with automatic dc testing equipment available to the industry. The test pattern is designed with a 2 by 10 modular cell arrangement; five different classes of advanced test structures have been included for evaluation. In addition, a variety of conventional test structures is included to permit comparison measurements as well as detailed study of the cross-bridge structure.

Experimental work on the development of a test pattern for characterizing and monitoring a large-scale-integration, silicon-on-sapphire process was completed at RCA Laboratories. Complete testing routines were established for all of the structures located in parts 1, 2, and 4 of the pattern which are intended to be tested on automatic electronic test equipment. An extensive report on this work is being prepared.

Assembly and Packaging — Detailed analysis was completed of the results of the interlaboratory evaluation of the radioisotope method for testing hermeticity of semiconductor devices being developed by ASTM Committee F-1 on Electronics. The estimated standard deviation ranged from 5×10^{-9} atm·cm^3/s for for a leak size of 1×10^{-8} atm·cm^3/s to 3.2×10^{-5} atm·cm^3/s for a leak size of 5×10^{-5} atm·cm^3/s. Significant individual laboratory biases were observed; if these could be eliminated by use of suitable calibration artifacts, it is estimated that the standard deviation could be reduced by a factor of about 2.

Device Inspection and Test — Studies of the application of the scanning acoustic microscope to the investigation of integrated circuits continued at Stanford University and Hughes Research Laboratories. The Stanford group has been able to observe individual stacking faults in silicon epitaxial layers with a clarity similar to that obtained in high quality interference contrast photomicrographs, as well as defects underneath metallization layers. Considerable understanding of the response of the scanning acoustic microscope to various layer structures typical of those found in integrated circuits is being obtained through mathematical analysis. The Hughes group is investigating techniques for preparing reflection gray-scale bar charts for use in measuring the acoustic contrast characteristics to complement earlier measurements of spatial resolution.

The experimental investigation of the suitability of using the temperature response of the substrate diode in an integrated circuit to evaluate the integrity of the die attachment was completed. Results of tests on integrated transistor arrays with voided regions intentionally introduced into the die attachment showed correlation between voided area and increase in temperature of the substrate diode junction. The sensitivity under pulsed conditions appeared adequate to detect void areas as small as 17 percent of the die area. These results suggest that at least in some cases the temperature response of the substrate diode can provide information regarding the quality of the integrated circuit die attachment.

An improved test method for determining the saturation voltage of bipolar transistors was developed and initial laboratory tests were conducted to validate the procedure. This test is intended for use in hardness assurance applications where it is desired to compare measurements of saturation voltage made before and after irradiation.

3. MATERIALS CHARACTERIZATION BY ELECTRICAL METHODS

3.1. Photovoltaic Method

The resistivity uniformity of the starting material plays a critical role in determining the characteristics and the performance of high power semiconductor devices. Variations in the resistivity of a slice of starting silicon not only cause variations in the characteristics of devices fabricated from that slice, but also contribute substantially to poor yield in the manufacturing process and adversely affect the reliability of finished devices. It is the purpose of this work to refine the photovoltaic scanning technique for measuring radial resistivity variations of circular semiconductor slices [1]. This technique is nondestructive in that no contact is required with the wafer surface area in which devices are to be fabricated; also it has better spatial resolution than the widely used four-probe method [2,3].

*Instrumental Development** — An automated data collection and analysis system has been designed and assembled (NBS Spec. Publ. 400-29, pp. 13-15) [4]. This system enables a user to measure the resistivity profile along a wafer diameter in about 2 min with some user-system interaction after the measurement has begun. Additional equipment modifications are being made to eliminate the user-system interaction after initiation of the measurement and to automate the measurement of the average resistivity of the slice by the van der Pauw method [5].

Because a number of problems, mostly mechanical, had been encountered with the original specimen holder with knife-edge contacts (NBS Spec. Publ. 400-29, pp. 13-15), a second holder with point-probe contacts, shown in figure 1, was fabricated and installed. With this holder, contacts are made to the top surface of the slice, about 0.25 mm from the periphery. It is expected that this location is close enough to the edge that no correction for probe position is required. Since the peripheral ring is usually removed during device fabrication, any damage which might be introduced by the probes would not affect the finished device.

(G. J. Rogers and D. L. Blackburn)

*System Characterization** — Study of the current-voltage characteristics of the point-probe contacts showed that the contact resistance was less than that of knife-edge contacts to the same slice, that the linearity of the point-probe contacts was better than that of the knife-edge contacts, and that the point-probe contacts were more repeatable from slice to slice.

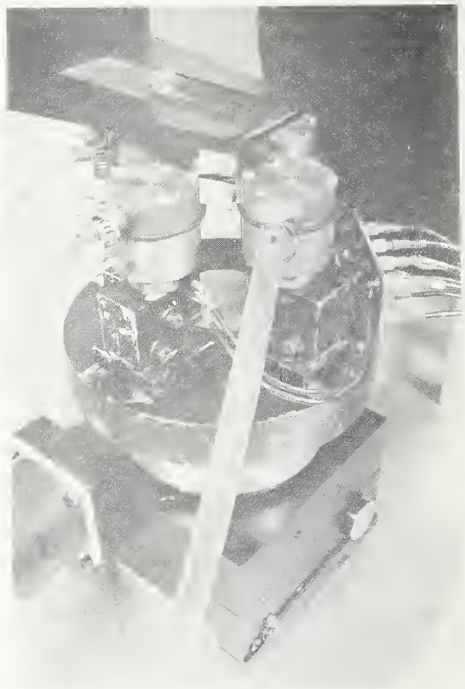

Figure 1. Photograph of probe holder with point contacts for photovoltaic scanning apparatus.

During initial measurements of resistivity profiles, several problems were encountered in both the photovoltage and photoconductivity measurements. A "lateral" photovoltage appeared between the two contacts at the same end of a measurement diameter; consequently, different photovoltages were measured by the two sets of contacts and the correct photovoltage could not be established. The measurements of photoconductivity, which require use of both sets of contacts, were found not to be reproducible. It was found that both problems were caused by large photovoltages generated by light scattered to the metal-silicon contacts. By carefully shielding the contacts from external stray light

* Principally funded by the Energy Research and Development Administration, Division of Electric Energy Systems.

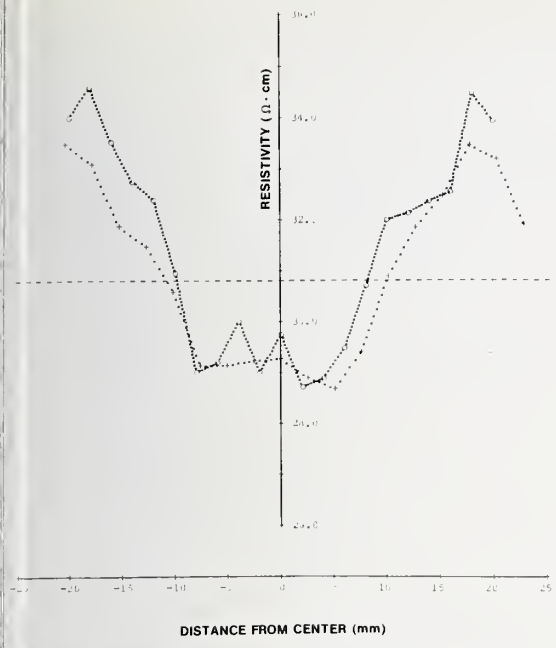

a. Mean resistivity: 30.8 Ω•cm.

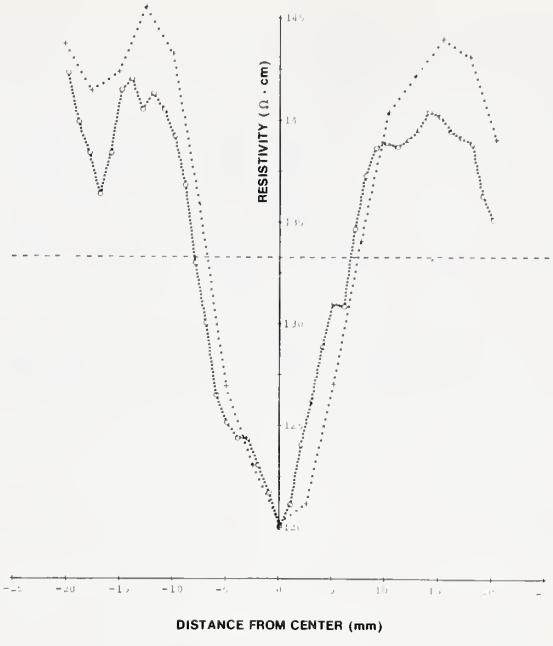

b. Mean resistivity: 133.3 Ω•cm.

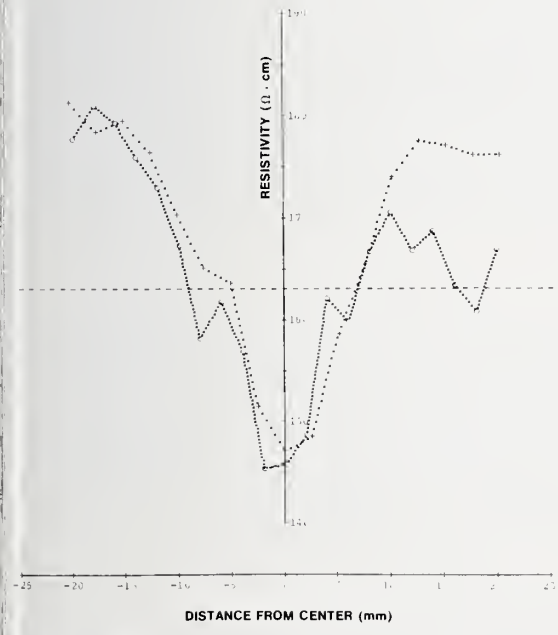

c. Mean resistivity: 163 Ω•cm

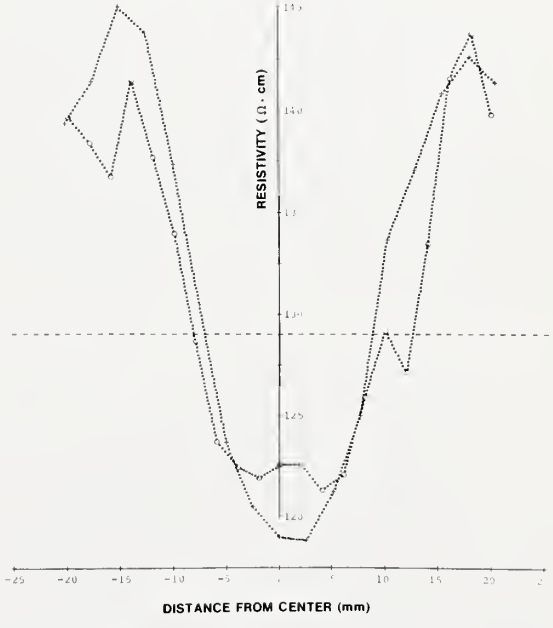

d. Mean resistivity: 129 Ω•cm.

igure 2. Examples of radial resistivity profiles measured on 2-in. diameter, n-type, float-oned silicon slices with photovoltaic and four-probe methods. (o: Photovoltaic method; x: our-probe method)

and using a strongly absorbed exciting laser beam (wavelength = 632.8 nm) in place of the previously used very penetrating one (wavelength = 1.15 μm) which might be scattered internally to the contact area, it was possible to effectively eliminate the lateral photovoltage in all but a few instances. In these cases, which are still under investigation, the photovoltage measured appears to be related to the surface condition of the wafer being measured.

With the elimination of the lateral photovoltage, it became possible to compare resistivity profiles measured with the photovoltaic and four-probe methods. Numerous such comparisons were made using the specimen holder with shielded point-probe contacts and the 632.8-nm laser source. Four examples are shown in figure 2. The results of the photovoltaic measurements were adjusted so that the average resistivity of the measured profile equals the resistivity of the slice as measured by the van der Pauw method. This procedure establishes the absolute resistivity at the initial point of the profile.

All of these measurements were made on specimens on which both surfaces had been lapped with 12-μm alumina grit. It has been found that the most repeatable results and profiles most like those determined by the four-probe method are obtained on this surface or on a lapped surface that has been lightly etched. These are the types of surface finish usually present for resistivity profiling of thyristor grade silicon because an abraded surface is usually desired prior to and during the initial diffusion process for these devices.

Preliminary measurements were made to evaluate the repeatability of the system. Eight measurements of the resistivity gradient were made over a period of four days on a single slice. The results are plotted in figure 3 together with two four-probe measurements of the profile. The spread in the photovoltaic data in this figure is less than 3 percent of the average resistivity. This is probably sufficient repeatability for a rapid, nondestructive method for measuring incoming float-zoned slices.

(D. L. Blackburn and G. J. Rogers)

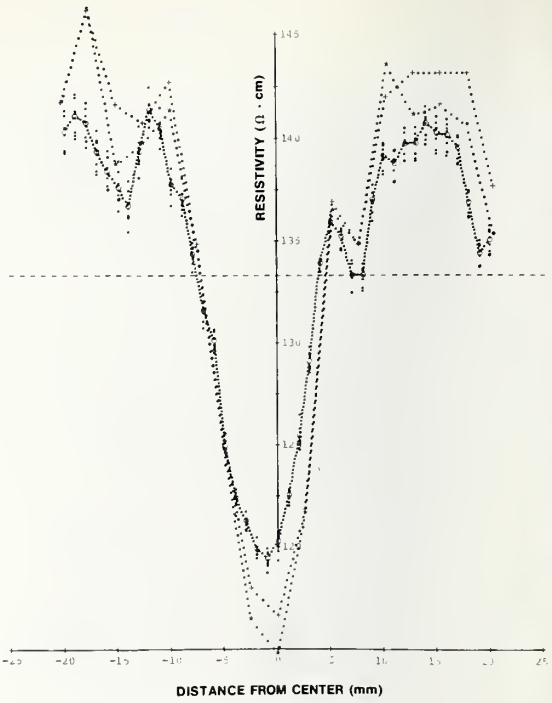

Figure 3. Results of repeatability study of photovoltaic method for measuring radial resistivity profiles. (Specimen: 2-in. diameter, *n*-type, float-zoned silicon slice with mean resistivity of 133.3 Ω•cm. o: Mean of eight photovoltaic measurements, plotted individually at the measurement points; +: four-probe measurement made at start of test; *: four-probe measurement made at end of test.)

Theoretical Analysis — The previous analysis of the photovoltaic and photoconductive signals [1] was reviewed with the intent of removing as many simplifying assumptions and restrictions as possible. Basically the same conformal mapping approach was used to satisfy the boundary conditions at the periphery of the circular slice and the edge of the circular light spot. However, it was found that by modifying the analytic form of the transformation equation, the amount of algebraic manipulation could be significantly reduced. In particular, the most useful function found for mapping the complex variable $z = x + iy$ into the transformed variable $w = u + iv$ was

$$w = \frac{1 - z/r}{1 + z/r}, \qquad (1)$$

where r is either the radius of the slice, b, or the radius of the light spot, a, depending upon which boundary condition is being met.

The algebraic simplification achieved through the use of this transformation made it feasible to generalize the analysis to consider cases where the current and voltage probes are arbitrarily placed around the edge of the slice instead of being restricted to the ends

of the scanning diameter and to include the effects of nonradial gradients in resistivity. The specimen geometry is depicted in figure 4 where the slice is aligned with its x-axis along the scanning diameter and probes are placed every 45 deg around the slice circumference. Probes 1 and 5, at the ends of the scanning diameter, are those used with the present measuring technique. Probes 3 and 7 along the y-axis could be used with the present technique to measure nonradial gradients in the y-direction. Probes 2, 4, 6, and 8 on diameters oriented at 45 deg with respect to the scanning diameter are the ones used in the 45-deg orientation geometry.

The resistivity gradient in an extrinsic silicon slice is given by

$$\frac{d\rho}{d\zeta} = -\frac{qC_1}{\pi kT} \cdot \frac{1+(\mu_{maj}/\mu_{min})}{f(x)} \cdot \frac{\overline{\rho}^2}{bt} \cdot \frac{V(x)}{\Delta R(x)}, \quad (2)$$

where ζ is x or y, q is the charge of the majority carrier, k is Boltzmann's constant, T is the absolute temperature, μ_{maj} and μ_{min} are the mobilities of the majority and minority carriers, respectively, $\overline{\rho}$ is the average resistivity of the slice, b is the radius of the slice, and t is the thickness of the slice. The constant C_1 and the quantities f(x), V(x), and $\Delta R(x)$, which depend on the position of the light spot x (which is assumed to have a radius a << b), are listed in table 1 for four cases of interest: the x- and y-gradients of resistivity measured with probes at the ends of the x- and y-axes (x-y geometry) or at the ends of the diameters oriented at 45 deg with respect to the x-axis (45-deg geometry). In the table the subscripts indicate the probes between which the voltage is measured or between which the current is applied, e.g., V_{51} is the potential difference between probes 5 and 1 and I_{51} is the current between probes 5 and 1.

The symmetry of these equations is significant, although it should be pointed out that V and ΔR have somewhat different definitions in the two geometries. Simple symmetry arguments show that nonradial (tangential) resistivity gradients do not influence the photo-

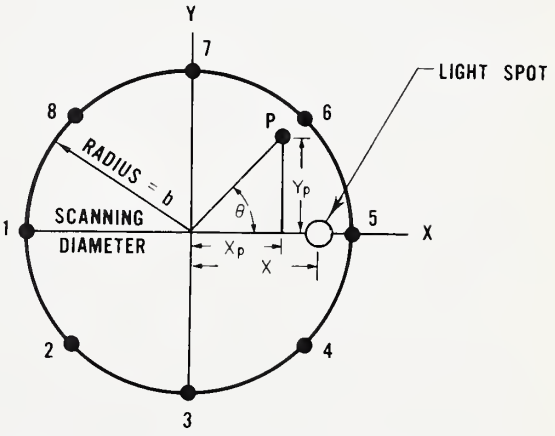

Figure 4. Schematic diagram of specimen geometry used for analysis of photovoltaic method for measuring radial resistivity variation.

Table 1 — Summary of Analysis of Spreading Resistance Method for Measuring Radial Resistivity Variation

Parameter in eq (2)	x-y Geometry		45-deg Geometry	
	x-gradient	y-gradient	x-gradient	y-gradient
C_1	1	1	$\frac{1}{2\sqrt{2}}$	$\frac{1}{2\sqrt{2}}$
f(x)	$1 - (x^2/b^2)$	$\frac{[1-(x^2/b^2)]^2}{[1+(x^2/b^2)]}$	$1 - (x^2/b^2)$	$1 + (x^2/b^2)$
V(x)	V_{51}	V_{73}	$V_{62} + V_{48}$	$V_{62} - V_{48}$
$\Delta R(x)$	$\Delta(V_{51}/I_{51})^a$	$\Delta(V_{51}/I_{51})^a$	$\Delta(V_{64}/I_{82})$	$\Delta(V_{64}/I_{82})$

[a] Two probes are required at each end of the diameter to avoid measuring the potential difference between current-carrying contacts.

voltage observed at the ends of the scanning diameter. These same symmetry arguments can be used to show that the contributions from the radial and nonradial components of resistivity gradient can be separated by taking the sum and difference of the photovoltages observed at the ends of the diameters at 45 deg to the scanning diameter. This allows one to measure each component of resistivity gradient separately and independently in the 45-deg geometry. Thus, in the x-y geometry, V is the photovoltage observed across the scanning diameter, or the diameter perpendicular to it, but in the 45-deg geometry it is the sum (or difference) of photovoltages observed across two diameters. The change in resistance induced by the light spot, ΔR, is observed in the x-y geometry by current and voltage measurements across the scanning diameter, but in the 45-deg geometry it is observed by current and voltage measurements using widely separated probes as in a van der Pauw measurement [5].

It should be noted that the equation for the x-gradient of the resistivity in the x-y geometry is 4/3 times the expression obtained in the original analysis [1,4]. This difference arises from two sources related to the treatment of the nature of the light spot in analyzing the photoconductive and photovoltaic aspects of the problem. In analyzing the photoconductive aspects, conformal mapping was used twice in succession, once to handle the circular boundary at the periphery of the slice, and then again to handle the circular boundary of the small light spot. The transformation function, eq (1), was used both times, with the appropriate value for r each time. An image of the light spot is generated in satisfying the zero normal-current boundary conditions at the edge of the slice in the first transform space. The effects of this image light spot must be included in the second transformation. This had been ignored in the previous analysis [1] because no way was found to evaluate its effects. This difficulty arose because the image light spot has a noncircular shape after being transformed back to the original coordinates for use in the second transformation. However, in the present analysis, it was observed that the symmetry of the transformed real and image light spots, coupled with their symmetrical position with respect to the transformed probe positions, leads to the conclusion that each will have the same net effect of the computed value of ΔR. Therefore, the neglect of the effect of the image light spot in the previous analysis led to an expression for ΔR that was too small by a factor of two.

In analyzing the photovoltaic aspects in the derivation, conformal mapping was used once again to satisfy the boundary conditions at the periphery of the slice. The transformation function, eq (1), was used with r equal to the radius of the slice. The boundary value problem at the edge of the light spot includes a photoinduced electric field within the light spot area (due to resistivity gradients interacting with the incident light) and the resulting current, both inside and outside the light spot area. In the previous analysis [1], an averaging over the light spot was employed, whereas in the present analysis an approximate solution to the actual boundary value problem was obtained using a uniform electric field inside the light spot and a dipole field outside the light spot. In this way, it was shown that the previous averaging technique underestimated the equivalent dipole moment of the light spot, and the resultant photovoltage, by a factor of two-thirds.

The 45-deg geometry is intuitively more attractive than the present x-y geometry because the light spot can be moved over the complete scanning diameter and not come close to a contact to produce extraneous effects due to photogenerated carriers reaching the metal-semiconductor contact. It does, however, require that three scans be made along the diameter mapped rather than the two needed for the x-y geometry. (R. D. Larrabee)

3.2. Thermally Stimulated Current and Capacitance Measurements†

Spatial Distribution of Gold in Silicon — Gold is frequently used to control the lifetime or switching characteristics of high-power diodes and thyristors. It is known to produce two centers in the band gap of silicon: an acceptor center 0.59 eV below the conduction band edge and a donor center 0.35 eV above the valence band edge [6]. The gold centers are generally produced by diffusing the gold near the end of the device wafer fabrication. The uniformity of the electrical activity of gold centers on wafer-sized power devices is an important consideration in the ability of the device to switch uniformly over its entire area.

†Principally funded by the Energy Research and Development Administration, Division of Electric Energy Systems.

The newly developed hot/cold wafer probing apparatus (NBS Spec. Publ. 400-29, pp. 20-22) [7] was used to map the gold donor concentration in a processed wafer. Thermally stimulated current and capacitance measurements were made on the 432-μm diameter n^+p gated base-collector diode (structure 3.10) of test pattern NBS-3 [8]. This test pattern is repeated at 5.08-mm intervals across the wafer; about 70 identical dice appear on a standard 2-in. diameter wafer. A typical bipolar process was used to fabricate the wafer on p-type silicon with a room temperature resistivity of 5 to 10 Ω•cm and (111) surfaces. After growth of the field oxide, the n^+ base regions were formed by diffusing phosphorus to form a junction about 1.5 to 2.0 μm deep. The test diodes considered here were not exposed to a subsequent emitter diffusion which was performed to complete other test structures. The gold center was introduced by the diffusion of gold, which had been evaporated on the back surface, for 24 h at 825°C.

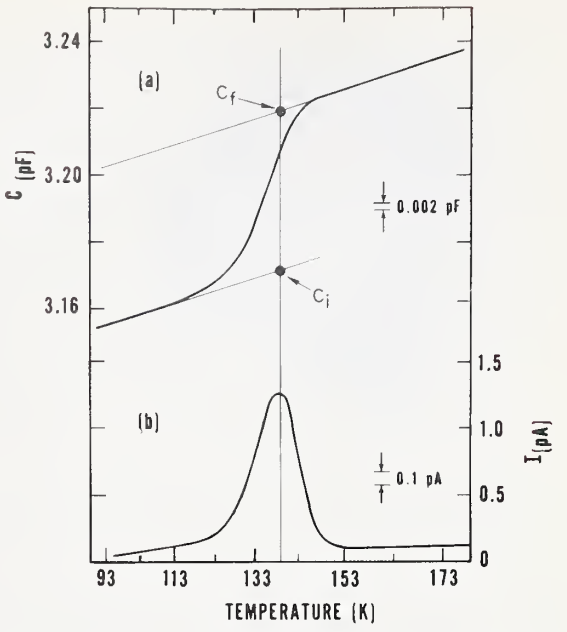

Figure 5. Typical thermally stimulated capacitance (a) and current (b) responses of a gold-doped n^+p diode. (Heating rate: 7 K/s.)

Figure 5 shows the thermally stimulated response from a typical diode on the processed wafer. The upper curve is the capacitance response and the lower is the current response. In each case, the response was measured by first cooling the device to near liquid nitrogen temperature. Zero bias was applied to the diode to charge all defects with majority carriers (holes); a reverse bias of 15 V was then applied to form a depletion region. The current or capacitance was measured with the depletion bias maintained while the device was heated at about 7 K/s. At the appropriate temperature, the gold donor emits its trapped hole resulting in both a measurable current and a slight collapse of the depletion region; the latter causes a measurable increase in capacitance. The system noise as reflected in the x-y recorder traces was approximately 2 fF and 0.1 pA for the capacitance and current, respectively.

The gold donor density, N_t, was determined from the measured thermally stimulated capacitance response [9]:

$$N_t = N_A \frac{2(C_f - C_i)}{C_f} , \qquad (3)$$

where N_A is the background boron acceptor density and C_f and C_i are the capacitances indicated in figure 5. This expression is appropriate for the present case since only hole emission from the gold donor center need be considered and since the initial capacitance, C_i, is much less than the capacitance of the diode at zero bias. This determination is independent of heating rate since it is the total change in charge on the center that is important. However, it is necessary to obtain an independent measure of N_A. The average acceptor density in the depletion region was calculated from:

$$N_A = \frac{2C_1^2C_2^2(V_2-V_1)}{qK_{Si}\varepsilon_o(C_1^2-C_2^2)} , \qquad (4)$$

where C_1 and C_2 are the capacitances of the diode at two values of reverse bias, V_1 and V_2, respectively; q is the electronic charge; K_{Si} is the relative dielectric constant of silicon; and ε_o is the permittivity of free space. Wafer maps of N_t and N_A as a function of position on the wafer are displayed in figure 6. In each case the darker areas represent regions of greater density. As indicated on the maps, the gold donor density varies from 2.34 to 3.61 × 10^{13} cm^{-3}, and the acceptor density ranges from 1 to 1.5 × 10^{15} cm^{-3}. It appears that there is no relationship between the donor defect density and the acceptor background. The system noise (2 fF) suggests that donor densities as low as

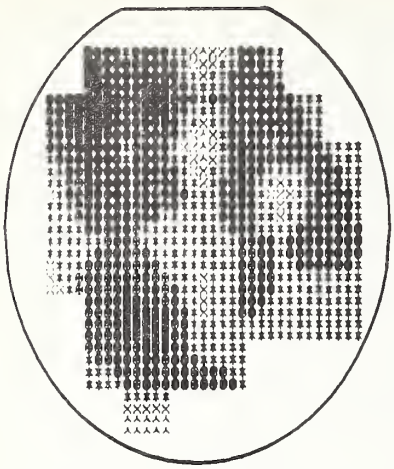

a. Gold donor density. Range: 2.34 to 3.61 × 10^{13} cm^{-3}.

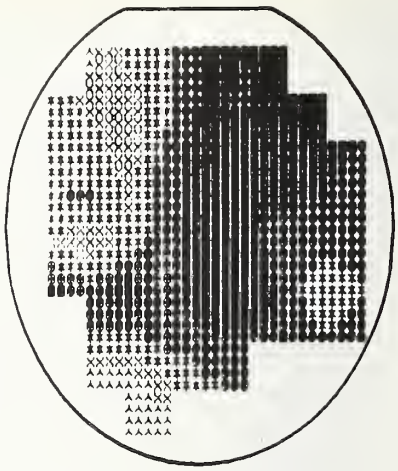

b. Boron density. Range: 0.99 to 1.15 × 10^{15} cm^{-3}.

Figure 6. Wafer maps of gold donor and boron acceptor densities in a 2-in. diameter silicon wafer. (Higher density occurs in darker regions on the map; every fourth point is an actual data point; others are interpolated.)

1 × 10^{12} cm^{-3} could be detected in this wafer. (R. Y. Koyama, W. E. Phillips, and Y. M. Liu)

Mesa Diode Fabrication — As discussed previously (NBS Spec. Publ. 400-36, pp. 23-24), special test structures are required to define and isolate the *p-n* junction in a partially or fully fabricated thyristor. This is most conveniently done by defining a pattern of mesa diodes over the front surface of the thyristor wafer. Three techniques are being considered for forming the mesa diode structures: ultrasonic machining, plasma etching, and chemical etching.

Initial test devices were produced by ultrasonic machining as illustrated in figure 7. In this process the diffused silicon is impact ground by an ultrasonically driven stainless steel tool and an abrasive slurry (fig. 7c). During the cutting operation, the front surface of the wafer is covered by a thin glass plate (fig. 7b) to prevent chipping. A special tool head was fabricated to form 22 mesa regions each about 1.5 mm in diameter and spaced on a square grid with 5.08 mm between centers. About 10 min is required to cut through the cover plate and approximately 75 μm into the silicon surface. The moat surrounding each mesa is briefly chemically etched in CP-6[§] to remove the damaged surface layer created by the grinding operation. The remaining sections of the glass microscope slide serve as a mask to protect the mesa surfaces during etching. The back surface diffused layer is lapped off (fig. 7d), and, after removal of the protecting glass plates, a 200-nm thick layer of undoped silicon dioxide is then deposited on the front surface of the wafer by conventional chemical vapor deposition techniques (fig. 7e) to passivate the junction edges which were exposed during the formation of the mesas. The CONTACT mask of test pattern NBS-2 [10] is used to define the contact areas (structure 2.09) by conventional photolithographic techniques. A 600-nm thick aluminum film is deposited on the front surface of the wafer, and ring contacts are defined with the METAL mask of test pattern NBS-2 (fig. 7f). A metal contact is also deposited on the back surface of the wafer. A photomicrograph of the front surface of a completed mesa diode is shown in figure 8.

About 20 percent of the diodes fabricated on several wafers had leakage currents of about 10 nA at a reverse bias of 10 V at room temperature; diodes with this magnitude of leakage current are suitable for making thermally stimulated current and capacitance measure-

[§] CP-6 (HNO_3:HF:CH_3COOH, 5:3:4) is available commercially under the name "silicon etch" from such suppliers as Corco Chemical Corp., Fairless Hills, PA 19030 and Transom Co., Rte. 1, Rowley, MA 01969.

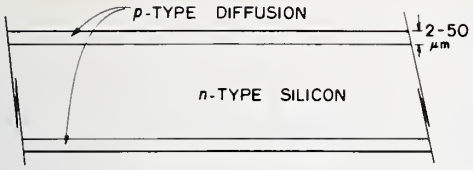

a. Diffused wafer.

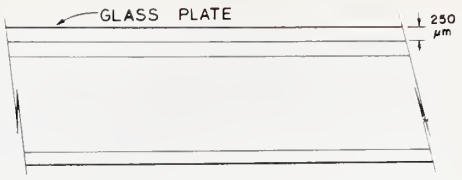

b. Wafer protected by thin glass plate.

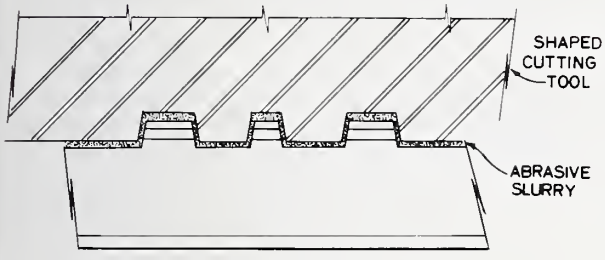

c. Ultrasonic cutting.

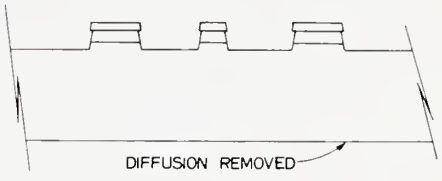

d. After removal of back-surface diffusion.

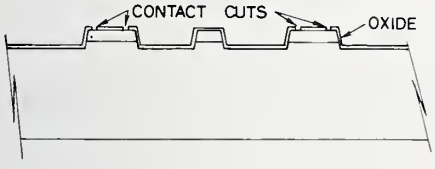

e. After deposition of oxide and definition of contact rings.

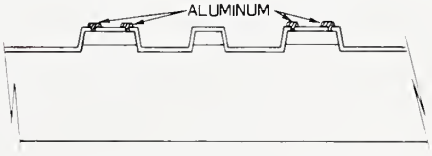

f. After deposition of aluminum.

Figure 7. Mesa diode fabrication process.

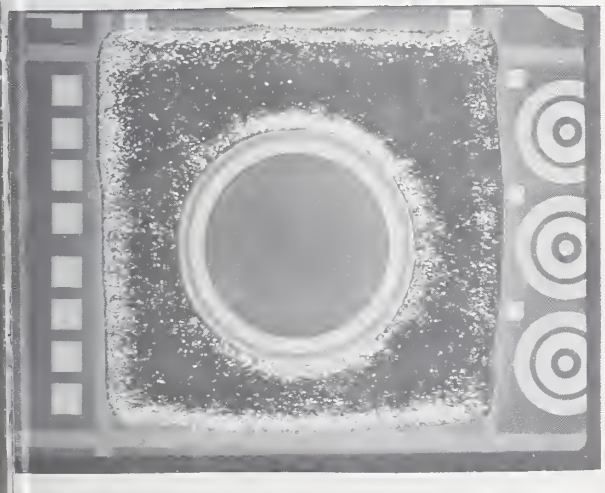

Figure 8. Photomicrograph of typical ultrasonically formed mesa diode. (The outside diameter of the mesa is about 1.5 mm.)

Figure 9. Photomicrograph of typical plasma-etched mesa diode. (The outside diameter of the mesa is about 230 μm.)

ments. Most of the devices, however, had leakage currents which were much larger; surface leakage is the probable source. The procedure for the ultrasonic fabrication of mesa diodes needs to be refined in order to achieve greater reproducibility of device quality.

Mesa structures were also produced by plasma etching, with the use of a simple three-level dot-matrix mask set. Plasma etching [11] is a "dry" chemical process which is used for removal of various materials in the semiconductor industry. In the present application, it is used to remove regions of silicon from the surface of the wafer not protected by the mesa mask. An rf plasma is used to excite an atmosphere of carbon tetrachloride and oxygen to produce various chemically reactive atoms, ions, electrons, and free radicals. These species chemically react with the surface to etch the silicon.

Whereas the ultrasonically formed mesa is defined by the mechanical dimension of the tool, the plasma etch technique requires a mask to protect the mesa region while the moat is being etched. In a first attempt at using this technique, an oxide film 300 nm thick was thermally grown on a diffused wafer. The oxide was patterned by a photolithographic operation to protect the mesa areas of the diode structure. After plasma etching the moat, an oxide film about 50 nm thick was thermally grown for the passivation. Finally, contact cuts were made and the contact metal was applied and patterned. A photomicrograph of typical mesas, 230 μm in diameter, is shown in figure 9. This procedure was successful in fabricating diodes of good leakage characteristics. Of the more than 20 devices tested most had a leakage current in the range of a few nanoamperes at room temperature with a 10-V reverse bias.

Although the plasma etched mesa is a definite possibility with respect to mesa diode fabrication, it has, in its current form, some disadvantages with respect to characterization of in-process power device material. One disadvantage is the relatively time-consuming step of the mesa etching; with present equipment the etching rate is only a few tenths of a micrometer per minute. Further, thermal oxidation steps were employed in this initial test for both masking and passivation. These steps require a temperature of 1000°C for about 20 min. Although this is both cooler and shorter than the deep diffusion temperature and time, it has not yet been established that thermal oxidation does not alter the characteristics of the wafer.

To avoid some of the complications encountered in these preliminary studies of mesa diode fabrication, a special test pattern, designated as test pattern NBS-13, was designed. This test pattern includes mesa diodes of various sizes, with and without guard rings, contact resistors, and mesa etch rate monitors. The simplest procedure for fabricating the mesa diode requires a three-level mask set.

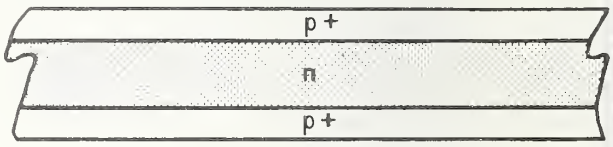

a. Diffused wafer.

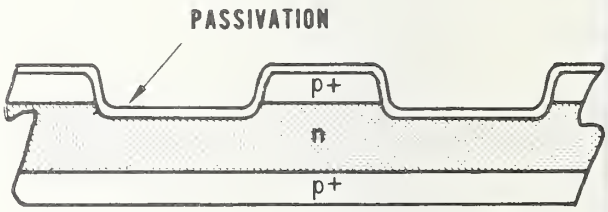

b. After mesa definition (Mask 1) and passivation.

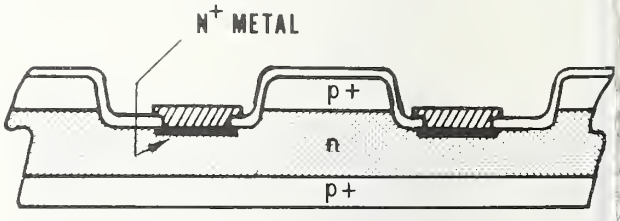

c. After n-contact cut (Mask 2), n-metallization, and n-metal definition (Mask 3).

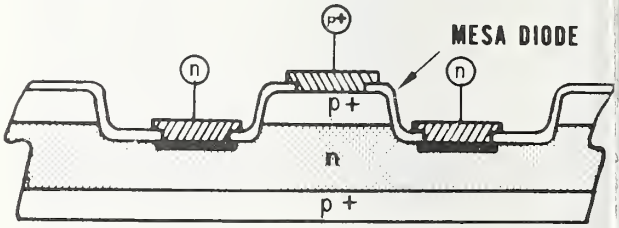

d. After p-contact cut (Mask 4), p-metallization, p-metal definition (Mask 5), and microalloy.

Figure 10. Postulated mesa-diode fabrication process using five-level photomask set.

After cleanup of the diffused starting wafer, the first step is to define the diode mesa area with the first level mask. After the moat area surrounding the mesa is removed, a passivation layer is applied to protect the junction. Following this, two mask levels are required for cutting the contact areas and defining the contact metallizations. Although there should be no problem associated with the metallization to the p^+-region, it is likely that metallization to the high resistivity n-region could result in a rectifying Schottky barrier contact. Because the fabrication procedures and test structures are in a development phase, it was appropriate to incorporate flexibility into the mask set. Hence, the mask set was designed with separate levels for the contacts to the n- and p-type regions.

A possible use of this mask set is illustrated in figure 10. As in the three-level case, described above, the first mask defines the mesa areas. This is followed by passivation. The second and third masks are used to cut and define the gold-0.6% antimony contacts to the n-type regions. The fourth and fifth levels are used to cut and define the aluminum metallization to the p-type region. A microalloy step (400°C) is included to insure good adhesion and low resistance, nonrectifying contacts. (J. Krawczyk, R. Y. Koyama, T. F. Leedy, and Y. M. Liu)

3.3. Indium-Doped Silicon

This work was undertaken to identify parameters associated with extrinsic infrared detection in silicon that present problems of measurement and to develop appropriate measurement technologies to solve these problems (NBS Spec. Publ. 400-36, pp. 17-20). Initial efforts are directed toward methods for characterizing indium-doped silicon.

Some observers [12-14] have reported an extraneous acceptor level in this material, but it has not been seen by others. If present, this additional level can seriously degrade detector performance and, if not adequately controlled, could give rise to appreciable variations in photoresponse over the active area of an imaging array. Therefore, it becomes important to determine if this is a real level or just an artifact of the measurement techniques used. If it proves to be a real level, it then becomes necessary to determine if it is present to the same extent in material from a variety of sources. This problem is being approached by collecting material from various sources, confirming their characterization measurements, and performing new experiments aimed directly at checking the validity of any extraneous level interpretation of the behavior observed. For example, the temperature dependence of the Hall coefficient is the traditional parameter measured to determine dopant energies and densities. Unfortunately, the interpretation of Hall measurements in terms of dopant parameters is not necessarily unique; the same data can frequently be fitted, within the experimental error, by assuming different sets of energies and concentrations of impurities. Therefore, some method must be devised to distinguish between the various possible interpretations. One way of accomplishing this is by measuring the effects of introducing additional donors to the test specimen. Since the different interpretations generally predict quite different behavior with donor addition, a second Hall measurement after donor addition can usually identify incorrect interpretations. Donors can be added by several techniques: by neutron transmutation of the silicon to form phosphorus by the reaction [12]

$$^{30}\mathrm{Si} + \mathrm{n} \rightarrow {}^{31}\mathrm{P} + \beta^- \ ;$$

Table 2 — Donor Formation in Silicon With Various Oxygen Contamination Levels on Heat Treatment at 450°C

9-μm Absorption Coefficient, cm^{-1}	Donor Density After 10 Min, cm^{-3}	Maximum Donor Density, cm^{-3}[a]
4.67	1.2×10^{15}	7×10^{16}
4.15	6.8×10^{14}	6×10^{16}
3.63	3.8×10^{14}	3.5×10^{16}
3.11	2.1×10^{14}	2.4×10^{16}
2.6	9.5×10^{13}	1.5×10^{16}
2.08	3.8×10^{13}	6.5×10^{15}
1.04	2.6×10^{11}	8×10^{14}
0.52	1.4×10^{11}	7×10^{13}
0.10	1.5×10^{8}	7×10^{11}
0.052	8.0×10^{6}	7×10^{10}

[a] This is the donor density formed after heating at 450°C for very long times.

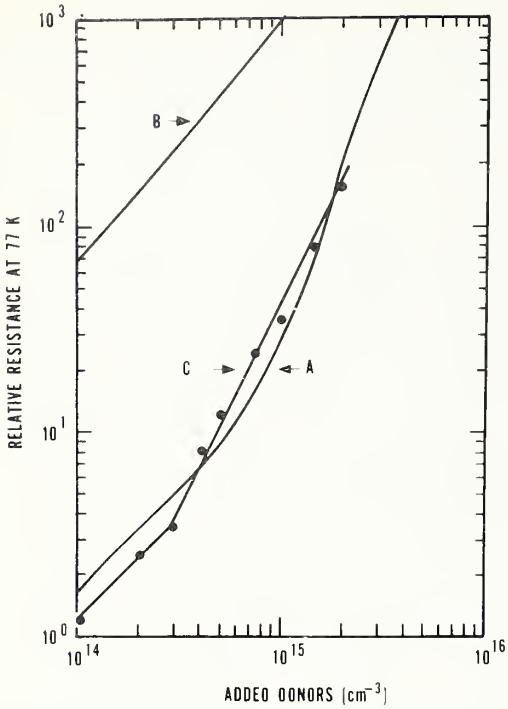

Figure 11. Resistance of an indium-doped silicon specimen at 77 K as a function of added donor concentration. (A: computed curve based on a model which includes the extraneous level; B: computed curve based on a model which does not include the extraneous level; C: experimental curve.)

by indiffusion, at 300° to 500°C, of lithium, which is an interstitial donor [15]; or, if sufficient oxygen is present in the crystal, by forming oxygen donor complexes by annealing in an inert atmosphere at 450°C for a short time [16,17].

A preliminary experiment was carried out on a silicon specimen known to exhibit the extraneous level behavior, from a crystal with an absorption of 4 cm^{-1} in the 9-μm oxygen band [18]. Varying amounts of donors were introduced by heating the specimen at 450°C for a series of short periods of time. Based on data of Baker [19], reproduced in table 2, and with the assumption that the rate of donor formation is constant for the total period of exposure to 450°C. In this experiment, the rate of donor introduction was taken as 5×10^{13} $cm^{-3} \cdot min^{-1}$.

The effects of adding oxygen donors to this specimen (determined in this case by measurement of the resistivity rather than the Hall coefficient) closely followed the behavior predicted by a model which included the extraneous level, as shown in figure 11. The behavior was quite different from that predicted by an alternative model which satisfactorily described the same Hall data but did not include extraneous levels. These data argue strongly for the validity of the extraneous level hypothesis.

Additional test specimens with various amounts of oxygen and extraneous levels are being obtained in order to conduct additional, more definitive experiments in which the Hall coefficient, as well as the resistivity, is to be monitored as donors are added. In addition, facilities have been set up to measure the spectral photoresponse attributable to the extraneous level as a function of added donor density, as a further test of the extraneous level hypothesis.

(R. D. Larrabee)

4. MATERIALS CHARACTERIZATION BY PHYSICAL ANALYSIS METHODS

4.1. Electron Spectroscopy Techniques

Limitations on Interface Width Resolution in Auger-Sputter Profiling: Electron Escape Depth — If the detected Auger electrons are emitted normal to the specimen surface, the emission strength, A(x), of a transition can be written as*

$$A(x) = \frac{1}{L}\int_0^\infty f(x+x')\, e^{-x'/L}\, dx' \,, \qquad (5)$$

where x is the depth of material sputtered away or, equivalently, the position of the surface after some amount of sputtering; L is the mean free path of an electron of energy E in the solid; and f(x) is the concentration profile to be determined from measurements of A(x) as a function of the sputtered depth. The variable x′ is the distance along the normal with an origin at the sputtered depth.

It is assumed that the upper layer of the specimen is uniformly excited by the incident electrons and that the specimen surface is smooth. The derivative of the emission strength formula,

$$\frac{dA(x)}{dx} = \frac{1}{L}\int_0^\infty \frac{df(x+x')}{dx}\, e^{-x'/L}\, dx' \,,$$

can be integrated by parts (noting that $df(x+x')/dx = df(x+x')/dx'$) to obtain:

$$\frac{dA(x)}{dx} = -\frac{1}{L} f(x) + \frac{1}{L} A(x) \,,$$

which may be rewritten:

$$f(x) = A(x) - L\frac{dA(x)}{dx} \,, \qquad (6)$$

to provide a formula with which the measured profile can be deconvolved.

The cylindrical mirror analyzer (CMA) system used in the present work has a ring aperture with an axis 30 deg from the normal to the specimen surface. Hence, the electrons which are detected are not emitted normal to the surface but rather over a broad range of angles. Electrons emitted at an angle θ from the normal travel a distance x′/cos θ inside the specimen. Electrons which pass through various parts of the ring aperture are emitted at different angles. If the width of the aperture is assumed to be very small and if the azimuthal angle on the ring is denoted by φ, the geometry of the present apparatus is such that

$$\cos\theta = 0.6405 + 0.3365\cos\phi \,.$$

The emission strength can then be written

$$A(x) = \int_0^\pi \int_0^\infty f(x+x')\, e^{-x'/L\cos\theta}\, dx' d\phi \,. \qquad (7)$$

If the integral over φ is approximated by a summation,† f(x) may be obtained from A(x) by a numerical routine. To check the effect of the broadening on a step interface under these conditions, the numerical routine was run in reverse to obtain the signal which would be obtained from a step interface, as well as reproduce the step. The results are illustrated in figure 12. The measured width, over which the signal decreases from 90 to 10 percent of its maximum value, is 1.64 L. For the on-axis system, the measured width of a step interface was found to be 2.2 L (NBS Spec. Publ. 400-36, p. 32). The curve in figure 12 can be approximated by an exponential with a decay constant approximately 0.75 (1.64/2.2) times the decay constant for the case of the on-axis detection system; this result suggests that the following deconvolution formula is a useful approximation for the CMA system:

$$f(x) = A(x) - \frac{3}{4} L \frac{dA(x)}{dx} \,. \qquad (8)$$

The difference between results obtained from the approximation of eq (8) and from the complete calculation is illustrated in figure 13 for an MNOS structure which was comprised of

---

*This formulation is equivalent to that derived previously (NBS Spec. Publ. 400-36, pp. 31-32), but the origin of the x-axis has been shifted from the interface to the surface of the specimen.

†When this is done, it is convenient and straightforward to eliminate contributions from those portions of the aperture which are blocked by obstructions in the apparatus.

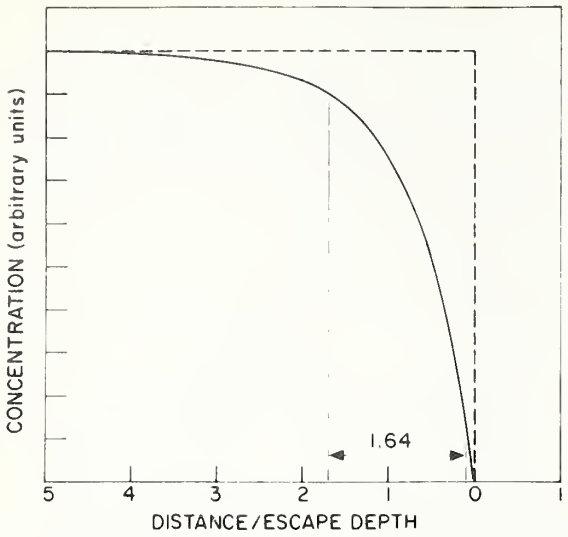

Figure 12. Computed signal obtained from a step interface with an Auger electron spectrometer with a cylindrical mirror analyzer.

a thin silicon dioxide layer sandwiched between pure silicon and silicon nitride. In the figure, the solid curve represents the measured signal, and the dashed curve represents the corrected concentration as calculated by the numerical routine with the assumption of a 1.2-nm escape depth. Note that the peak height is increased by 30 percent. Points calculated from eq (8) are plotted as solid circles on the figure. The curve through these points is shifted somewhat more to the right and reduced slightly in height, but does appear to be a good approximation.

(C. R. Helms[§], S. Schwarz[§], and W. E. Spicer[§])

Auger-Sputter Profiling of MOS Oxides — Auger-sputter profile measurements were made on a group of oxide-silicon interfaces prepared by oxidation of (100) silicon wafers in a dry oxygen atmosphere at 1000°C. The oxidations were carried out as follows: Chemically cleaned wafers were inserted into an oxidation furnace in flowing nitrogen, with an insertion time of 2 min. The wafers remained in the nitrogen ambient for an additional 8 min before dry oxygen was let into the furnace. This time interval insured that the wafers were at the oxidation temperature before oxidation began. After oxidation, the wafers were annealed for 8 min in nitrogen before being withdrawn from the furnace; withdrawal time was 2 min. The thickness of the oxide films, as determined by ellipsometry,

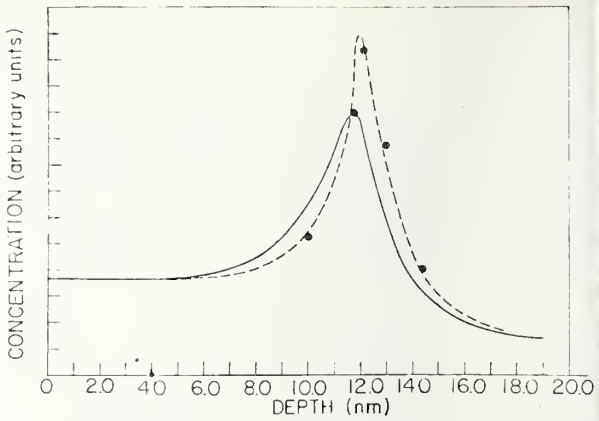

Figure 13. Oxygen concentration profile in MNOS structure. (Solid curve: measured Auger signal; dashed curve: signal corrected with numerical routine; solid circles: signal corrected with eq (8).)

C-V measurements, or step-height measurements ranged from 24 to 96 nm.

Sputtering was carried out with neon, xenon, or argon at 1 keV or argon at 500 eV and both the oxygen KLL transition at 510 eV and the silicon LVV transition at 92 eV were monitored as a function of sputter depth; typical profiles are depicted in figure 14 which shows the results on a 96-nm thick oxide. No significant differences in the measured width (10% to 90%) of either the oxygen or silicon line were observed for films of different thickness or for the different sputtering conditions. The measured oxygen and silicon widths were 3.35 ± 0.25 nm and 2.5 ± 0.15 nm, respectively, where the variability indicated is one sample standard deviation. The major contribution to the difference in values obtained is the escape depth. When the escape depth is deconvolved from the profiles, values of 2.5 ± 0.5 nm and 2.25 ± 0.25 nm are obtained. If in addition a correction is made for the ion range (NBS Spec. Publ. 400-25, pp. 16,17) [20], it can be concluded that the transition region between pure silicon and pure silicon dioxide is about 2.0 nm [21].

The significance of these measurements is twofold. First, any nonuniformities in the sputtering process should give a broadening ef-

[§]Work performed at Stanford Electronics Laboratories of Stanford University under NBS Contract No. 5-35944. NBS contact for additional information: K. F. Galloway.

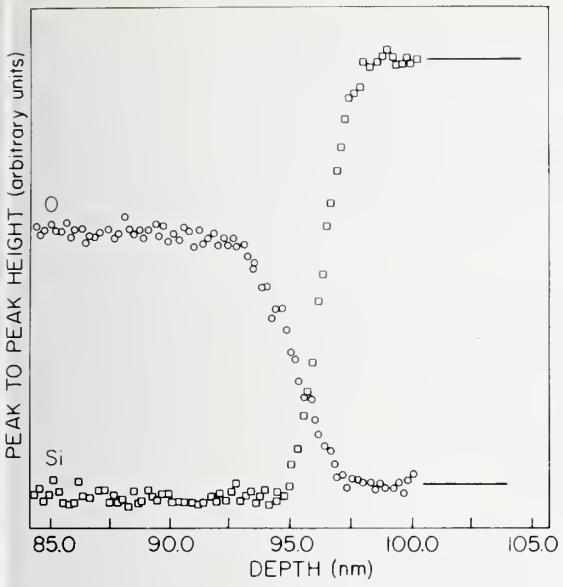

Figure 14. Oxygen KLL and silicon LVV signals as a function of distance near the interface between silicon dioxide and silicon.

fect that is proportional to thickness; from these data, these effects are clearly undetectable. Second, all of the interfaces studied had identical electrical characteristics; it is therefore encouraging that the measured interface properties were also identical.

Neither in this study nor in previous work (NBS Spec. Publ. 400-25, pp. 18-19) [21] has evidence been observed for a different chemical state of silicon, which might be expected to occur in the transition region. This result, however, may be due to the ion knock-ons which have a tendency to "scramble" the chemistry of the region of interest. There is considerable uncertainty in the effect of the ion beam on SiO_x type materials; their presence may only be detectable in the Auger data taken during sputtering before the interface is reached. For 1-keV argon ions, the depth for significant damage is estimated to be about 3.0 nm. With an escape depth of 3.0 nm (Si KLL transition), and assuming a minimum sensitivity of 10 percent, it is estimated that a layer of SiO_x, 0.8 nm thick or thinner, could not be detected.

These results lead to the model shown in figure 15 for the interface [22]. The width of the transiton region is probably due to an undulating interface, the period of which is certainly less than 100 μm, the distance over which the electron beam is rastered, and any

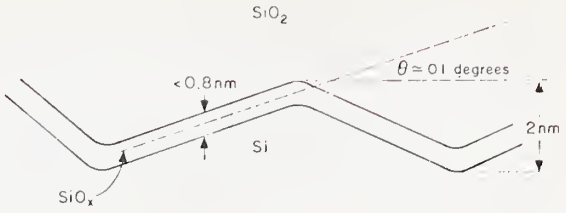

Figure 15. Model for silicon-silicon dioxide interface.

SiO_x present is in a connective region no greater than 0.8 nm wide. The value for the width of the transition region is consistent with the results of recently reported ion thinning, transmission electron microscopy experiments [23] in which an undulating interface with about 2-nm excursions and a periodicity of about 1 μm was found. The value for the upper limit of the width of the connective region is consistent with the results of recent internal photoemission studies [24] in which no evidence was found for an SiO_x region or significant excess charge extending further than 0.4 μm from the interface. On the other hand, the results of experiments [25] using x-ray photoelectron spectroscopy suggest that the thickness of the connective region is somewhat greater than 0.8 nm. The experiments were, however, performed on very thin oxides, and it is not unreasonable to expect the interface region of a thin oxide, present during the initial stages of oxidation, to differ from that obtained after 25 to 100 nm of oxide had been grown.

(C. R. Helms[§], S. Schwarz[§], W. E. Spicer[§], and N. Johnson[¶])

A Comparison of Ion Microprobe and Auger-Sputter Profiling — Auger-sputter profiling (ASP) measurements were made on a group of silicon specimens implanted with phosphorus or antimony that had also been profiled by ion microprobe mass analysis (IMMA). In general, the peak concentrations measured by ASP were about 30 percent higher than those measured by IMMA on the same profile. This difference appears to be due to ion-beam effects which are present in both experiments but to a lesser extent in the ASP work.

[§]Work performed at Stanford Electronics Laboratories of Stanford University under NBS Contract No. 5-35944. NBS contact for additional information: K. F. Galloway.

[¶]Xerox Palo Alto Research Center, Palo Alto, California 94304.

The broadening due to the 1-keV ions used in ASP has been found to be about 1.5 nm. For the 20-keV ions used in IMMA the broadening is estimated to be about 15 nm, a value which is about the same order of magnitude as the width of the implanted profile. Hence, significant broadening of the measured profile is possible with an accompanying reduction in the peak height as compared with the effects due to the lower energy ion beam used in ASP. (C. R. Helms[§], S. Schwarz[§], and W. E. Spicer[§])

4.2. Techniques for Chemical Diagnostics in Semiconductor Processing

The objective of this task is the development of a standardized measurement technology for chemical diagnostics for implementation in the semiconductor industry. This measurement technology is based on the use of x-ray photoelectron spectroscopy (XPS or ESCA) as the primary chemical probe. XPS and other complementary surface analytical spectroscopies are used to follow the surface chemistry of material at critical stages of semiconductor device processing. This effort is currently emphasizing two of the most important aspects of that technology: depth profiling and data reduction.

Depth Profiling — Since surface analytical techniques can sample only the volume within about 10 nm of the surface, it is necessary to combine material removal with these methods in order to measure concentration profiles as a function of depth down through material. There are two basic approaches to this problem: 1) ion milling (sputter etching) and 2) wet chemical etching. Currently, ion milling is in great favor since it can be combined with simultaneous Auger spectroscopy for elemental depth profiles. However, considerable chemical and physical damage to the specimen is introduced by the ion beam. This damage is related to ion energy. Although damage is minimized at energies below 500 eV, considerable chemical damage has been observed when even 100-eV argon ions are used to mill silicon or silicon dioxide.

Wet chemical methods based on immersion in dilute solutions of hydrofluoric acid in water or various nonaqueous solvents have not been fully successful. The porosity of silicon dioxide and the reactive solubility of the water in the oxide leads one to expect chemical modification of the structure after long term immersion in such solutions. In the course of the previously described study of carbon at the silicon-silicon dioxide interface (NBS Spec. Publ. 400-36, pp. 34-35), it was observed that square specimens, about 1 cm on a side, when spun at 12,000 rpm could be uniformly etched by drop-wise addition of hydrofluoric acid solutions to the spinning surface. Preliminary experiments were initiated to investigate the reproducibility of this system.

Pipetting devices which dispense 5 μL with an accuracy of ±0.1 percent or better were used to dispense the etching solution in 50-μL drops. Several oxide films, 10 or 30 nm thick, were grown on silicon specimens and etched back by this technique. The thickness of the remaining oxide was measured ellipsometrically, and no thickness variations were observed over the surface. No topographical detail was observed on several specimens which were examined by electron microscopy after the oxide thickness had been reduced to about 3 or 4 nm. These experiments suggested that a depth profile can be taken in which the depth coordinate is measured in terms of chemical equivalents of solvation. Therefore, additional work was undertaken to refine the etching apparatus and to optimize the etching chemistry.

The current technique for controlled wet chemical etching is designed to apply well-defined amounts of chemical etchant to the specimen surface for a controlled period of time. The choice of a solution-phase etchant permits control of the process on an atomic scale. Subtly different chemical bonds show different reactivities to the same etchant. The various forms of silicon dioxide show a wide variation in etching rate when exposed to hydrofluoric acid. Precise control of the amount of etchant and the time of exposure should therefore enable the experimenter to discern small variations in the silicon-oxygen chemistry.

As noted above, however, immersion of the specimen in a solution, would expose the inner layers of the oxide to the solvent through rapid diffusion. The presence of solvent molecules within the lattice could lead to reaction with the oxide lattice, redistribution of impurities, and modification of defects. This technique is therefore based on the exposure of the specimen surface

---

[§] Work performed at Stanford Electronics Laboratories of Stanford University under NBS Contract No. 5-35944. NBS contact for additional information: K. F. Galloway.

to a liquid film of controlled composition for time periods of 1 to 1000 ns. This solid-liquid analog of a stopped-flow system is accomplished by placing the specimen on a platform spinning at a constant velocity between 10,000 and 100,000 rpm and dispensing etchant onto the specimen surface as 50-μL drops. Each drop is permitted to evaporate to dryness before the next drop is dispensed. The experiment is performed within the environmental chamber attached to the XPS spectrometer introduction lock. This chamber is dynamically flushed with dry nitrogen gas and the residual water concentration is limited to less than one part per million. All solutions are deoxygenated.

Nonaqueous solvents have been used because of the affinity of silicon dioxide for water and because residual nonaqueous solvents can readily be detected through observation of the carbon 1s photoelectron line in the XPS spectrum. After examination of a number of different solvent systems, anhydrous ethanol was chosen for these experiments by reason of its viscosity, ability to dissolve surface fluoride species, and high volatility. Saturated ethanalic hydrogen fluoride solutions are prepared by bubbling anhydrous hydrogen fluoride gas through deoxygenated ethanol. These saturated solutions are then diluted with additional ethanol to a volume ratio of 10:1. These solutions are observed to give an etch rate of approximately 2 nanometers per milliliter of solution at 15,000 rpm. Following the drop-wise addition of the appropriate amount of etchant, the specimen is rinsed with 10 mL of ethanol and then introduced into the spectrometer introduction lock. After XPS analysis, which includes silicon 2p, oxygen 1s, carbon 1s, nitrogen 1s, and wide scan spectra, oxide film thickness is measured by ellipsometry if the oxidized to elemental silicon intensity ratio in the silicon 2p spectrum is greater than 3 to 1. Significant hydrocarbon and water adsorption occurs during the mounting of the specimen for the ellipsometric measurement, and consequently this method was not used when the spectral intensity ratio could be used to establish the required depth scale.

A diagram of the variable speed spinner is given in figure 16. The system consists of a dry-nitrogen driven turbine which rotates at 10,000 to 100,000 rpm as the gas pressure is varied from 12 to 95 psi (83 to 660 kPa). The turbine chamber is isolated from the spinning head which is enclosed within a TFE-fluorocarbon receptacle to capture etchant and solvent thrown off the spinner surface.

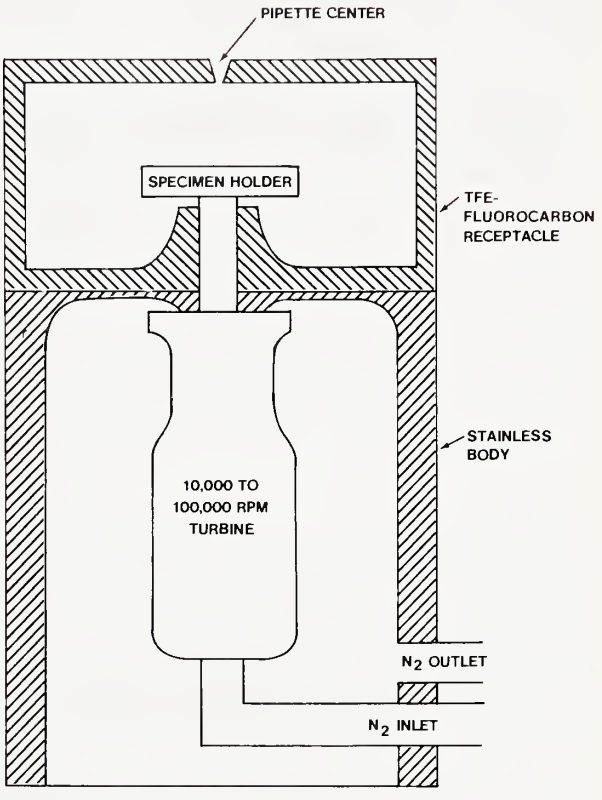

Figure 16. Diagram of variable speed spinner for controlled wet chemical etching.

The spinner is fabricated from polypropylene. The test specimen is held in position by suction created by nozzles drilled into the spinner block.

This wet etching procedure was used to profile a number of silicon dioxide films thermally grown on single-crystal silicon substrates. The etching conditions used in these experiments were designed to remove 1.0 to 2.0 nanometers of oxide per step. The oxygen-to-silicon ratio in the oxide was directly determined through measurement of the oxygen 1s and oxidized silicon 2p intensities in the x-ray photoelectron spectra. A normalized plot of this ratio for a representative film prepared by dry oxidation at 900°C is shown in figure 17. The integrated intensity ratio is effectively 2:1 over most of the film. About 1.5 nm from the silicon-silicon dioxide interface, the ratio appears to change rapidly. In this same region large shifts in the position of the centroid of the oxide peak are also observed which suggests

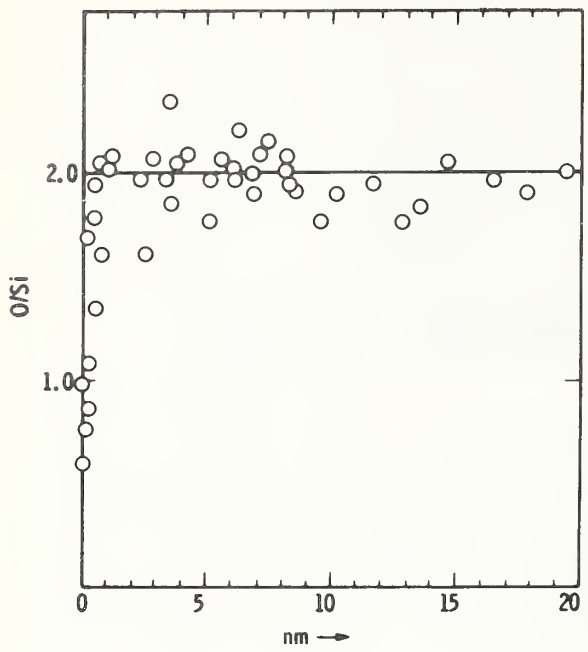

Figure 17. The oxygen-to-silicon ratio in a silicon-dioxide film as a function of distance from the oxide-silicon interface.

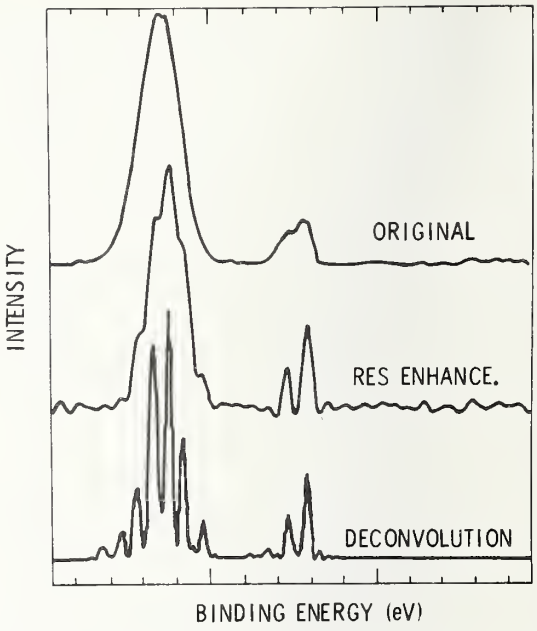

Figure 18. Example of data enhancement techniques. (Upper curve: direct trace of silicon 2p spectrum of a 6-nm thick film of silicon dioxide on silicon; middle curve: resolution enhancement by simple filtering; lower curve: trace enhanced by application of deconvolution computer routines.

that although bulk oxide stoichiometry is maintained throughout most of the film, lower oxides are present in a narrow region next to the interface.

Data Reduction — Work is continuing on the development of data reduction and presentation procedures. The current state of the noise removal and deconvolution routines is indicated in figure 18. The upper curve is a direct trace of the silicon 2p spectrum of a 6-nm thick film of silicon dioxide on silicon. The middle curve shows the resolution enhancement that can be obtained by using a simple filter. The lower curve results from the additional use of smoothing and line-shape constraints.

An algorithm has been developed to facilitate the problem of peak assignment and spectral interpretation in XPS spectra. The algorithm comprises five basic steps: 1) smooth spectrum with cross-correlation filters; 2) locate peak maximum and integrate above background to find intensity; 3) tabulate intensity and binding energy for all peaks with intensity 50 percent greater than the standard deviation of the noise; 4) scan dictionary which contains peak positions and relative intensities of secondary elemental lines; 5) perform intensity and position fitting procedure using a SIMPLEX driver and least-squares criteria.

This algorithm reduces the spectral problem to a sum of delta functions with particular position and intensity. The interrelation of additional lines for a single element, such as 4f, 5s, 4d, 3d, etc., is included. The implementation of the last step includes a procedure for plasmon search. Peaks are assigned in order of decreasing intensity. Following successful assignment, all peaks related to the element are stripped from the table which is then iterated once again.

(F. J. Grunthaner[#])

4.3. Optical Test for Surface Quality of Sapphire Substrates

The results of optical and x-ray analyses on silicon films have been shown to correlate

[#]Work performed at Jet Propulsion Laboratory under NBS Order No. 611377. NBS contact for additional information: K. F. Galloway.

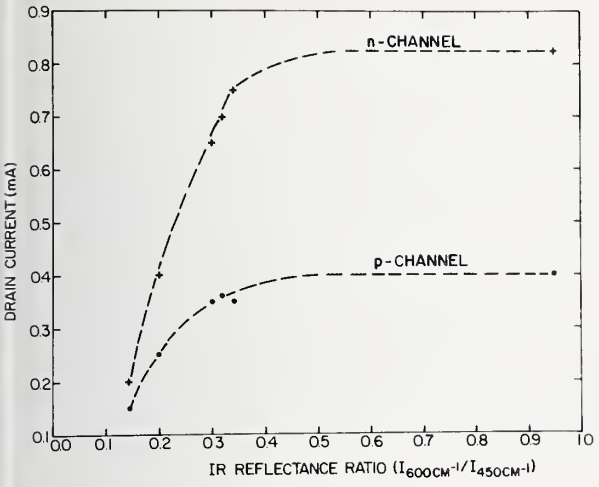

Figure 19. Correlation of SOS MOSFET channel current with infrared reflectance data of corresponding sapphire substrates.

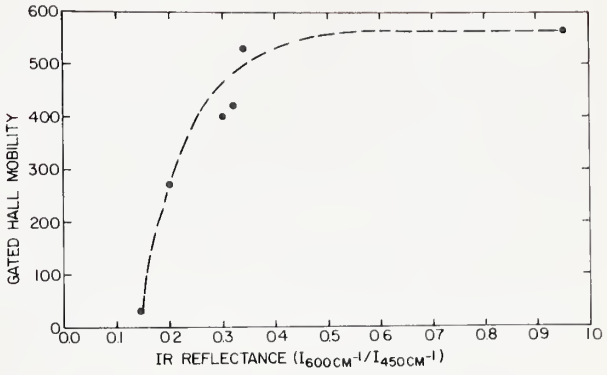

Figure 20. Correlation of gated Hall mobility of SOS structures with infrared reflectance data of corresponding sapphire substrates.

well with the results of optical reflection measurements on the underlying sapphire substrate (NBS Spec. Publ. 400-36, pp. 37-39). The silicon films were subsequently ion-implanted and fabricated into device structures using the test pattern generated under a companion contractural effort (NBS Spec. Publs. 400-19, p. 47, and 400-25, pp. 44-45).

Electrical measurements were performed on *n*- and *p*-channel transistors and on gated Hall bars on each of the several variously polished substrates. Drain current corresponding to a given set of bias conditions on both transistor types is plotted against the infrared reflectance ratio for each substrate in figure 19. The bias conditions were the same in all cases; the source drain voltage was 5 V, and the gate voltage was 10 V, with appropriate polarity applied for each transistor type. Each data point in figure 19 is representative of device performance over a given substrate. It was determined that the threshold voltage was approximately the same for all wafers except for the specimen with the lowest infrared reflectance ratio. Therefore, the drain current is directly proportional to the field effect mobility. It is interesting to note that the current, and therefore the field effect mobility, saturates at a reflectance ratio of approximately 0.5 and that for higher ratios, corresponding to more highly polished substrates, these devices, as operated, do not show a dependence on substrate surface quality. A similar saturation also occurs in the gated Hall mobility, shown in figure 20.

The transistor current and Hall mobility data from figures 19 and 20 are plotted against the ultraviolet reflectance ratio of the silicon films in figures 21 and 22, respectively. The lower the ultraviolet reflectance ratio is, the better the silicon film quality. No saturation trend is observed in these curves and improved device performance, as determined by the parameters measured here, can be expected from improved film crystallinity. However, the data plotted in figures 19 and 20 suggest that substrate surface finishing is not the ultimate limiting factor in determining film quality.

Some comments regarding the data presented here are necessary. The infrared reflectance range shown in figures 19 and 20 corresponds approximately to the range observed (from the worst to the best) among purchased substrates. The substrates used here were deliberately not annealed before silicon epitaxy, except for one which had a good surface initially represented by a reflectance ratio of 0.95. The latter served as a reference with which other specimens could be compared. Annealing the other substrates can be expected to improve device performance, but would obscure a decision on the level of damage tolerable in the substrate polishing process.

The level of damage in the substrates used was not always uniform across the substrate. Consequently, some scatter in the data can be expected. In addition, gated Hall measurements at the silicon film thickness used here (0.6 μm) are complex because of anomalous behavior near zero gate bias [26] and data must be obtained at a bias level suitable for the device being evaluated. This

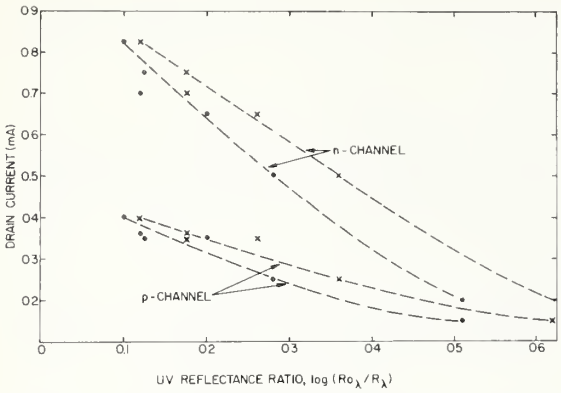

Figure 21. Correlation of SOS MOSFET channel current with ultraviolet reflectance data of corresponding epitaxial silicon films.

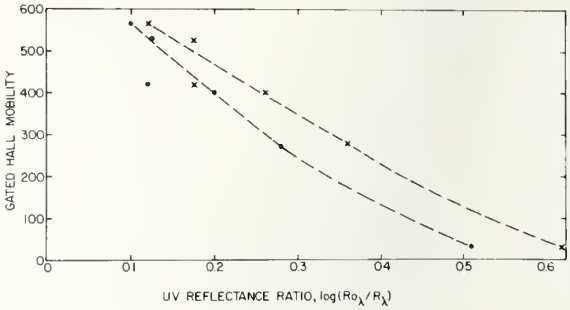

Figure 22. Correlation of gated Hall mobility of SOS structures with ultraviolet reflectance data of corresponding epitaxial silicon films.

means that the devices measured here were not all measured under the same gate bias conditions. Despite these factors, there is a good correlation between the infrared reflectance measurements on the substrates, the ultraviolet reflectance measurements on the epitaxial silicon films, and the electrical properties of the final devices.

(M. T. Duffy[×], P. J. Zanzucchi[×], W. E. Ham[×], and G. W. Cullen[×])

[×]Work performed at RCA Laboratories under NBS Contract No. 5-35915. NBS contact for additional technical information: K. F. Galloway.

5. MATERIALS AND PROCEDURES FOR WAFER PROCESSING

5.1. Sodium Contamination in Oxidation Furnaces*

Thermodynamic calculations aimed at investigating the sodium equilibrium density established at 1000°C in oxidation atmospheres contained in polycrystalline silicon tubes were made [27] as an extension of similar calculations (NBS Spec. Publ. 400-29, pp. 36-37) made in oxidation atmospheres contained in transparent fused silica tubes [28].

Silicon oxidation tubes are prepared by chemical vapor deposition through hydrogen reduction of pure trichlorosilane; this fabrication process made under carefully controlled conditions reduces the inclusion of external contamination. The resulting polycrystalline silicon has a sodium content of about 10 ppb by weight [29] or about 1000 times less sodium than occurs in transparent fused silica oxidation tubes. The low sodium content of polysilicon makes it an excellent wall material to contain oxidation atmospheres.

The equilibrium density of sodium in the oxidation atmosphere in a new polycrystalline silicon tube is about 32 times lower than that of a fused silica tube operated under the same conditions (temperature and water content in the atmosphere) because of the initially lower sodium content in the bulk. However, a silicon oxidation tube tends to develop increased alkali contamination during normal operation unless special care is taken to isolate it from external contamination. At oxidation temperatures, sodium diffuses easily through the wall into the oxidation atmosphere. The sodium may originate from the furnace refractory impurities, the room ambient, or other sources outside the tube. Such contamination is hard to avoid even in clean production-oriented facilities. Further, because oxygen and trace water impurity contained in the oxidation atmosphere react with the tube to form silicon dioxide deposited on the wall, the situation qualitatively approaches the fused silica oxidation chamber condition.

The sodium contamination build-up imposes a need for periodic *in situ* cleaning of silicon oxidation tubes if devices are to be fabricated with oxides which have a low sodium content. The introduction of a dilute hydrogen chloride mixture causes the formation of silicon chloride from the interaction with sodium glasses contained in the silica film formed on the silicon tube wall. At equilibrium, for the case where the cleaning mixture contains 10-percent hydrogen chloride and 0.01-percent water in an inert carrier gas, the equilibrium sodium number density in the atmosphere is 3.66×10^{15} cm^{-3}. This is 10^7 times larger than the equilibrium sodium density normally present in the oxidation ambient. This results in a leaching of sodium from the inner wall of the tube and a reduction in the bulk sodium content below the original level.

Chlorine gas is sometimes used to clean silica tubes since it is somewhat more efficient than hydrogen chloride. However, the use of dry chlorine as a cleaning agent for silicon tubes should be avoided because of the risk involved due to its high reactivity with silicon. The calculations [27] show that the tube could be severely damaged by chlorine if the protective silica film deposited on the inner tube wall has pinholes through which chlorine may come in contact with silicon to produce quantities of gaseous silicon chlorides. If moisture is present in the system, hydrogen chloride is generated, moderating the aggressive behavior of dry chlorine.

The silica film formed on the tube wall can also be removed by a dilute hydrogen atmosphere at oxidation temperature. The formation of water generated through the hydrogen-silica interaction contributes to the leaching of sodium from the tube bulk. If such an atmosphere is maintained in silicon oxidation tubes when they are not being used for semiconductor processing, the sodium impurity from the tube wall bulk and the silica film on the tube are constantly removed from the hot zone. This tube conditioning reduces the need for periodic hydrogen chloride cleaning and consequently minimizes the incidence of other species (such as chlorine) in the oxidation chamber. Experimental evidence shows that chlorine is incorporated into oxide films thermally grown on silicon wafers processed in oxidation tubes previously cleaned with hydrogen chloride [30]. This has proved to result in electrical instabilities under exposure to ionizing radiation [31].

(S. Mayo and W. H. Evans†)

---

*Principally funded by the Defense Nuclear Agency.

†NBS Chemical Process Data Evaluation Section, Physical Chemistry Division.

6. PHOTOLITHOGRAPHY

6.1. Calibration Standards for Optical Photomask Line-Width Measurements

A primary objective of the photomask metrology task is to develop line-width artifacts in the 1- to 10-μm region which can be used by the integrated circuit industry to calibrate optical systems used for measuring line widths on photomasks with transmitted illumination. The first step toward issuance of these artifacts is a collaborative test involving NBS and a limited number of participants from the industry.* This initial collaborative test has as its goals: 1) reduction of known systematic errors resulting from instrument-reading scale offsets; 2) evaluation of residual errors which remain after reducing known systematic errors; and 3) evaluation of the proposed NBS recommended line-width measurement procedure to determine if the procedure is sufficiently well defined to achieve the optimal transfer of measurements from NBS to the user.

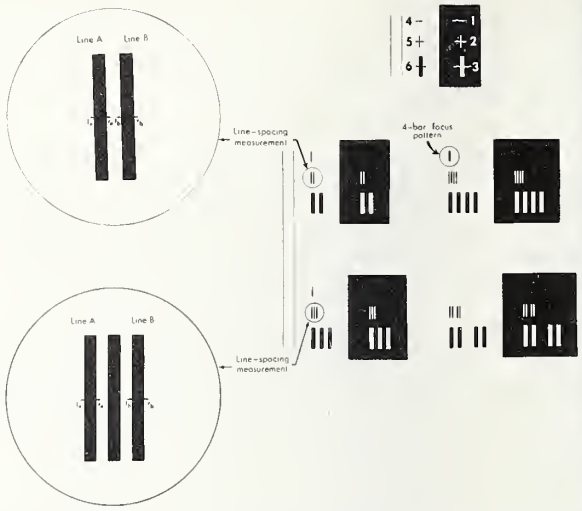

Figure 23. A view of a pattern group on the chromium-on-glass line-width measurement artifact.

In this initial experiment, each participant is to make measurements on lines in two pattern groups of the initial chromium-on-glass artifacts (NBS Spec. Publs. 400-29, p. 53, and 400-17, pp. 37-38). A view of one of the pattern groups is shown in figure 23. The four-bar pattern of 1-μm lines is used for focusing the microscope. The widths of the spaces and lines numbered 1 through 6 are measured at the locations marked by the arrows; measurements of these six patterns plus the adjacent 2-μm line are also made on a second pattern group. Line spacing measurements (both left edge to left edge and right edge to right edge) are made between lines A and B in the two line groups shown in the insets. The measurement procedure for use in the collaborative test is based on a preliminary set of measurements performed at NBS. These measurements, described below, established that the systematic error in line-width measurements resulting from instrument scale offsets could be reduced by an order of magnitude using line-width calibration rather than a conventional line-spacing calibration.

Calibration Measurements — Optical line-width calibrations on these artifacts were made on the NBS scanning photometric microscope (NBS Spec. Publ. 400-29, pp. 50-52) [32]. The important parameters of this image-scanning, transmitted-light optical microscope are: 1) spectrally filtered illumination peaked at 530 nm for optimum optical-image performance; 2) 0.90 objective N.A.; 3) 0.60 condenser N.A. (underfilled); and 4) an effective scanning slit of 0.13 μm by 1.3 μm at the position of the test specimen. The scanning slit remains fixed while the stage moves, and the stage position is monitored with a linear voltage transducer (LVTD) gauge. The digital outputs from the photomultiplier and LVTD gauge are recorded by a microprocessor at position increments of 0.01 μm. The length scale of the LVTD gauge is calibrated using a known center-to-center line-spacing measurement.

The optical line-width calibrations on the artifacts involve measurement of the widths of seven clear or opaque lines in each pattern group measured. Each line is measured nine times, three times a day for three days. For the three measurements made within a single day, the artifact remained in the same place, but the optical system was refocused prior to each measurement. For the day-to-day measurements, the artifact was removed from the system and reinserted, realigned, and repositioned. Table 3 shows a sample of the

---

*During the interval between the end of the reporting period and the issuance of this report, the initial collaborative test has been completed and the results analyzed. A report of the results is given in Swyt, D. A., Rosberry, F. W., and Nyyssonen, D., Calibration of Optical Microscopes for Photomask Linewidth Measurements, *Proc. Microelectronics Seminar — Interface '77*, Monterey, California, October 5-7, 1977, pp. 131-144.

Table 3 — Sample Optical Line-Width Calibration Data

Nominal Line Width, μm	Measured Line Width, μm									Mean, μm	Standard Deviation 3σ, μm
	Day 1			Day 2			Day 3				
	Run 1	Run 2	Run 3	Run 1	Run 2	Run 3	Run 1	Run 2	Run 3		
Opaque Lines											
1	0.82	0.82	0.83	0.82	0.83	0.82	0.80	0.83	0.81	0.82	0.03
2	1.76	1.74	1.75	1.77	1.78	1.81	1.79	1.80	1.79	1.78	0.07
3	2.86	2.84	2.81	2.79	2.75	2.83	2.80	2.79	2.82	2.81	0.10
10	9.27	9.20	9.18	9.18						9.21	0.13
Clear Lines											
1	0.88	0.86	0.89	0.88	0.90	0.89	0.92	0.93	0.93	0.90	0.07
3	3.06	3.05	3.01	3.06	3.08	3.03	3.03	3.01	2.99	3.04	0.09
10	9.54	9.58	9.52	9.52	9.50					9.53	0.09

measurement data on one particular pattern group. Earlier measurement data established that on a high quality, nominally 1-μm wide line, the system was capable of a 3σ variability of 0.025 μm with five measurements on any given day; the 3σ variability could be reduced below 0.01 μm with a total of 30 measurements.

The present data reflect two primary sources of measurement variation. Line-edge quality is reflected in the day-to-day variations as shown, particularly in the measurement of the nominally 2-μm wide opaque line. When replacing the artifact in the measurement system, it is difficult to assure that the measurement is made in exactly the same place because the serrations originally intended for this purpose (NBS Spec. Publ. 400-17, pp. 37-38) do not lie within the field of view. Hence, the visible raggedness in the edge affects the day-to-day measurements. The other source of variation in measurements involves focus. Although initial focusing can be performed extremely accurately, the height variation of the artifact with linear displacement of the stage introduces focus displacements of 0.1 μm or more while scanning over a distance of 10 μm. These displacements may be due to imperfections or dirt in the stage ball bearings. Care was taken to minimize this effect by leveling the stage. Currently, the remaining focus error is corrected in mid-scan (for the 10-μm lines only). This is possible since for a given position of the artifact, the focus error introduced over the length of scan may be determined using the piezoelectric focusing mechanism. As long as the artifact is not moved with respect to the stage, this focus error is repeatable and therefore may be corrected for by application of the correct voltage to the piezoelectric elements. This technique is not altogether satisfactory since the 3σ values are still larger than is desirable. As a long-term solution to this problem, the flexure-pivot stage used in the SEM/interferometer system (see sec. 6.5) [33] is being redesigned with a hole in the middle to accommodate the condenser for the transmitted-light system. It has been tested in reflected light and shows no focus problem over distances of 10 μm or more when properly leveled. (D. Nyyssonen†)

Line-Width Measurements§ — While the underlying premise that proper calibration of microscopes for measuring line widths demands line-width, not line-spacing, standards has not been fully validated, the fundamental inadequacy of line-spacing calibrations has been demonstrated (NBS Spec. Publs. 400-19, pp. 41-42, and 400-29, pp. 53-56) [34]. These results clearly showed a systematic dependence of measured line widths on object, illumination, and measuring-eyepiece types.

The study reported here was undertaken as an initial demonstration of the positive value of using the calibrated line-width as opposed to the line-spacing standard. The standard was a prototype artifact calibrated as described above. The study consisted of: 1) visual-eyepiece measurements (in arbitrary scale units) of the widths of a number of lines; 2) computation of the widths of the lines subsequently designated "unknowns" in

†NBS Optical Physics Division.

§Partially funded through the NBS Dimensional Metrology Program.

terms of the widths of those designated "calibration lines;" and finally, 3) comparison of the widths of the unknowns so computed against the relative widths as measured on the scanning photometric microscope. The study was performed partially blind in that the operator made the visual measurements knowing only the nominal widths of the lines, independent of their designation. Only after completion of the measurements were raw data in scale units converted to dimensional units relative to the photometrically measured line widths.

Measurements were made on both filar and image-shearing eyepiece microscopes. Filtered green light and an objective/condenser numerical aperture ratio of less than one were used by design. With all readings taken in arbitrary scale units, the widths of the five clear spaces were measured, then the widths of the first two spaces remeasured. Similarly, the widths of six opaque lines were measured, with repeat measurements on the first two. Each of the line-width measurements consisted of three individual readings which were averaged to obtain the mean value for the measurement. The entire set of measurements for each group was repeated in three "runs" for each eyepiece.

After completion of the measurements, computations and analysis of the results were performed by a different person. One pair of lines in each of the clear and opaque groups, the pair consisting of one 3-μm wide line and one 10-μm wide line, served as calibration lines. The remaining lines were treated as unknowns. For each individual run of lines of like polarity (clear or opaque), readings in arbitrary units for each eyepiece were converted to dimensional units by linear calibration against the photometrically measured widths of the calibration pair.

For r_1 and r_2, respectively the means of three readings on lines of photometrically measured widths w_1 and w_2, the unknown width w_x corresponding to reading r_x is:

$$w_x = ar_x + b ,$$

where

$$a = \frac{w_1 - w_2}{r_1 - r_2}$$

and

$$b = \frac{w_2 r_1 - w_1 r_2}{r_1 - r_2} .$$

By this calibration relationship, the numerical results of this exercise (shown in tables 4 and 5 for filar and image-shearing eyepieces, respectively) were generated. Included are specific results for each of three runs on clear spaces and opaque lines made with each eyepiece.

The agreement is generally satisfactory. For the filar eyepiece the RMS average difference for all runs is 0.058 μm; because of the large deviations on run 3, the RMS average difference for the measurements on the clear spaces is larger than that for the measurements on the opaque lines. For the image-shearing eyepiece, the RMS average difference for the measurements on the clear spaces is 0.033 μm, and that for the measurements on the opaque lines is 0.099 μm. Despite the relatively large differences obtained in some cases, it is apparent that systematic differences between the two types of eyepieces have been eliminated.

(D. A. Swyt[¶] and F. W. Rosberry[¶])

6.2. Optical Line-Width Measurements on Silicon and Iron-Oxide Photomasks[#]

Optical measurements of line widths on see-through photomasks such as silicon and iron-oxide have posed a problem to both manufacturers and users of photomasks because of the uncertainty involved in locating edges in the complex image structure. The difficulty lies in determining the edge locations in relationship to the dark and bright bands that occur near the edges (NBS Spec. Publ. 400-29, p. 53). Clearly, measurements of line widths made by locating the edge in the center of the dark band yield significantly different values than measurements made using the transition region between the clear area and the dark band or even between the dark band and the adjacent bright band. In order to determine the true edge location, an accurate description of the optical system, illumination, and photomask is required, and the phenomena which give rise to the banding must be understood.

[¶] NBS Optics and Micrometrology Section, Mechanics Division.

[#] Funded through the NBS Optical Physics Division.

Table 4 — Comparison of Filar-Eyepiece Measurements With Scanning Photometric Microscope Measurements of the Same Lines When the Eyepiece is Calibrated Against the Photometric System

Line Type	Line Number[a]	Photometric Line Width, μm	Visual Line Width, μm		
			Run 1	Run 2	Run 3
Clear Spaces:					
Unknowns	3	0.78	0.78	0.78	0.69
	4	2.98	2.99	3.01	2.85
	5	10.10	10.08	10.15	10.19
Calibration (Check)	1	2.98	3.02	2.98	2.97
	2	10.17	10.13	10.17	10.33
Opaque Lines:					
Unknowns	8	0.96	0.88	0.88	0.93
	9	1.86	1.83	1.90	1.87
	10	2.96	3.01	2.99	3.00
	11	10.03	9.96	9.92	10.02
Calibration (Check)	6	3.00	2.99	2.96	2.96
	7	9.95	9.99	9.94	9.95

[a]The line numbering system in this experiment is different from that shown in figure 23 which was used in the initial collaborative test.

Table 5 — Comparison of Image-Shearing Eyepiece Measurements With Scanning Photometric Microscope Measurements of the Same Lines When the Eyepiece is Calibrated Against the Photometric System

Line Type	Line Number[a]	Photometric Line Width, μm	Visual Line Width, μm		
			Run 1	Run 2	Run 3
Clear Spaces:					
Unknowns	3	0.78	0.77	0.79	0.77
	4	2.98	2.97	2.97	2.96
	5	10.10	10.17	10.16	10.16
Calibration (Check)	1	2.98	2.96	2.98	2.98
	2	10.17	10.16	10.21	10.18
Opaque Lines:					
Unknowns	8	0.96	1.09	1.08	0.97
	9	1.86	2.05	2.05	1.95
	10	2.96	3.05	3.11	2.99
	11	10.03	10.03	9.95	9.94
Calibration (Check)	6	3.00	3.05	3.06	2.94
	7	9.95	10.03	9.97	9.92

[a]The line numbering system in this experiment is different from that shown in figure 23 which was used in the initial collaborative test.

For see-through masks the image structure is quite different from that of the previously analyzed opaque masks (NBS Spec. Publs. 400-29, pp. 50-52, and 400-36, pp. 42-44) [32], although the optical system parameters have remained the same. The change which must be made in the mathematical model of the system is in the complex amplitude transmittance function t(x). For chromium-on-glass photomasks, which have a transmittance of a few percent or less, the complex amplitude transmittance was taken as real and the phase retardation of the material ignored. However, for see-through masks, there is an optical path difference between light transmitted through the clear and the semi-opaque portions of the photomask. The resulting phase difference in transmitted light is given by

$$\phi = k(n_o - 1)d \ , \qquad (9)$$

where k is the wave number, n_o is the index of refraction of the mask material, and d is the mask thickness. The complex amplitude transmittance must, in the general case, include this phase as well so that

$$t(x) = t_o(x)e^{i\phi(x)}$$

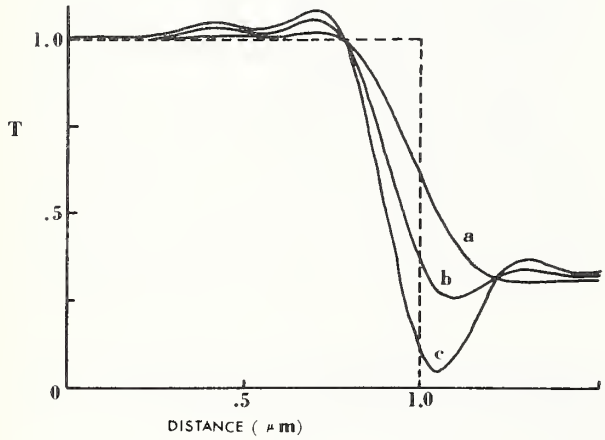

a. 0.60 condenser N.A., T_o = 0.31, ϕ: (a) 0, (b) $\pi/2$, and (c) π.

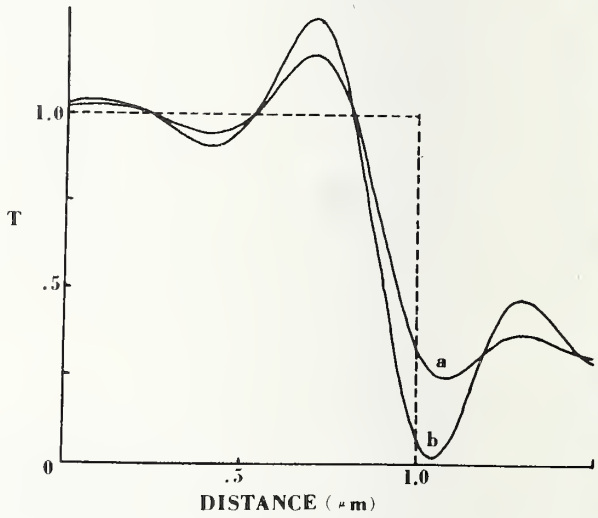

b. 0.22 condenser N.A., T_o = 0.31, ϕ: (a) $\pi/2$, (b) π.

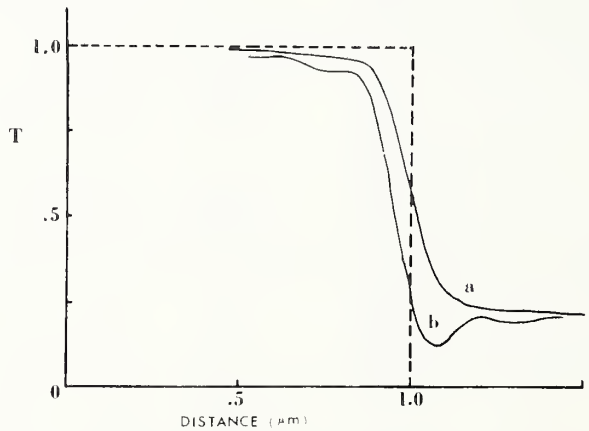

c. 0.90 condenser N.A., T_o = 0.21, ϕ: (a) 0 and (b) π.

Figure 24. Computed image profiles of a 2-μm clear line for an objective lens with numerical aperture of 0.90 and various condenser lenses and phase shifts.

Image profiles and associated parameters were computed for several cases of interest [35]. Figure 24 illustrates the computed image profiles for an objective numerical aperture of 0.90 and varying condenser aperture for the background transmittances and phases indicated. In the course of generating these image profiles, Kintner introduced a new, faster computation method based upon a Fourier-series expansion of the object and computation of the transmission cross-coefficient which characterizes the combined condenser and objective system [36,37]. This method, which is discussed in connection with dark-field imaging (see sec. 6.3.), is outlined in Appendix C. It enables a reduction in computer time of up to an order of magnitude in some cases along with a slight improvement in accuracy with phase included in the complex amplitude transmittance of the object.

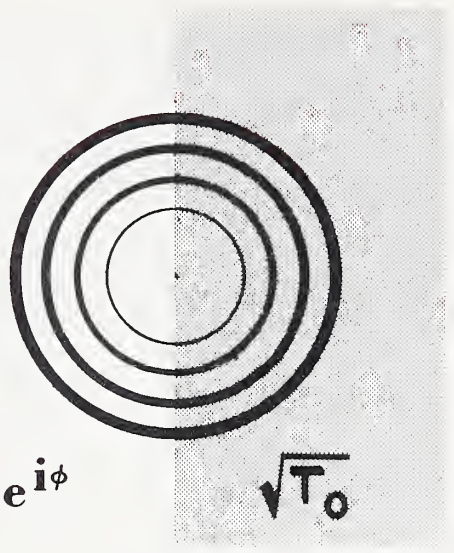

Figure 25. Schematic illustration showing method of computing threshold at edge with phase shift present.

Because the transmittance threshold, T_c, which corresponds to the edge location (denoted by the dashed lines in fig. 24) varies with the amount of phase present as well as the background transmittance of the photomask material, a new expression must be derived for the proper transmittance threshold to be used to establish the edges of the line being measured. As in the case of nearly opaque masks (NBS Spec. Publ. 400-36, pp. 42-44) [32], when a symmetrical impulse response is centered at the edge between two materials, as shown in figure 25, in coherent illumination the threshold at the edge is the ratio of the transmittance computed at this position with respect to the transmittance of the clear area. With a phase change present, T_c becomes, in coherent limit,

$$T_c = 0.25\ (1 + T_o + 2\sqrt{T_o}\cos\phi)\ , \qquad (10)$$

where T_o is the relative transmittance of the semi-opaque areas of the mask with respect to the transmittance of the clear area and ϕ is given in eq (9) for transmitted light. Partially coherent imaging systems are extremely sensitive to phase changes; for eq (10) to apply, the condenser aperture must be less than it was for the case of nearly opaque masks. Table 6 gives values of T_c for a variety of cases. The values for the case of coherent light were computed from eq (10);

Table 6 — Computed Thresholds Corresponding to Edge Location

T_o	ϕ	R = N.A.$_{condenser}$/N.A.$_{objective}$					
		∞ (incoherent)	1.00	0.66	0.44	0.24	0 (coherent)
0	0	0.50	-	0.27	0.24	0.23	0.25
0.21	0	0.61	0.56	0.53	-	-	0.53
0.21	$\pi/2$	0.61	0.41	0.31	-	-	0.30
0.21	π	0.61	0.26	0.07	-	-	0.07
0.31	0	0.66	-	0.61	-	-	0.61
0.31	$\pi/2$	0.66	-	0.36	0.35	0.33	0.33
0.31	π	0.66	-	0.10	0.08	0.06	0.05

Table 7 — Line-Width Errors Resulting from Locating the Edges at the Center of the Adjacent Dark Band

T_o	ϕ	Objective N.A.		
		0.90	0.60	0.45
0.21	$\pi/2$	0.20 μm	0.31 μm	0.41 μm
0.21	π	0.11	0.17	0.22
0.31	$\pi/2$	0.16	0.24	0.32
0.31	π	0.08	0.13	0.17
1.00	any	0	0	0

values for the other cases were found from the computed image profiles.

In microscopes which do not produce a photometric image profile and cannot, therefore, determine the proper threshold, it is of interest to know the magnitude of the error which results from locating the edge at the center of the dark band which is the most repeatable setting for a filar eyepiece. Table 7 shows the magnitude of this error computed for various values of T_o, ϕ, and objective and condenser numerical apertures [35].

(D. Nyyssonen†)

6.3. Optical Line-Width Measurements in Reflected Light×

Another major goal of the photomask metrology task is the extension of the capability for measuring line widths in the 1- to 10-μm region to include measurements in reflected light. Early in the effort it was recognized that measurements made in reflected light are more difficult to characterize than those made in transmitted light on black-chromium photomasks. Several factors contribute to these difficulties. The reflectance of the materials is much lower than the transmittance resulting in lower signal-to-noise ratio in the photomultiplier output of the scanning photometric microscope. The differences in reflectances are also lower, thereby producing lower contrast imagery. Therefore, the optical-path differences between light reflected from the various parts of the test specimen become important in determining edge locations. The study of transmittance measurements of see-through photomasks (see sec. 6.2.) indicates that the edge image profiles change drastically along with the threshold corresponding to edge location. In addition, it is expected that the measurements would be affected both by the surface characteristics of the materials and by the thickness of the line-carrying layer in relation to the depth of focus of the microscope.

Evaluation of Bright-Field and Dark-Field Reflected-Light Systems — One of the two illumination systems, bright field or dark field, is generally used for viewing objects in reflected light with a microscope. The bright-field system, illustrated schematically in figure 26a, uses a beam-splitter to direct the illumination onto the objective which, in turn, focuses the illuminating aperture onto the object. When unfolded, this system corresponds to a transmitted-light system with matched numerical apertures for condenser and objective. Such a system is partially coherent and sensitive to phase (optical-path) differences in the object. Since there is no analytic expression to relate edge location to transmittance threshold, this system is a poor choice for line-width measurements of the desired accuracy.

In the dark-field system, shown schematically in figure 26b, the illuminating condenser aperture is annular, with an inner radius corresponding to, or greater than, the numerical aperture of the objective. The outer radius is usually as large as practicable in order to gain the maximum flux at the detector. This system, when unfolded, may be analyzed using the theory of partial coherence as was done in the case of transmitted-light systems [32]. However, because the thin, annular condenser aperture has a numerical aperture greater than that of the objective, a two-dimensional analysis must be made. The computation method used in earlier calculations is prohibitively time-consuming for two-dimensional computations, but fortunately the new method of computation introduced by Kintner [36,37], discussed below, reduces the computation time by nearly an order of magnitude; this reduction makes accurate analysis of dark-field imagery feasible.

(D. Nyyssonen†)

Computation of Dark-Field Line Images — The calculation of the image intensity distribution in a partially coherent imaging system is, in general, a difficult task. It can be

†NBS Optical Physics Division.

×Principally funded by the Naval Ocean Systems Center.

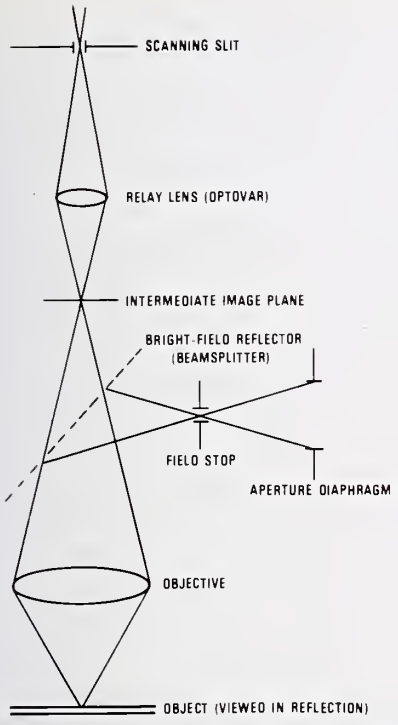

a. Bright-field, reflected-light system.

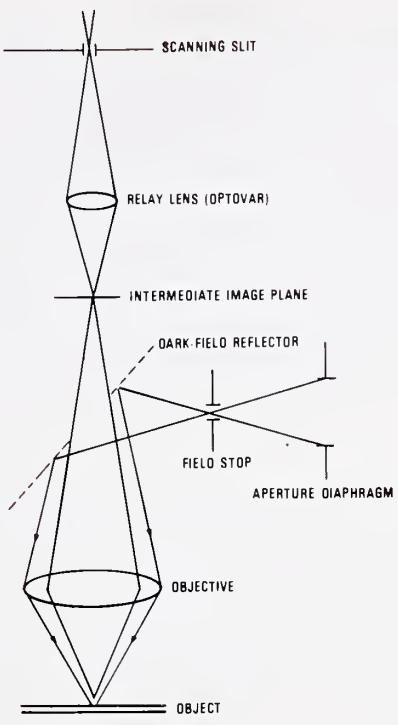

b. Dark-field, reflected-light system.

Figure 26. Schematics of optical microscope systems.

simplified by describing the system in terms of a dimensionless abstract model which takes advantage of the properties of the Fourier transform and by making certain particular assumptions about the form of the object being imaged. In particular, if the object function varies in one dimension only, if the object function is assumed to be periodic, and if the image plane is sampled by a scanning slit, the intensity spectrum observed is given by

$$I_s(\xi) = \frac{\sin(\pi w \xi)}{\pi w \xi} \cdot I(\xi) \ , \qquad (11)$$

where ξ is the geometrical coordinate in the pupil plane divided by the numerical aperture of the objective lens, w is the full width of the scanning slit in dimensionless coordinates (actual width multiplied by the numerical aperture of the objective lens and divided by the wavelength of the light), and $I(\xi)$ is the image spatial frequency spectrum in the pupil plane. It should be noted that a non-periodic object may be expressed in terms of a periodic model if a large period is chosen so that the object is effectively isolated and does not interfere with its neighbors. The model and the derivation of eq (11) are outlined in Appendix C.

(E. C. Kintner[+])

Comparison of Calculated and Experimental Dark-Field Image Profiles — Line images were calculated from eq (11) for comparison with image profiles experimentally measured with dark-field illumination. One of the difficulties in comparing theoretical and experimentally measured image profiles is determination of the radii of the annular condenser illuminator. For the available transmitted-light, dark-field systems, the numerical apertures of the annuli were available in the literature. However, for reflected-light systems with a reflecting annular illuminator built into the objective, the radii of the annuli could only be estimated from the physical dimensions.

Images of 1-, 2-, and 5-μm wide clear lines were calculated for the case of an objective lens with a numerical aperture of 0.60 and an annular condenser aperture with inner and

[+]NBS-NRC Postdoctoral Research Associate, NBS Optics and Micrometrology Section, Mechanics Division.

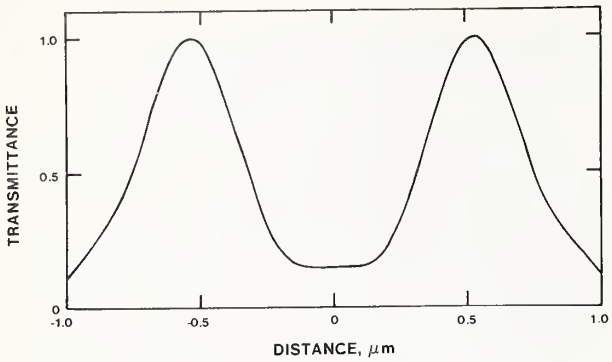

a. 1-μm clear line.

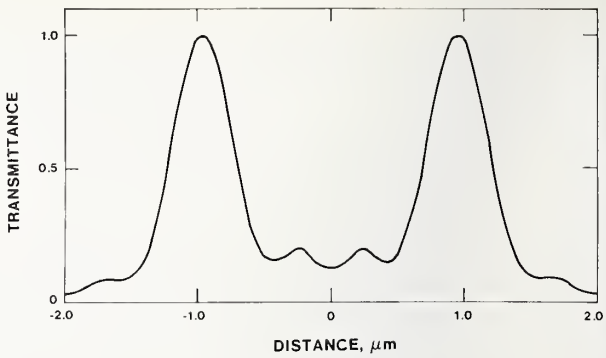

b. 2-μm clear line.

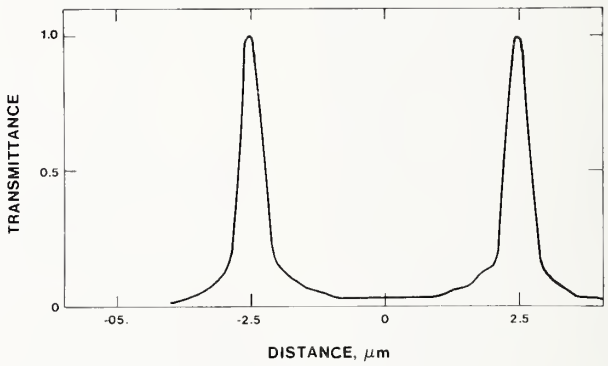

c. 5-μm clear line.

Figure 27. Theoretical dark-field image of clear lines for 0.60 objective N.A. and 0.80 to 0.95 condenser N.A.

outer radii corresponding to numerical apertures of 0.80 and 0.95, respectively. The calculated profiles, shown in figure 27, have the observed bright band at the edge of the line which is frequently used to make linewidth measurements. However, the peak of this bright band does not always coincide with the edge as is generally assumed. Other calculations show that the peak displacement is independent of phase difference and background transmittance of the photomask material. It is therefore possible to plot a calibration curve for a given condenser and objective combination; this curve relates the line width measured peak-to-peak to the true line width as shown in figure 28. This plot varies with the numerical apertures of the condenser and objective and is dependent on the optical aberrations of the system (a diffraction limited optical system is assumed).

Experimentally determined image profiles in the transmitted-light, dark-field case were found to be similar to the calculated profiles. However, reflected-light, dark-field imagery is much less satisfactory principally because of the low light level in the image plane and the resulting poor signal-to-noise ratio. This limitation, combined with the nonlinear calibration relation (fig. 28) led to the decision not to use reflected-light, dark-field illumination as a method for calibrating lines on wafers.

Optimum Line-Width Measuring System — Since neither conventional reflection system seemed to be a desirable optical calibration system, other possible systems were examined. Based on the large amount of information and research available on the transmitted-light system, an optimum choice would be the reflection analog of that system. The major modification which must be made to conventional reflection systems is the restriction of the illuminating aperture to a diameter less than that of the imaging system. This can be

achieved by using a conventional bright-field system but closing down the aperture diaphragm to yield a suitable value of the ratio R of the numerical aperture of the condenser lens to that of the objective lens. Investigations on semi-opaque photomasks (see sec. 6.2) have shown that the coherent limit for the threshold corresponding to the edge location, given in eq (10), is appropriate when R is less than 0.45 provided that the phase change is $\pi/2$ rad or less. It is desirable to use this aperture for most measurements to maintain reasonable signal-to-noise levels in the photomultiplier output. However, for phase changes approaching π rad the value of R must be reduced to 0.25 or less for the coherent limit to apply. Note that in reflection, the phase difference is not in general the same as that for transmitted light, as given in eq (9), but is given by

$$\phi_R = 2kd + \phi_o \ , \qquad (12)$$

where k is the wave number, d is the thickness of the defining film on the substrate, and ϕ_o is the difference in the phase change on reflection at the film surface and at the substrate which is dependent upon the materials. To determine the proper threshold, it is necessary to know the phase change ϕ_o or ϕ_R. In reflected light, ϕ_o may be determined by using a microscope intereference objective of the Watson-Barnett type and measuring the fringe displacement. Figure 29 shows a photograph of such a fringe pattern for an iron-oxide photomask. The white-light, zero-order fringe must be used to determine the direction of fringe displacement. (D. Nyyssonen†)

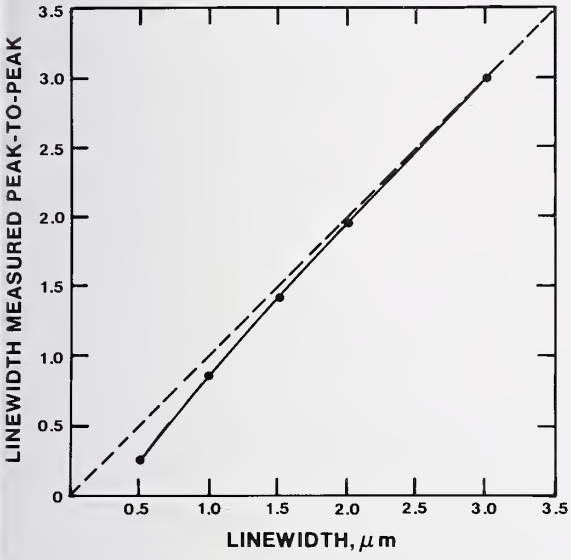

Figure 28. Theoretical calibration curve for dark-field illumination, line width measured between peaks *versus* true line width for 0.85 objective N.A., 0.85 to 1.00 condenser N.A., and diffraction-limited optics.

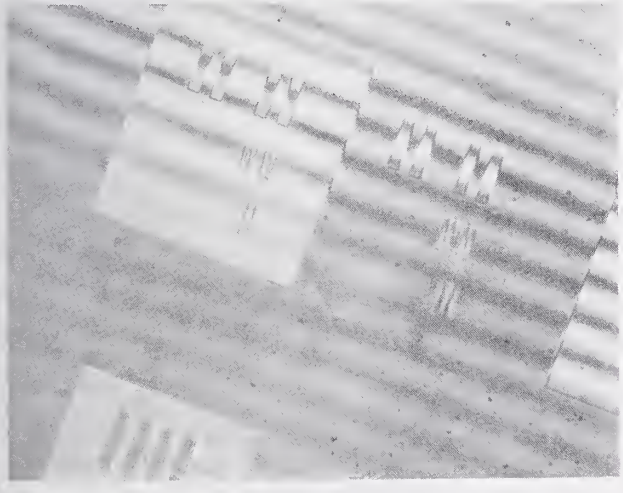

Figure 29. Interference image of an iron-oxide artifact as seen in a Watson-Barnett interference attachment for the microscope. (Optical path differences on reflection from iron-oxide as compared to glass substrate introduce a phase change of approximately 0.7 λ.)

6.4. Submicrometer Line-Width Measurements×

Although primary interest until recently has been on line widths in the 1- to 10-μm region, there is now strong interest in exploiting optical line-width-measurement capability below 1 μm. Edge profiles of submicrometer clear lines on an opaque background were computed [38]. For relatively wide clear lines on an opaque background, the 25-percent relative intensity transmittance point corresponds with the true edge location. However, as the width of the line becomes smaller, this threshold point starts to deviate slightly from the true edge location as illustrated in figure 30. This deviation results in a small error if the 25-percent threshold is employed. Similar deviations occur for measurements on partially transparent back-

†NBS Optical Physics Division.

×Principally funded by the Naval Ocean Systems Center.

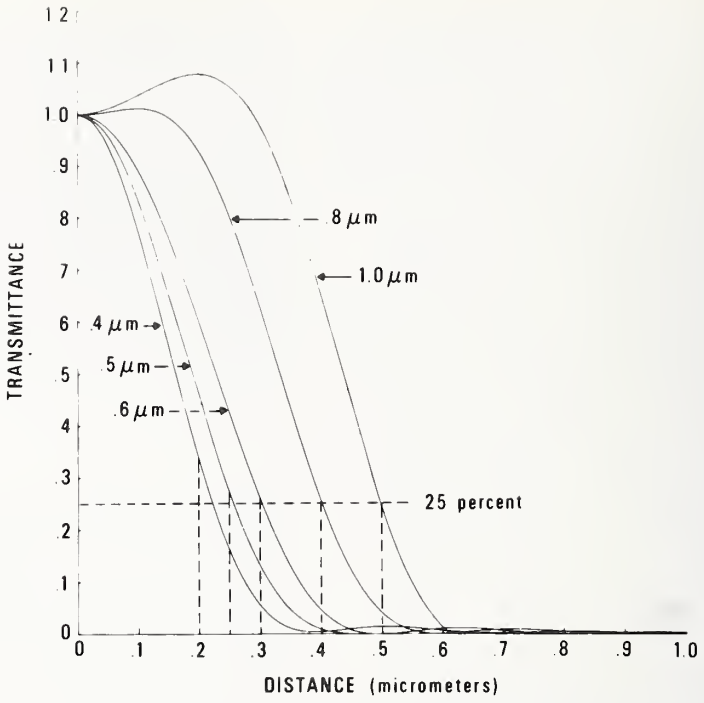

Figure 30. Theoretical image profiles of submicrometer clear lines from 0.4 to 1.0 μm wide on an opaque background for the optical scanning photometric microscope. (Vertical dashed lines indicate respective edge locations. Intersection of 25-percent threshold line with respective curves indicates where system would locate edge.)

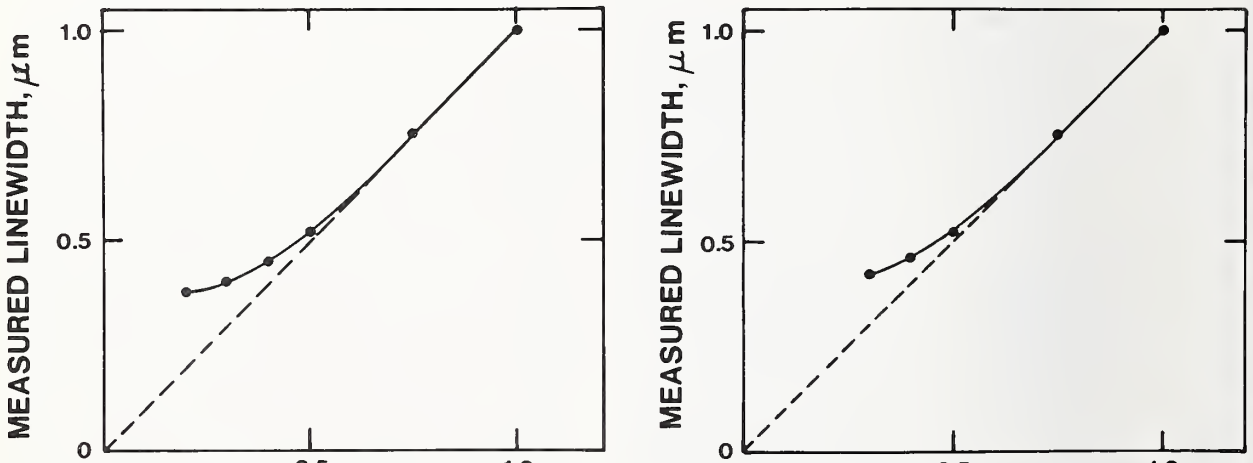

a. Isolated clear lines.

b. Adjacent lines and spaces of equal width.

Figure 31. Theoretical calibration curves for line-width measurements on chromium/chromium oxide artifacts for 0.60 condenser and 0.90 objective N.A. (33.5-percent threshold used for measurement based on 2.5-percent background transmittance, no phase change.)

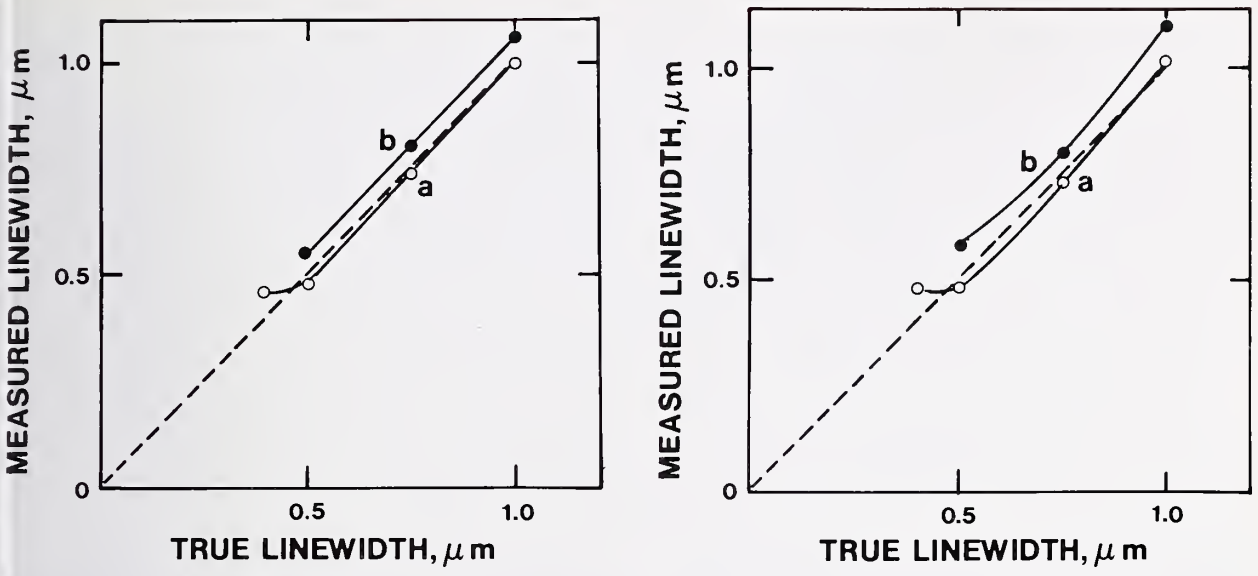

a. Isolated lines.

b. Adjacent lines and spaces of equal width.

Figure 32. Theoretical calibration curves for line-width measurements on see-through photomasks or wafers with 31-percent background transmittance or reflectance. (Curve a: $\pi/2$ phase change with line width measured at 32.8-percent threshold; curve b: π phase change with line width measured at 4.8-percent threshold. Condenser N.A.: 0.40; objective N.A.: 0.90.)

grounds or reflecting surfaces, in which cases the threshold is given by eq (10) (see sec. 6.2.). Calibration curves to relate measured line width employing the 25-percent threshold criterion to actual line width were computed for several cases of interest as shown in figures 31 and 32.

For isolated lines on black-chromium photomasks, measurements can be made on lines as narrow as 0.4 μm; as shown in figure 31a, the error in line width is 0.02 μm for a 0.5-μm and increases to 0.05 μm for a 0.4-μm line. There is no significant difference between the edge location for multiple lines and that for isolated lines; the calibration curves differ by less than 0.01 μm for a line 0.4-μm wide. For specimens with a higher transmittance (or reflectance) background and phase differences present, measurement capability extends to 0.5 μm and abruptly dies out. There is still image detail present, but the curves are changing so rapidly that the threshold corresponding to edge location for larger line widths can no longer be used. The curves in figure 32 are plotted for a condenser numerical aperture of 0.40 and an objective numerical aperture of 0.90. This choice of condenser aperture is poor for specimens with phase differences of π rad. When the condenser numerical aperture is reduced to 0.22, the curves for a phase difference of π rad become the same as the curves for a phase difference of $\pi/2$ rad. Again, there are no significant differences between the edge location for multiple and isolated lines.

Although these theoretical images agree with the imagery seen experimentally, they do not include the effect of edge slope; an ideal edge of infinite slope has been assumed. The effect of edge slope needs to be explored, and a comparison of optical measurements on submicrometer lines with SEM measurements on the same lines must be performed to verify the calculated calibration curves.

In the above discussion, it was assumed that the test object was located at the position of best focus; no aberration term for defocus was included in the computations. Examination of the optical imagery in the microscope showed that with phase differences present, the imagery going through focus is not symmetric with respect to best focus. A complete reversal of image polarity can occur going through focus. For isolated lines, best focus occurs when the edge profile has the steepest slope, but for multiple lines and spaces, this criterion cannot be used. In the latter case, best focus appears to occur when the transmittance at the center of the line or space (whichever is lower transmittance or reflectance) reaches the same

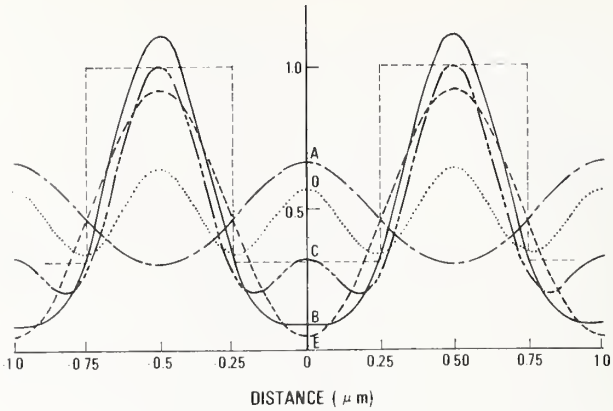

Figure 33. Theoretical image profiles as a function of focus position of adjacent 0.5-μm lines and spaces for T_o = 0.31 and ϕ = $\pi/2$. (Dark dashed line (C) is best focus; (A): $-\lambda/2$; (B): $-\lambda/4$; (D): $+\lambda/4$; (E): $+\lambda/2$.)

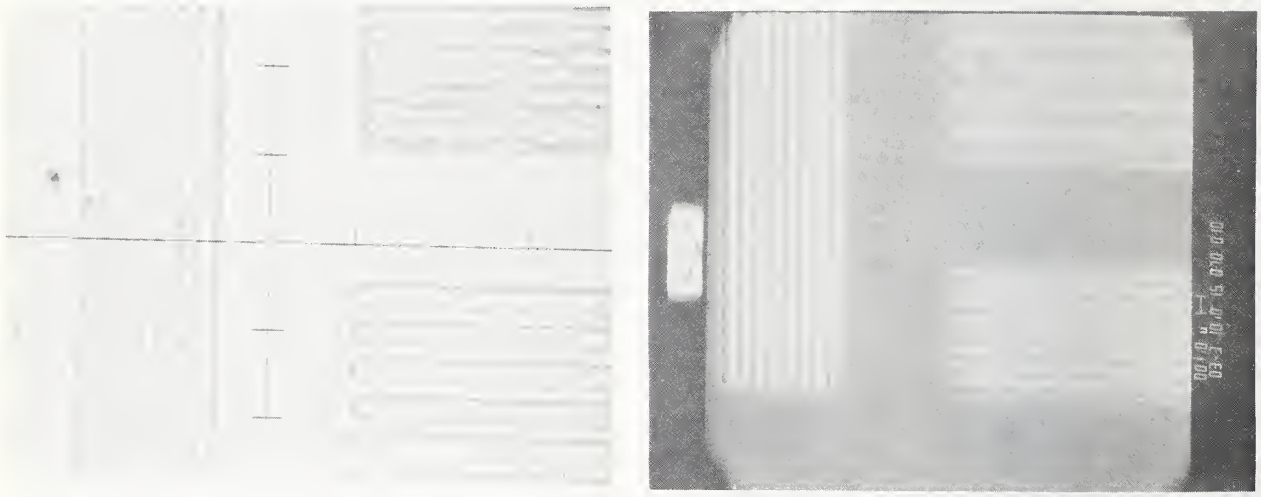

a. Viewed with optical scanning photometric microscope.

b. Viewed with scanning electron microscope used for line-width measurement.

Figure 34. Photomicrographs of a portion of resist pattern on a wafer showing nominal 0.5-μm lines and spaces (smallest pattern).

relative background transmittance level as the larger semi-opaque or clear areas of the test object. This case is illustrated in figure 33. This criterion for best focus requires scanning over longer distances which, in turn, puts severe requirements on maintenance of focus. The accuracy and repeatability of this method remains to be verified experimentally.

Preliminary measurements were made on an exposed resist pattern on a silicon wafer which contained 0.5-μm wide lines and spaces.** This wafer was examined in both the scanning electron microscope (SEM)†† and optical line-width-measuring systems. Figure 34 shows samples of optical and SEM imagery of the best pattern on the wafer. In the optical image, a dark line occurs along the edges of the pattern, but in the SEM image a bright line occurs in the same place. The pictures are mirror images of the same portion of the same line groups and show that the 0.5-μm

** This specimen was supplied by the Naval Ocean Systems Center.

†† Scanning electron micrograph made by W. J. Keery.

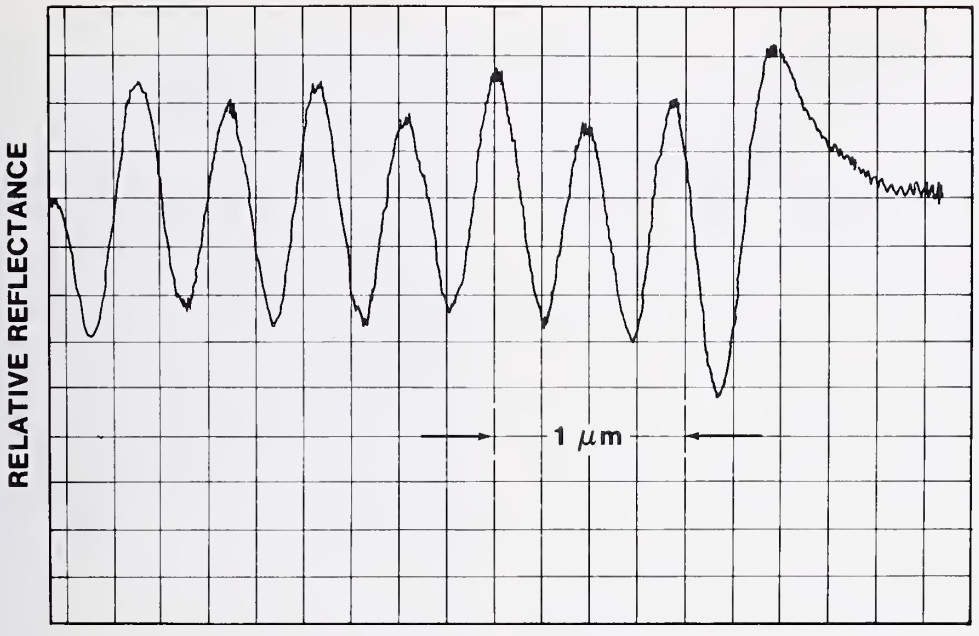

Figure 35. Experimental image profile of nominal 0.5-μm lines and spaces in resist on a wafer before carbon coating. (Reflection optical microscope is analog of transmittance line-width measuring system with illuminating numerical aperture determined by leaf diaphragm set to R ≈ 0.5.)

wide lines are well resolved optically. Before the scanning electron micrographs were taken, this pattern was scanned in the scanning photometric microscope system. For the image scan shown in figure 35, the system was operated in the reflection mode with the leaf aperture diaphragm shut down to between 0.6 and 0.7 times the aperture of the objective. At this time, the problem of determining best focus was identified; before an objective criterion for determination of best focus was developed, the resist pattern was overcoated for examination in the SEM. Subsequent measurements revealed that the carbon coating had affected the reflectance properties of the wafer in such a way that determination of best focus was virtually impossible and no measurements could be made. This result established the necessity of making all optical measurements on test wafers before carbon coating. (D. Nyyssonen†)

6.5. Primary Line-Width Calibration§

To relate the generally unaccessible defined unit of length (wavelength of radiation from krypton 86) to an accessible artifact for the user, several calibration measurements must generally be successively linked. In the first stage of the line-width calibration process, the physical standard for the defined unit of length is related to the width of a material line on a photomask-like artifact by means of a primary measurement system which includes a polarization interferometer located in a scanning electron microscope (SEM) (NBS Spec. Publ. 400-19, p. 43). The wavelength of the interferometer laser is monitored by comparison with the radiation wavelength from a stabilized laser which, in turn, is compared with the krypton radiation.

This primary measurement system is too time-consuming and costly for the routine calibration of user artifacts. Therefore, in the second stage of the process a secondary measurement system is used to relate the line widths calibrated by the SEM/interferometer on the first artifact to line widths on the user artifact. The secondary measurement system is a scanning photometric optical microscope with modifications for optimal performance (NBS Spec. Publ. 400-29, pp. 50-53) [32]. In the third stage, the line widths calibrated by the secondary measurement system are related to the readouts of a line-

†NBS Optical Physics Division.

§Partially funded through the NBS Dimensional Metrology Program.

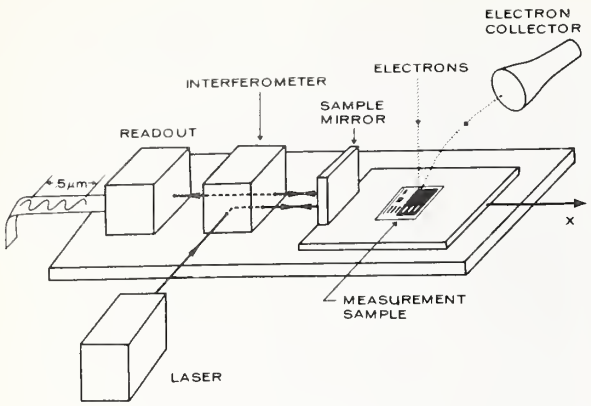

Figure 36. Schematic of the SEM/interferometer system.

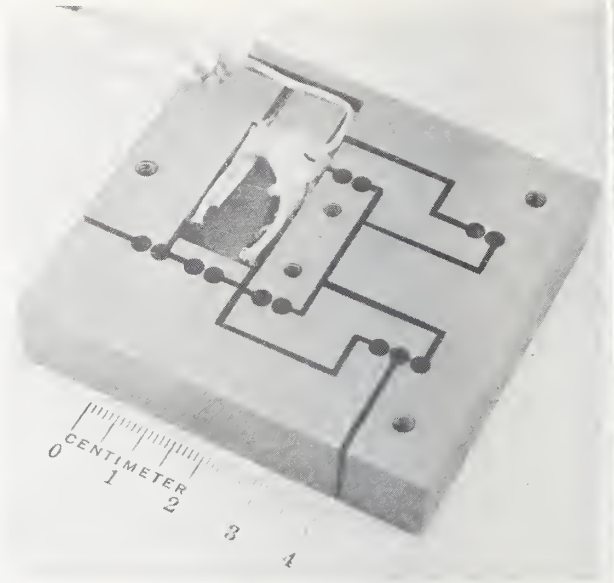

Figure 37. Photograph of scanning stage with flexure-pivot system. (Stage is fixed at points A, while other stage sections move; F - flexure pivot, P - stack of piezoelectric elements, and S - specimen mounting area.)

width measurement system, such an an optical microscope, used in the field. Finally, the user makes measurements of unknown photomask line widths with this calibrated instrument.

In the primary measurement system [33], shown schematically in figure 36, a very small beam of electrons, nominally a few tens of nanometers in diameter, is focused at normal incidence on the test specimen and remains relatively stationary as the test specimen is moved. A double-pass polarization interferometer records the motion of the test specimen as the latter is moved under the beam; the locations of the line edges are detected by the change in SEM signal which arises from differences in the secondary-electron emission coefficients of the various materials.

In this system, the SEM is used as a very fine fiducial mark or cross hair for locating the line edges. Since conventional SEMs are not designed to operate in this mode, a number of compromises have been made in the operation of the SEM. These compromises include: 1) replacing the normally used stage with a specially designed stage assembly consisting of two substages for moving the test specimen, 2) operating the electron beam in a line-sweep mode with approximately 1-μm sweep length on the test specimen, and 3) operating the SEM at 10 keV to reduce contamination buildup on the test specimen (even though a higher operating voltage would give a smaller effective electron-beam diameter).

One of the two substages uses two piezoelectric drivers with orthogonal motions to position the test specimen over a 10-mm by 10-mm area in the SEM field of view. The other substage is a mechanical flexure-pivot stage which moves the line from one edge to the other; this stage has a maximum travel of about 60 μm and a smoothness of better than 0.001 μm over a few micrometers. A photograph of a flexure-pivot stage is shown in figure 37. This stage uses a stack of piezoelectric elements to drive the stage at one point and, by means of flexure-pivot lever arms, the original movement is magnified about 20 times.

A sample plot of the output from the two data channels of the SEM-interferometer is shown in figure 38. The SEM and interferometer data are shown with respect to the same linear time base; the interval between successive data points is 1 ms. The SEM output signal is used to determine the line-edge locations so that the line width, or the separation of the line edges, can be related to a number of whole fringes plus fringe fractions from the interferometer output signal. Therefore, the electron interaction with the material line must be modeled in order to specify accurately the true line-edge locations from the SEM signal or edge trace.

An illustration of the line edge which is assumed in the model is shown schematically in figure 39a. The line edge is a linear ramp rising at an angle ϕ from the glass substrate to the top of the chromium-oxide layer on a

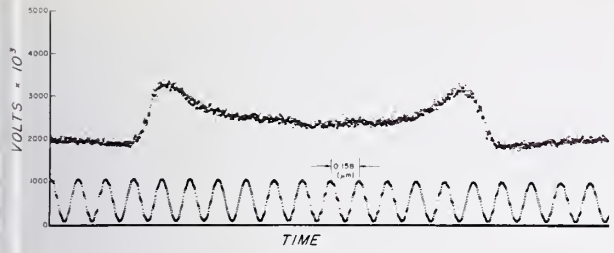

Figure 38. Direct output of the SEM and interferometer data channels for a nominally 2-μm wide opaque line.

black-chromium artifact. The incident electron beam is assumed to have a Gaussian distribution of electrons. For the model, it is necessary to specify a value of ϕ, the diameter of the electron beam, the thickness of the chromium/chromium-oxide layer, and the secondary-electron emission coefficients of the glass substrate, chromium, and chromium oxide. In order to get a match between optical and SEM measurements, the line-edge location is defined as the point on the line slope corresponding to a 25-percent intensity transmittance (50-percent amplitude transmittance). A line-edge trace calculated from this model is compared with an experimental SEM trace in figure 39b. The following parameters were used in the calculation: electron beam diameter, 70 nm; thickness of chromium/chromium dioxide layer, 110 nm; ϕ, 55 deg; secondary-electron emission coefficients for the glass substrate, chromium, and chromium oxide, 1.0, 1.026, and 1.265, respectively. The model fits the data well in the region of the edge, but in the region past the edge on the chromium-oxide side, the SEM output does not fall off as rapidly as the model predicts.

Measurements of the widths of clear and opaque lines on a black-chromium artifact were made with both the SEM/interferometer system and the scanning photometric optical microscope. Typical results are given in table 8 which lists the mean values of a series of measurements. Based on other experimental data, the 3σ limits associated with repeated measurements on a single occasion are 0.016 μm for the SEM/interferometer and 0.025 μm for the optical microscope.

There is essentially no difference in the mean values for the opaque lines as measured on the SEM/interferometer and optical microscope. For the clear lines, however, the differences are 0.13 μm for the nominally 1-μm wide line and 0.34 μm for the nominally 3-μm wide line. Part of these differences

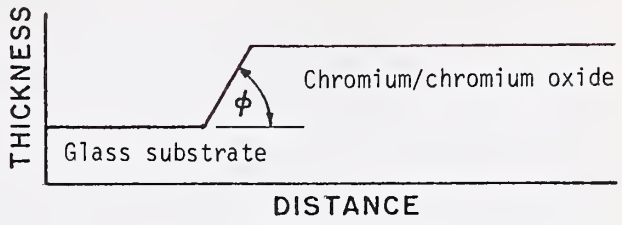

a. Model of line edge.

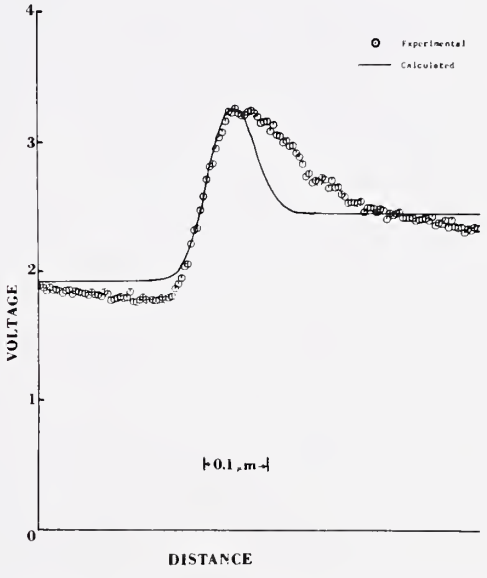

b. Comparison of an experimental SEM line-edge profile with the profile calculated from the model.

Figure 39. Line-edge profile for the model and a comparison of an experimental SEM line-edge trace with the calculated trace based on the model.

is probably due to the measurement uncertainties associated with each measurement system. For the optical microscope, the measurement uncertainty is estimated to be ±0.10 μm. For the SEM/interferometer, the uncertainty is not so well characterized, but is estimated to be smaller than ±0.10 μm. The SEM/interferometer system has the potential for a significantly smaller uncertainty than the optical microscope as a result of the better resolution of the SEM. The relatively large difference of 0.34 μm appears to be an anomaly which is currently under investigation.

(A. W. Hartman[¶], D. Nyyssonen[†], R. E. Swing[¶], and W. J. Keery)

[¶]NBS Optical and Micrometrology Section, Mechanics Division.

[†]NBS Optical Physics Division.

Table 8 — Average Line-Width Measurements As Determined With the Optical Scanning Photometric Microscope and the SEM/Interferometer for a Black-Chromium Artifact

Nominal Line Width	Measured Line-Widths, μm		
	Optical Microscope	SEM/Interferometer	Difference
1 μm Opaque	0.77	0.77	0
1 μm Clear	0.94	1.07	0.13
3 μm Opaque	2.90	2.91	0.01
3 μm Clear	3.12	3.46	0.34

7. TEST PATTERNS

7.1. Test Patterns for Resistivity-Dopant Density Evaluation

The test pattern for developing data for re-evaluation of the resistivity-dopant density relationship in silicon has been redesigned to provide square-array four-probe resistor structures [39] of varying pipe size. Of the various structures for measuring resistivity included on test pattern NBS-3 (NBS Spec. Publ. 400-12, pp. 19-22) [8], the square-array four-probe resistor has proven to be the best. However, because of lateral diffusion and depletion width effects (NBS Spec. Publ. 400-17, pp. 25-26), a single pipe size proved inadequate for making measurements on specimens which covered a resistivity range from less than 10^{-3} Ω·cm to over 100 Ω·cm. The square-array four-probe resistors on the original mask set for test pattern NBS-3 had 0.25-mil (6.3-μm) square pipes. A modified base mask was made which permitted fabrication of 0.50-mil (12.7-μm) square pipes [39]; however, both sizes could not be fabricated on the same wafer. The new test pattern, NBS-4, contains five square-array four-probe resistors with pipe sizes of 0.20, 0.25, 0.30, 0.40, and 0.50 mils (5.1, 6.3, 7.6, 10.2, and 12.7 μm).

In addition two MOS capacitors with diffused guard rings for making steady-state, deep-depletion, capacitance-voltage measurements [40] of dopant density and four new base sheet resistors (see sec. 7.2.) were included on the new pattern. Two new mask levels were added to the original four levels [8]. One of these, the BASE-CONTACT mask, is designed to delineate heavily doped regions for making electrical contact to base diffusions. These regions are generally used only in processing of *p*-type wafers to reduce the resistance of the aluminum contacts to the *n*-type base regions; the aluminum metallization makes satisfactory contact to typical *p*-type base regions. The other mask, the GATE mask, is used to delineate regions of thin, high-quality oxide which are needed for the MOS devices; only one type of oxide can be fabricated with test pattern NBS-3 [8].

A photomicrograph of the NBS-4 test pattern is shown in figure 40. The overall pattern is 200 mils (5.08 mm) on a side and is divided into four quadrants. The new structures on the pattern were designed using the same design rules as for NBS-3 [8]. The 38 test structures on the NBS-4 pattern are listed in table 9. Note that the Hall effect device (4.31) is functional only after it has been scribed from the wafer. The devices specifically designed for the resistivity-dopant density evaluation are indicated by an asterisk in the table. Bulk dopant density values can be obtained from the following structures: the three MOS capacitors (4.2, 4.3, and 4.8), the base-collector diode (4.10), the MOSFETs (4.15 and 4.16), and the Hall effect device (4.31). Bulk resistivity values can be found from the five square-array four-probe collector resistors (4.1, 4.5, 4.7, 4.9, and 4.17) and the Hall effect device (4.31).

A variety of other structures for various purposes was also included on the new test pattern. It contains eight base sheet resistors, four of which were not included on test pattern NBS-3 [8], in order to provide comparisons of the various geometries (see sec. 7.2.). The base-under-emitter sheet resistor (4.20) is a new structure on test pattern NBS-4; it is intended to determine the sheet resistance of the active region of the base. The metal sheet resistor (4.19) is constructed as a Greek cross (NBS Spec. Publ. 400-29, pp. 64-65) [41] rather than as an offset quadrate cross (pinwheel) (NBS Spec. Publ. 400-19, pp. 44-45) to avoid the problem of burn-out due to high current density in narrow connecting arms. The incremental base sheet resistor (4.35) was redesigned with wider contact arms than the equivalent structure (3.30) to reduce problems which arose from the thinning of the contact arms during anodic oxidation and etching.

(W. R. Thurber and M. G. Buehler).

7.2. Sheet Resistor Test Structures

Measurements were made on the base sheet resistors in both *n*- and *p*-type wafers fabricated with test pattern NBS-4 (see sec. 7.1.). There are six van der Pauw and two bridge base sheet resistors on this test pattern. Four of these structures are new and four also were included on test pattern NBS-3 [8]. The four new structures are illustrated in figure 41. The repeated structures are the offset quadrate cross van der Pauw resistor (4.26), the large circular van der Pauw resistor with a field plate and channel stop (4.11), a still larger circular van der Pauw resistor designed for incremental sheet resistance studies (4.35), and a bridge-type sheet resistor with the probe pads in a linear configuration (4.33).

Results of measurements of all eight sheet resistors along the diameter of a 60-Ω·cm *n*-

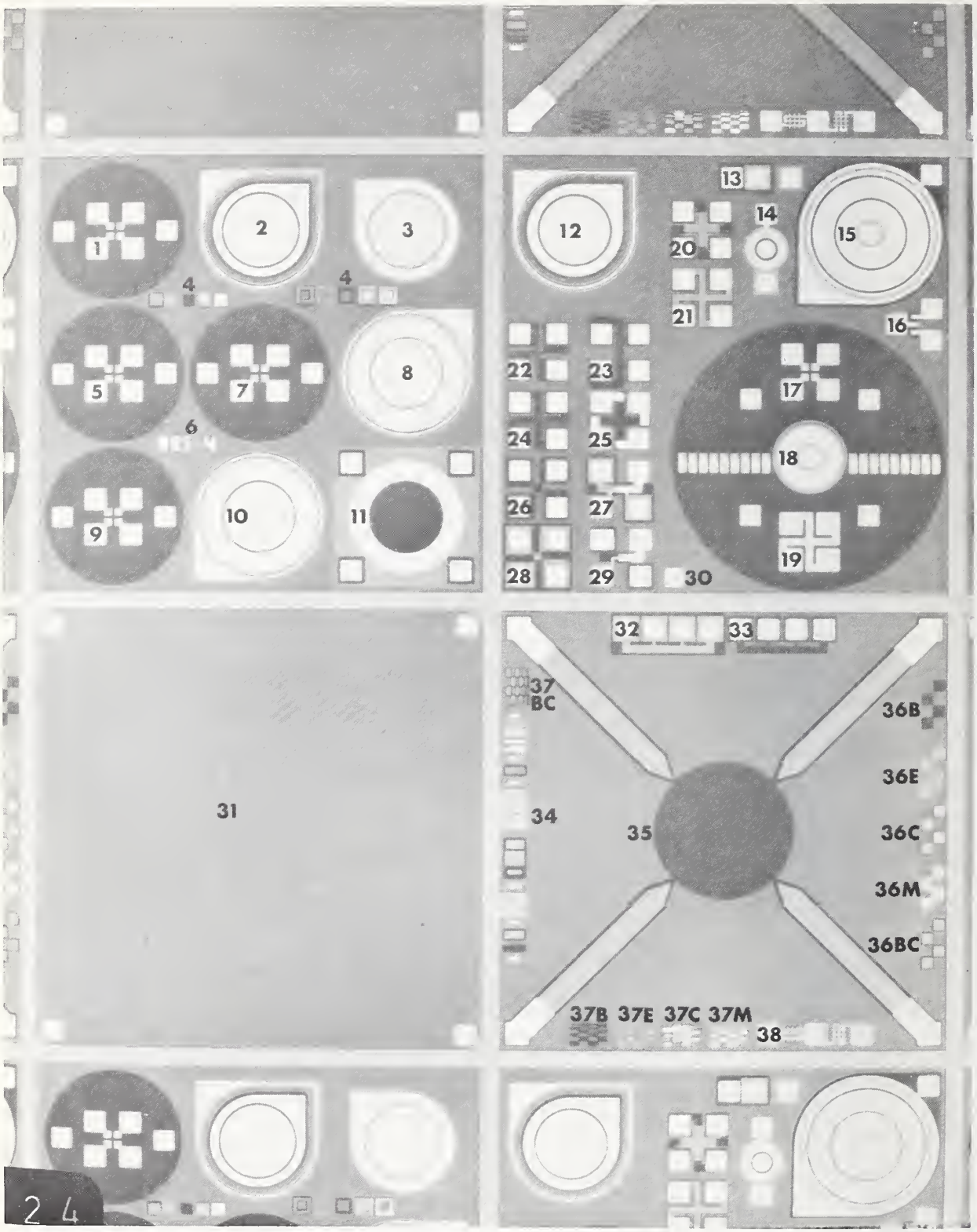

Figure 40. Photomicrograph of test pattern NBS-4 for characterizing the resistivity-dopant density relation in silicon. (The 38 test structures are identified in table 9. The overall pattern is 200 mils (5.08 mm) on a side.)

Table 9 — Planar Test Structures on Test Pattern NBS-4

Number	Test Structure[a]	Important Mask Dimension, mil (mm)[b]
1	*Collector resistor (pipes 0.20 mil on a side)	S = 2.25 (0.057)
2	*MOS capacitor over collector (base DGR)	D = 15 (0.38)
3	*MOS capacitor over collector (emitter DGR)	D = 15 (0.38)
4	Alignment markers	
5	*Collector resistor (pipes 0.30 mil on a side)	S = 2.25 (0.057)
6	Logo	
7	*Collector resistor (pipes 0.40 mil on a side)	S = 2.25 (0.057)
8	*MOS capacitor over collector (FP, CS)	D = 15 (0.38)
9	*Collector resistor (pipes 0.50 mil on a side)	S = 2.25 (0.057)
10	*Base-collector diode (FP, CS)	D = 17 (0.43)
11	Base sheet resistor (VDP, FP, CS)	D = 17 (0.43)
12	MOS capacitor over base	D = 15 (0.38)
13	Bipolar transistor	S = 5.5 (0.14)
14	Base-collector diode (FP, CS)	D = 5 (0.13)
15	MOSFET (circular, W/L = 18.2)	L = 3.5 (0.089)
16	MOSFET (rectangular, W/L = 4)	L = 0.5 (0.013)
17	*Collector resistor (pipes 0.25 mil on a side)	S = 2.25 (0.057)
18	Collector spreading resistor	D = 15 (0.38)
19	Metal sheet resistor (Greek cross)	S = 1.5 (0.038)
20	Base-under-emitter sheet resistor (Greek cross)	S = 1.5 (0.038)
21	Base contact sheet resistor (Greek cross)	S = 1.5 (0.038)
22	Base sheet resistor (Greek cross)	S = 0.25 (0.0064)
23	Base sheet resistor (B, W/L = 0.25)	L = 6 (0.15)
24	Base sheet resistor (Greek cross)	S = 1.5 (0.038)
25	Base sheet resistor (Greek cross, tab contacts)	S = 1.5 (0.038)
26	Base sheet resistor (offset quadrate cross)	S = 1.5 (0.038)
27	Metal-to-emitter contact resistor	S = 1.0 (0.025)
28	Emitter sheet resistor (offset quadrate cross)	S = 1.5 (0.038)
29	Metal-to-base contact resistor	S = 1.0 (0.025)
30	MOS capacitor over collector	S = 4 (0.10)
31	*Hall effect device (VDP)	S = 100 (2.54)
32	Emitter sheet resistor (B, W/L = 0.25)	L = 6 (0.15)
33	Base sheet resistor (B, W/L = 0.25)	L = 6 (0.15)
34	Surface profilometer structure	
35	Incremental base sheet resistor (VDP)	D = 30 (0.76)
36	Etch-control structures[c]	
37	Resolution structures[c]	
38	Metal step-coverage resistor	

* = structures designed for resistivity-dopant density evaluation.

[a] B = bridge; CS = channel stop; DGR = diffused guard ring; FP = field plate; L = length along current path; VDP = van der Pauw; W = width of current path.

[b] D = diameter; L = length along current path; S = side of a square.

[c] B = BASE mask; BS = BASE CONTACT mask; C = CONTACT mask; E = EMITTER mask; GO = GATE OXIDE mask; M = METAL mask.

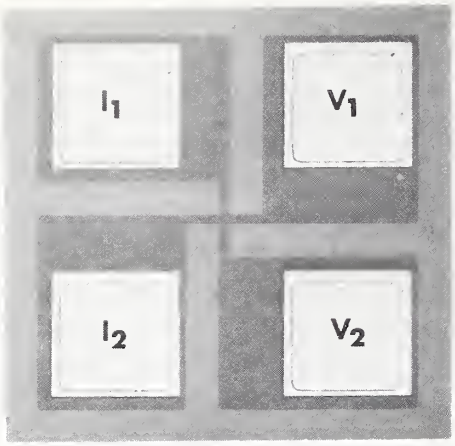

a. Greek cross (4.22).

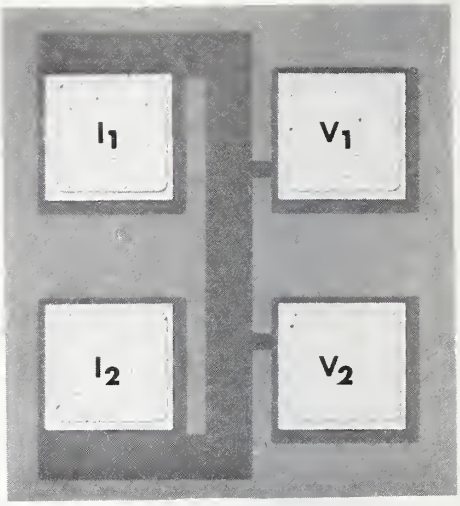

b. Bridge (4.23).

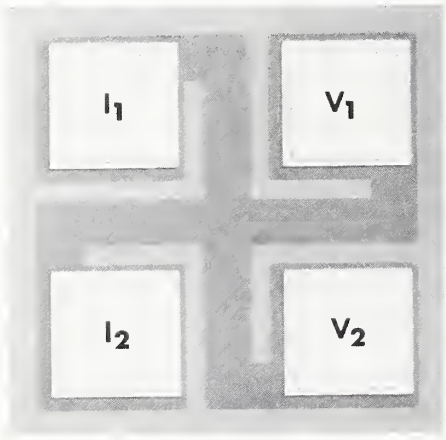

c. Greek cross (4.24).

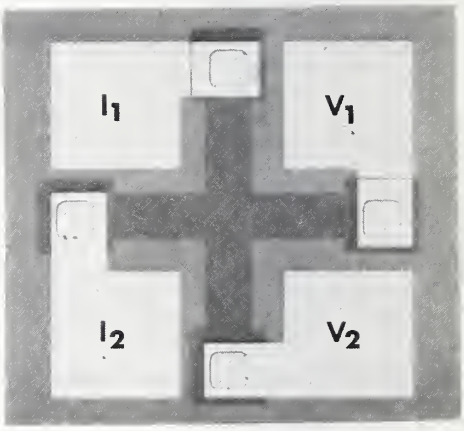

d. Greek cross (4.25).

Figure 41. Four of the base sheet resistors on test pattern NBS-4.

type silicon wafer are shown in figure 42. All the van der Pauw configurations at a given location give essentially the same sheet resistance. Since the large incremental sheet resistor (4.35) is located at a considerable distance from the cluster of other base sheet resistors (see fig. 40), the sheet resistance was measured on devices above and below the quadrant where most of the other sheet resistors are clustered and averaged to obtain the values plotted on figure 42. This procedure reduces the effects of gradients in the sheet resistance on the intercomparison.

The good agreement of the new Greek-cross structures with the circular and offset quadrate cross structure supports the numerical analysis of these configurations by David and Buehler [41]. In particular, they showed that the Greek-cross sheet resistor is a valid van der Pauw test structure if the length of the arms is greater than the width of the arms. Thus, accurate measurements of the sheet resistance of a very small region can be made. Structure 4.22 has arms which are only 0.25 mil (6.4 μm) wide which is the minimum line width on the pattern. Simple calculations of the effects of lateral diffusion on sheet resistance predict that structure 4.22 could show a resistance up to 6 percent higher than the structures with 1.5-mil (38.1-μm) wide arms such as structures 4.24 and 4.25. However, the experimental data suggest that any such effect, if present at all, is at most about 0.5 percent.

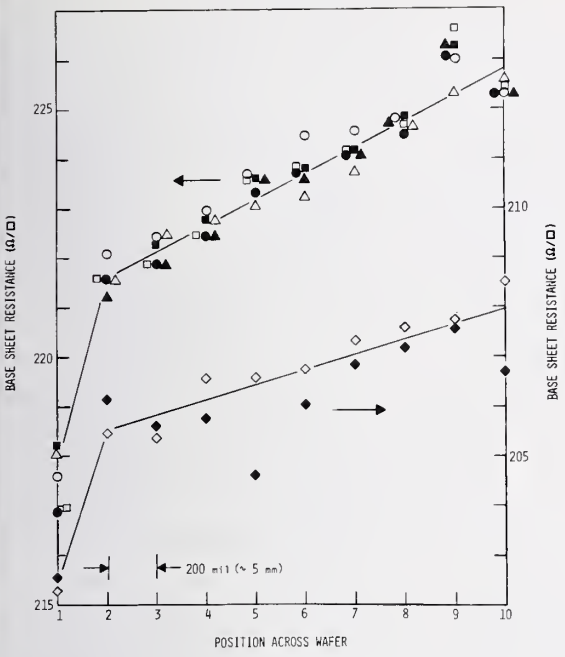

Figure 42. Base sheet resistance across diameter of Wafer B59Ph-1 (60-Ω•cm n-type) fabricated with test pattern NBS-4. (▲: Circular van der Pauw with field plate and channel stop (4.11); ○: Greek cross (4.22); ◆: Bridge (4.23); ●: Greek cross (4.24); ■: Greek cross (4.25); □: Offset quadrate cross (4.26); ◇: Bridge (4.33); △: Large circular van der Pauw (4.35).)

As expected, the bridge structures show lower sheet resistance values than the van der Pauw structures because of the effects of overetching and lateral diffusion on the bridge structures (NBS Spec. Publ. 400-17, pp. 22-24). It is interesting to note that the two lines in figure 42, through the van der Pauw and through the bridge data points, are not parallel. This means that the amount of overetching varied across the wafer.

The results of measurements on two p-type silicon wafers revealed problems due to the presence of an inverted surface layer which shunts the current in the van der Pauw structures. Measurements on a 3-Ω•cm p-type wafer yielded results similar to those obtained on the n-type wafer discussed above. As shown in figure 43, the base sheet resistance had a steep U-shaped profile, but, within the uncertainty due to the large variation in sheet resistance across the wafer, the van der Pauw structures all gave about the same value at a given location. The two bridge structures had lower measured sheet resistance which could be generally accounted for by overetching and lateral diffusion effects. These two structures had about the same sheet resistance at the center of the wafer; one is higher to the left of center and the other higher to the right of center, as would be expected from their positions on the test pattern.

The results of measurements on a 92-Ω•cm p-type wafer, which was processed at the same time as the 3-Ω•cm wafer except that following the emitter diffusion all oxide was removed and a new, thinner oxide was regrown to reduce surface inversion caused by charge in the oxide, were significantly different as shown in figure 44. On this wafer, the sheet resistance as measured on some of the van der Pauw structures was much higher than the nominal 200 to 300 Ω/□, and the sheet resistance of the bridge structures was much lower than would be predicted by overetching considerations. The results on both kinds of structures can be qualitatively explained by the presence of an inverted surface layer on the p-type collector region which occurred in spite of the special oxidation procedure. For the van der Pauw structures, some of the current passes through this surface layer which surrounds the body of the resistor; this results in a higher than normal value of measured sheet resistance. The fraction of the current which passes through the surface layer is strongly dependent on the geometry of the structure; the arm resistance and the spacing between arms are important factors. Structure 4.22, which has narrow arms close together, shows the highest sheet resistance. Structure 4.11 which has a channel stop and field plate appears to give the truest value of sheet resistance. The basic design of this structure is good because the arms, even though they are fairly narrow, are widely separated from each other. Consequently, even when the plate was biased to accumulate the collector surface surrounding the base diffusion, the measured sheet resistance was not changed significantly from the value measured with an inverted surface. That structure 4.25 is much less influenced by the surface layer than structure 4.24 can be attributed to the fact that the diffusion for structure 4.24 extends under the probe pads and consequently the amount of shunted current is much greater than that for structure (4.25). For the bridge structures, the inverted surface layer provides a parallel current path which reduces the measured sheet resistance. (W. R. Thurber, M. G. Buehler, and Y. M. Liu)

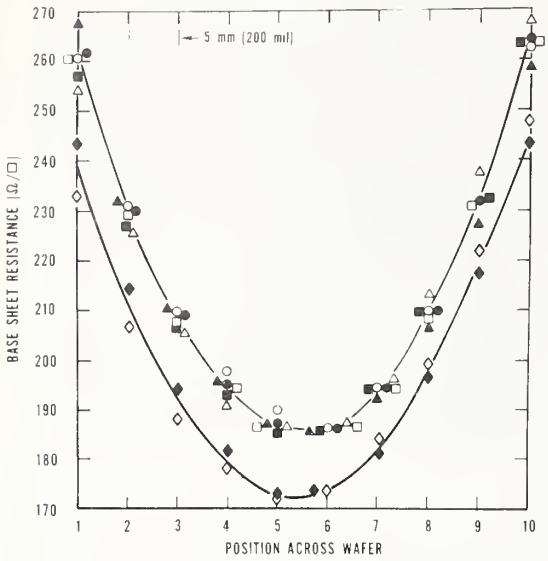

Figure 43. Base sheet resistance across diameter of Wafer B3.0B-3 (3-Ω•cm p-type) fabricated with test pattern NBS-4. (Symbols are the same as in fig. 42.)

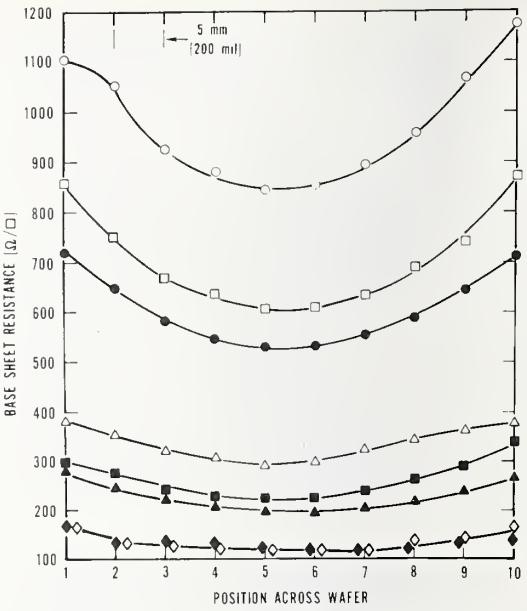

Figure 44. Base sheet resistance values for Wafer B92B-2 (92-Ω•cm p-type) fabricated with test pattern NBS-4. (Symbols are the same as in fig. 42.)

7.3. Overetch Structure for Visual Measurement

An important parameter to be measured in integrated circuit processing is the amount of overetching which has occurred whenever a pattern is delineated by etching selected areas such as the windows in the silicon dioxide layer prior to a diffusion or when patterning the metallization interconnect layer. A test structure was designed to provide a rapid way to estimate the amount of overetching from microscopical observations. This structure contains a built-in distance scale which allows one to calculate the amount of overetching without knowing the magnification of the microscope that was used to observe the structure on the wafer. However, because the scale is a line-spacing scale and the determination of the amount of overetching is a line-width measurement (see sec. 6.1.), systematic errors may be introduced; these errors are the order of 0.25 to 0.5 μm [34].

The test structure consists of six 25-μm by 25-μm squares arranged as shown in figure 45a, which illustrates the pattern as it would appear on the photomask. For a metallization pattern, the numbered squares represent areas which will remain unetched, while for oxide windows they are the areas in which etching will occur. In the photomask pattern, the squares are positioned such that the corners of adjacent squares touch each other.

The appearance of the structure after etching a metallization layer is shown in figure 45b, while figure 45c shows the structure as it would appear following the etching of an oxide layer. The effect of overetching (somewhat exaggerated in these figures) is the shrinking of each square in the metallization pattern and the swelling of each square in the oxide pattern. Each side of the square is displaced by one half the amount of the overetching, X_{oe}.

Although etching causes the size of each square to change from the value it had on the photomask, certain distances which are conserved may be used as a convenient scale. It can be seen by comparing the patterns in figure 45 that the distance from any top, bottom, right, or left edge of one square to the corresponding top, bottom, right, or left edge of any other square is conserved in the etching process. For rough determinations, the measurements may be made on a photomicrograph of the structure and the amount of overetching computed from

$$X_{oe} = \frac{W_{oe}}{W_e} X_e ,$$

where X_e is the scale distance on the mask

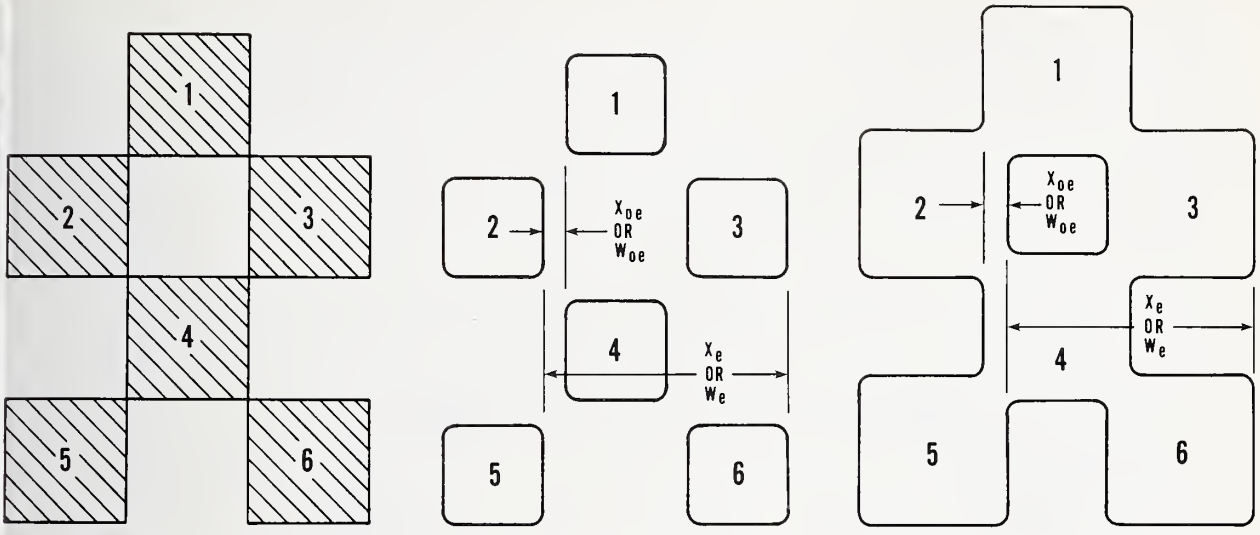

a. Overetch structure, composed of 25-μm by 25-μm squares, as it appears on the photomask. The numbered squares represent areas which remain unetched in a metallization layer and areas which are etched in an oxide layer.

b. Overetch structure after being etched in a metallization layer. The effect of overetching is shown by the shrinking of each square by $X_{oe}/2$ on each side.

c. Appearance of the overetch structure after being etched in an oxide layer. The effect of overetching is shown by the swelling of each square by $X_{oe}/2$ on each side.

Figure 45. Test structure for etch control. (The dimensions X_{oe} and X_e are the actual overetch and "ruler" lengths, while W_{oe} and W_e denote these quantities as they appear on an enlarged photomicrograph of the structure.)

pattern in micrometers, W_e is the scale distance on the photomicrograph in arbitrary units, and W_{oe} is the overetch distance on the photomicrograph in the same arbitrary units. For purposes of illustration in figure 45, the scale chosen is the distance between the line drawn to connect the right edges of squares 2 and 5 and the line drawn to connect the right edges of squares 3 and 6.

For measurements on photomicrographs, additional sources of error include variations in the locations of the edges on the photomicrograph due to aberrations in the camera optical system and to variations in exposure and development of the film. For these measurements it may be sufficient to assume that the scale length, X_e, has the value intended by the photomask design.

For more accurate determinations a line-width measuring system (such as a microscope equipped with a filar or image-shearing eyepiece or an automatic TV-microscope system) calibrated with a line-width standard should be used to make measurements of X_{oe} directly on the pattern. In this case, it is not necessary to use the built-in-scale feature of the pattern. (G. C. Taylor and M. G. Buehler)

7.4. Test Pattern Design Concepts

Layout of test patterns in modular cells (NBS Spec. Publ. 400-25, pp. 41-43) has proven to be useful in structure design (see sec. 7.2.), mask generation (see sec. 7.6.), and testing. A comprehensive test pattern for junction-isolated TTL technology has been designed (NBS Spec. Publ. 400-29, pp. 65-66) [42] using modular cells with a 2 by 10 pad array.

Frequently, however, it is desirable to insert a test pattern die at selected points on a product wafer. In such circumstances, testing is facilitated if the contact pad arrange-

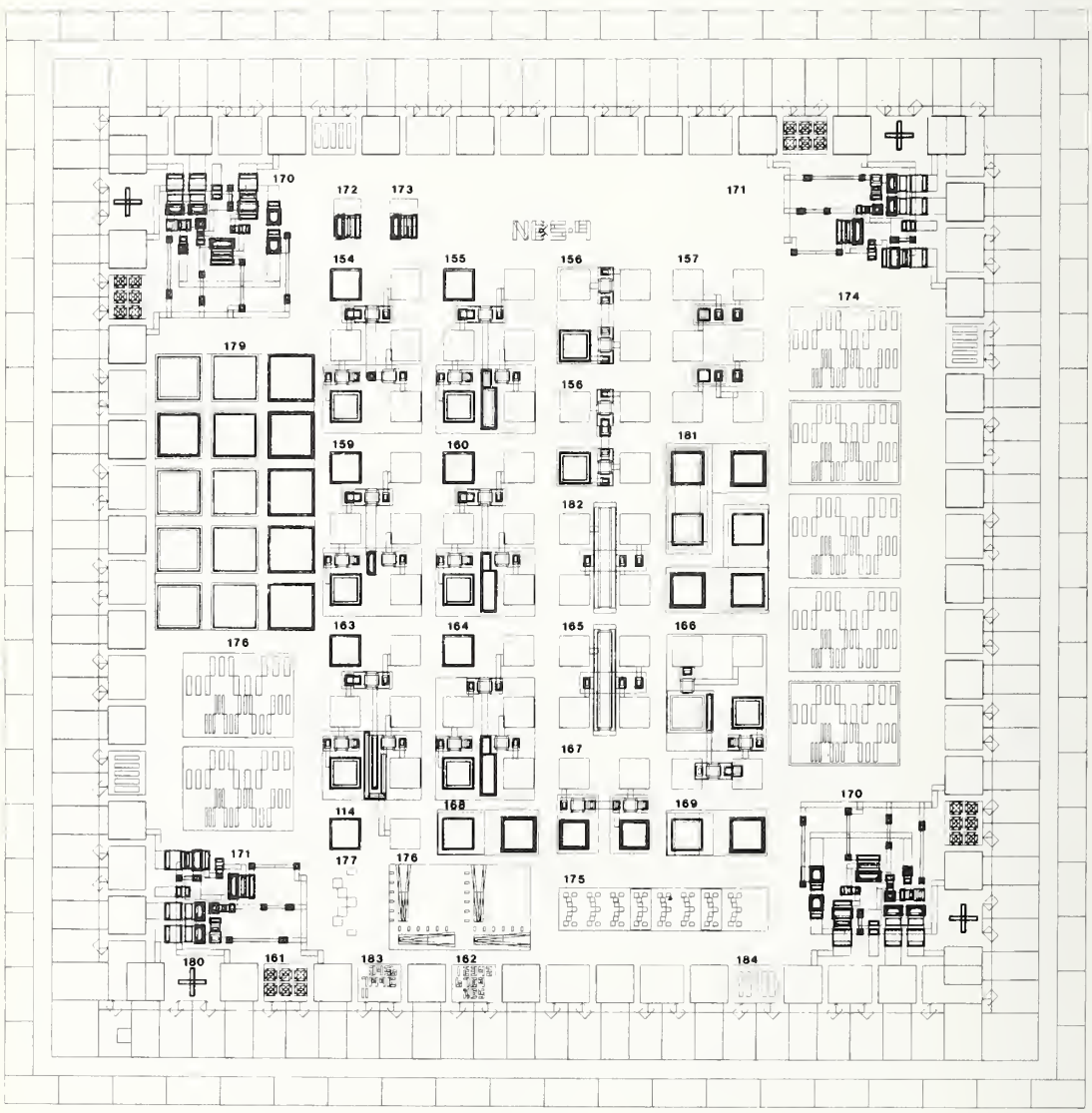

Figure 46. Computer layouts of two quadrants of test pattern NBS-9 for dielectrically isolated periphery of the die.

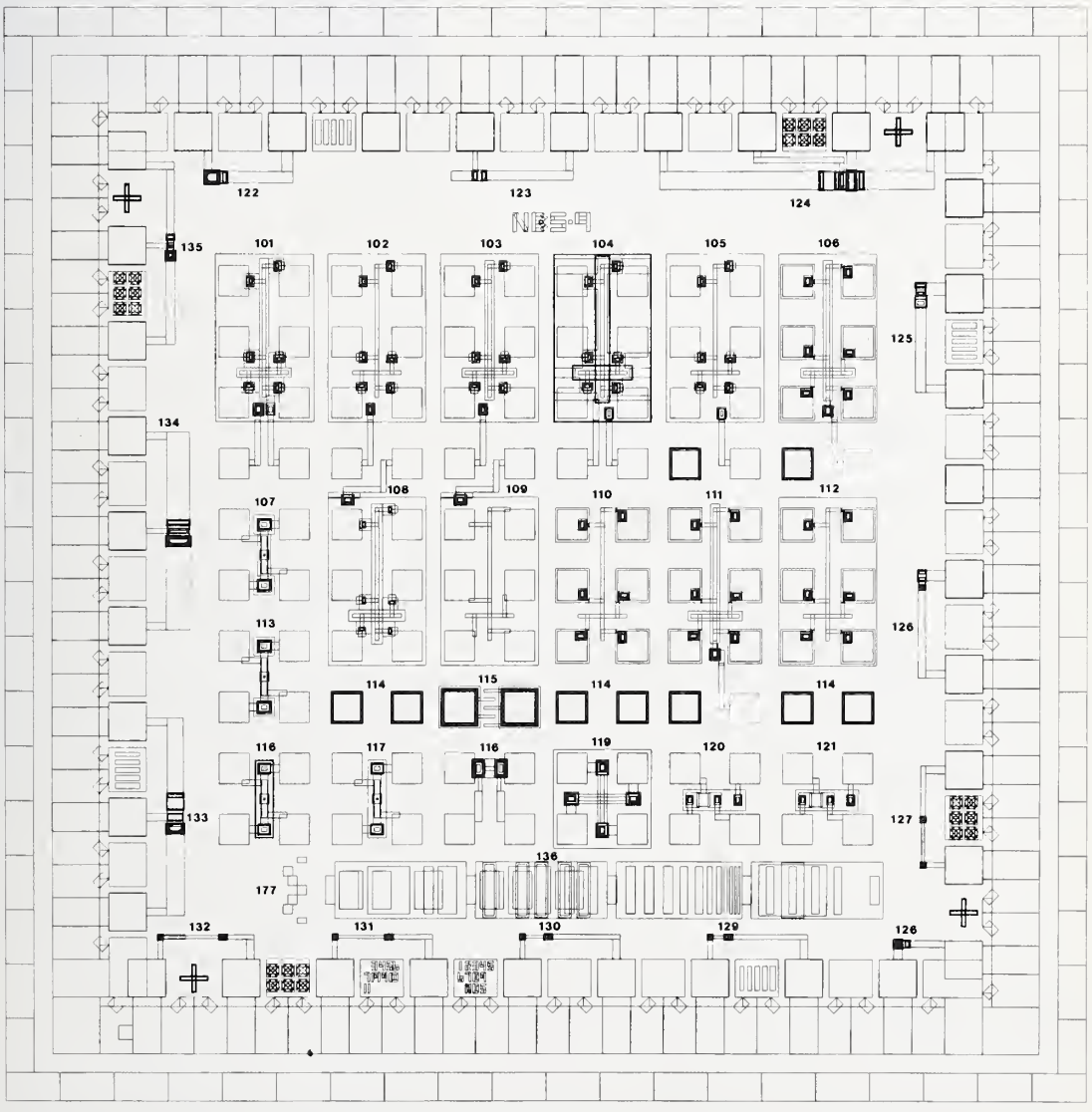

TTL technology showing test structures arrayed in both the 2 by 10 modular array and around the

ment is the same as that on the product die itself. It is possible to combine this arrangement with the 2 by N modular layout of test structures.

As an illustration consider the two quadrants of test pattern NBS-9 which are illustrated in figure 46. This test pattern was designed for a dielectrically isolated TTL integrated circuit (IC) process. The quadrants illustrated contain process control structures for measuring sheet and contact resistances of various diffused layers and metallizations and advanced test structures (NBS Spec. Publ. 400-36, pp. 46-48) for measuring very small device leakage currents arranged in a 2 by 10 array. Around the periphery, connected to the IC contacts, are located selected circuit elements and individual circuit devices.

Testing of the circuit elements can be accomplished by suitable software control flagged by the results of the initial test of the entire IC as determined on the test pattern die. Failure of any of the circuit elements to operate according to designed specifications could trigger tests of the individual circuit devices. Additional tests on the remaining test structures (using a different probe card) might also be necessary to identify the process step at fault.

The complete pattern also contains a number of test structures intended to provide information from visual (microscopical) observation and, in the remaining two quadrants, random fault test structures designed to test for oxide pinholes, metal bridges, metal step coverage, metal step to resistor, number of emitter openings without fault, and perimeter or area emitter faults. (T. J. Russell, G. C. Taylor, D. A. Maxwell, and M. G. Buehler)

7.5. Probe Pad Evaluation

Studies were undertaken to define the limits of probe pad size suitable for use with test patterns arranged in 2 by 10 cell arrays. A single-level test pattern, a cell of which is shown in figure 47, was designed for these studies. Each cell of the pattern contains four 2 by 10 arrays of probe pads shorted together. The four arrays have pads which are either 100, 80, 60, or 40 μm on a side depending on the array. Each cell also contains structures for electrically determining the metal sheet resistance and metal overetch and an array with hollow pads designed to test the centering of the probe pins in the

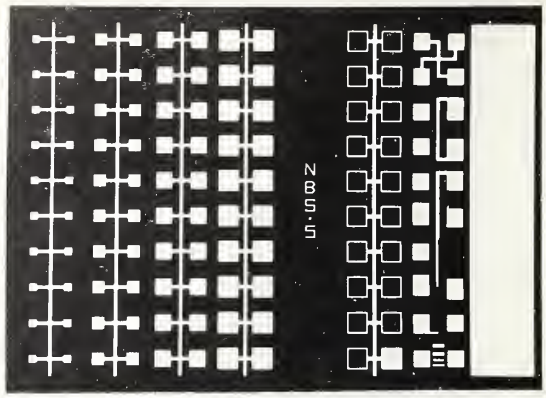

Figure 47. Photomicrograph of test pattern NBS-5 for probe pad and probe card evaluation. (The pads in the leftmost column are 40 μm on a side.)

pad pattern. There is also an all-metal area which is intended to be used for visual inspection of the pattern of the probe marks. The experiments were carried out on patterns etched in aluminum deposited on an oxidized silicon wafer.

Three probe cards, each from a different vendor, were used in the experiments. Each card was used to probe a portion of the pattern which contained 20 rows by 12 columns of cells. Within this sampling area, continuity was checked between the 2400 pairs of adjacent pads in each of the four arrays. A separate patterned wafer was used for tests on each of the probe cards. In each case, the first run was made on the 100-μm square pads with succeeding runs made on successively smaller pads. In each case the probes were aligned under a microscope so that the vertical and horizontal displacements of the probes from the centers of the pads in the probe pad arrays in each of the four corners of the sampling area were, on the average, minimized. Probing proceeded from left to right and from top to bottom of the sampling area.

For each of the three probe cards, the 100-, 80-, and 60-μm probe pad arrays were all probed without a single failure over all 2400 probe pad pairs. This indicated that pads as small as 60 μm on a side can be probed using automatic probing equipment and that probe cards satisfactory for probing pads of this size are generally available from vendors.

In one instance it was possible to probe the 40-μm square pad arrays within the sampling area without a single failure. In the other

0 0 0 0 0 0 0 0 0 0 0 0	1 0 0 0 0 0 0 0 0 0 0 0
0 0 0 0 0 0 0 0 0 0 0 0	0 0 0 0 0 0 0 0 0 0 0 0
0 0 0 0 0 0 0 0 0 0 0 0	0 0 0 0 0 0 0 0 0 0 0 0
0 0 0 0 0 0 0 0 0 0 0 0	0 0 0 0 0 0 0 0 0 0 0 0
0 0 1 0 0 3 6 3 3 3 4 4	0 0 0 0 0 0 0 0 0 0 0 1
3 4 5 2 2 3 4 4 3 5 5 5	0 0 0 0 0 0 0 0 1 1 0 1
3 4 5 3 2 3 5 4 3 3 5 4	0 0 0 0 0 0 1 1 1 1 1 1
3 3 5 3 2 3 5 4 3 3 5 5	0 0 0 1 1 1 1 1 1 1 1 1
3 4 4 3 2 2 5 3 2 3 5 3	0 1 1 1 1 1 1 1 1 1 1 1
2 3 5 3 2 3 5 4 2 4 5 3	1 1 1 1 1 1 1 1 1 1 1 1
3 4 5 2 2 3 4 4 2 2 4 3	1 1 1 1 1 1 1 1 1 1 1 1
2 3 4 3 2 2 4 4 2 2 4 3	1 1 1 1 1 1 1 1 1 1 1 1
2 4 3 2 2 2 4 3 2 2 4 4	1 1 1 1 1 1 1 1 1 1 1 1
2 3 4 2 2 2 5 3 2 2 3 3	1 1 1 1 1 1 1 1 1 1 1 2
2 2 4 2 2 2 4 3 2 2 4 2	1 1 1 1 1 1 1 2 2 2 2 2
2 3 4 8 8 8 9 8 7 8 X 8	1 1 1 1 2 2 2 2 2 2 3 3
8 8 X 8 7 8 X 8 8 8 X 8	1 1 1 2 2 2 2 2 2 2 3 3
8 8 X 8 8 8 X 8 8 8 X 9	1 1 1 2 2 2 2 2 2 2 2 3
8 9 X 8 8 7 X 8 8 8 X X	1 1 2 2 2 2 2 2 2 3 3 3
7 8 X 8 8 8 X 8 8 8 X 8	1 1 2 2 2 2 2 3 3 3 3 3
a. Probe card A.	b. Probe card B.

Figure 48. Number of failures per cell as a function of relative position when probing 40-μm probe pads using different probe cards.

two cases the fault patterns appear to indicate the occasional occurrence of minor mechanical problems in the probing equipment used in the experiment. Figure 48 shows the number of probe pad pairs at which continuity was not detected as a function of position within the sampling area in these two experiments. The letter X indicates that all ten probe pad pairs were open within that cell.

In one case, shown in figure 48a, probing was successful (with one exception) until the sixth site in the fifth row of the sampling area. From that point on probe pad pairs 3 and 7 (where the top pair in each 2 by 10 array is pair 1) failed in nearly every cell, and pad pairs 2, 4, 6, and 8 failed occasionally, to give a total of from 2 to 6 failures within each cell. This behavior continued until the fourth site in the sixteenth row. At that point other pad pairs began to fail also so that between 7 and 10 pairs failed in each cell. Such quantum jumps in the number of failures per cell suggest that the prober stepping motor lost or gained one or more steps before stopping at the sites where the quantum jumps occurred. Visual inspection of the probe marks at and near these two sites showed that there was an abrupt change in the positions of the probe marks relative to the probe pad array at these two sites.

In the second case, shown in figure 48b, no quantum jumps appear, but there is a gradual increase in failure rate in moving from one corner of the sampling area to another. It has been speculated that this could be caused by wafer slippage on the chuck or rotation of the chuck as the test proceeded.

The test pattern can also be used to evaluate the suitability of probe cards for probing patterns with the 2 by 10 pad cell array. Measurements with malfunctioning probe cards would yield a regular pattern of open pairs which is easily distinguishable from the patterns observed above.

(R. L. Mattis and M. R. Doggett)

7.6. Computer Aided Design and Layout of Test Pattern Photomasks

A software package, designated Computer Aided Photomask Programs (CAPP), was developed to provide a means of transforming test structure designs into working photomasks. The program architecture is based on a modular concept. The building-block levels are illustrated in figure 49. The basic element is a rectangle which can be any size from a square 0.002 in. (51 μm) on a side to a square 0.060 in. (1.52 mm) on a side. Rectangles can be rotated between 0 and 89.9 deg. A structure is composed of either a single rectangle or a combination of rectangles. Structures are combined to form modular cells which can, in turn, be combined into complete test patterns.

The flow chart in figure 50 indicates the steps required to transform structure designs to a working mask set. After design in accordance with established design rules, the test structures selected for inclusion in a pattern are digitized. In this phase, the hand-drawn rectangles which constitute a structure are reduced to digital form and stored in a computer file. Each structure requires one or more mask levels; each mask level of the structure is stored along with a label indicating both structure and mask level information. This step is carried out on an independent digitizing board.

The results of the digitization are processed using CAPP to create a library index file with entries for each structure and mask lev-

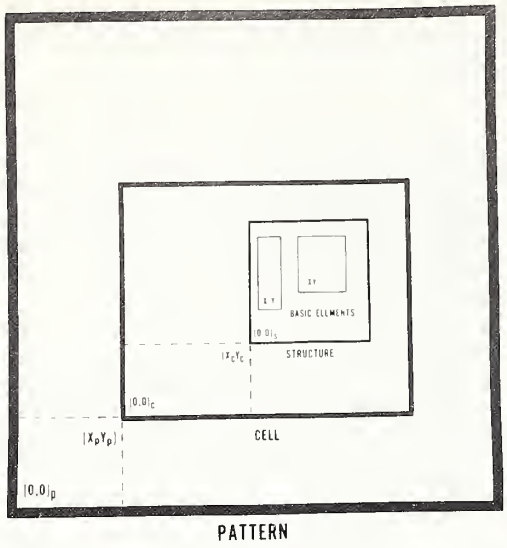

Figure 49. Modular structure concept for photomask design.

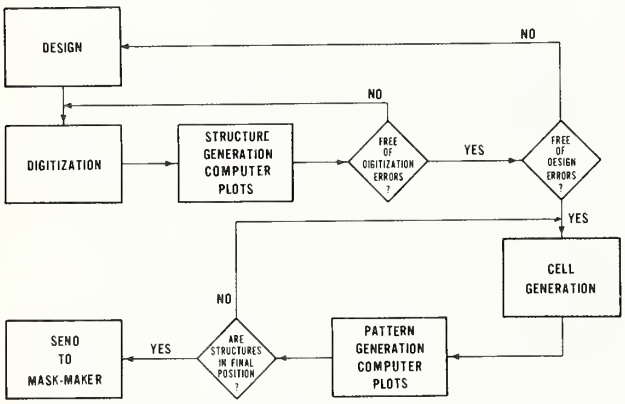

Figure 50. Flow chart indicating steps required to take a structure design to a working mask set.

el combination. To do this, the input data base, which is read in freefield format, is written into a random access file with fixed record length. At the same time, a second file, the library file, keeps track of the structure number, mask level, and record position in the random access file. The library file can then be used to interrogate the random access file, record by record, and create computer-generated plots of each structure-mask level. These plots are used to verify the design and check for digitization errors.

To reduce the data handling in the final pattern, cells, which consist of a group of structures, are constructed with the use of CAPP. The location of each structure within the cell is determined by specifying the coordinates of the lower left corner of the structure. It is possible, therefore, that more than one structure may occupy the same location or the same structure may occupy different locations in the cell with the restriction that each structure assignment uses one of the 10 structure positions. Although the cell is multi-leveled, it is not necessary that the cell level and the structure level be the same; since each structure level is a basic unit, it may be included in any cell level. For example, a new structure could be formed by using a structure emitter level as a cell base level when the cell is generated. At completion of this phase, the cell is the new basic unit. Each cell level contains the collection of structure-level data for all structures contained in the cell. There is no restriction on the shape of the cell; however, modular design with a 2 by 10 array of contact pads (NBS Spec. Publ. 400-25, pp. 41-43) is encouraged in order to maximize the pattern density and reduce parasitic effects due to design differences (c.f. sec. 7.2.).

Next the cells are positioned into the pattern by specifying the coordinates of the lower left corner of each cell. At this stage additional computer-generated plots may be obtained and checked to ensure that the pattern layout is complete and correct.

Finally, a file which contains all rectangle information for each level used in the pattern is written. This file is then reformatted and written on magnetic tape for use as the input source of the mask-making machine.

(R. C. Frisch and D. A. Maxwell)

7.7. Advanced Planar Silicon Test Structures

Design of the test pattern for studying the limits and application of advanced test structures containing integral electrometer amplifiers (NBS Spec. Publ. 400-36, pp. 46-48) was completed. The pattern consists of both advanced gated diode and capacitor test structures and conventional test structures.

The advanced test structures are arranged modularly with a 2 by 10 contact pad array. The center-to-center pad spacing is 160 μm and the standard pads are squares 4 mils (100 μm) on a side. The test structures are spatially interchangeable within the module and common bus lines are utilized to eliminate redundant pads. With the common bus approach,

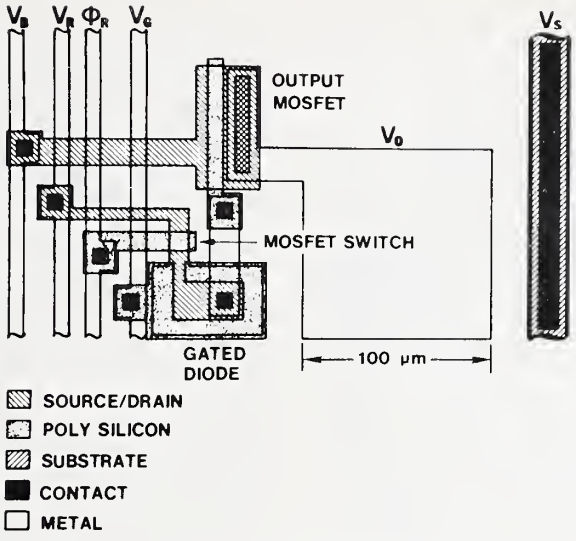

Figure 51. Advanced test structure, showing common bus lines and gated diode with integral reset transistor and MOSFET electrometer.

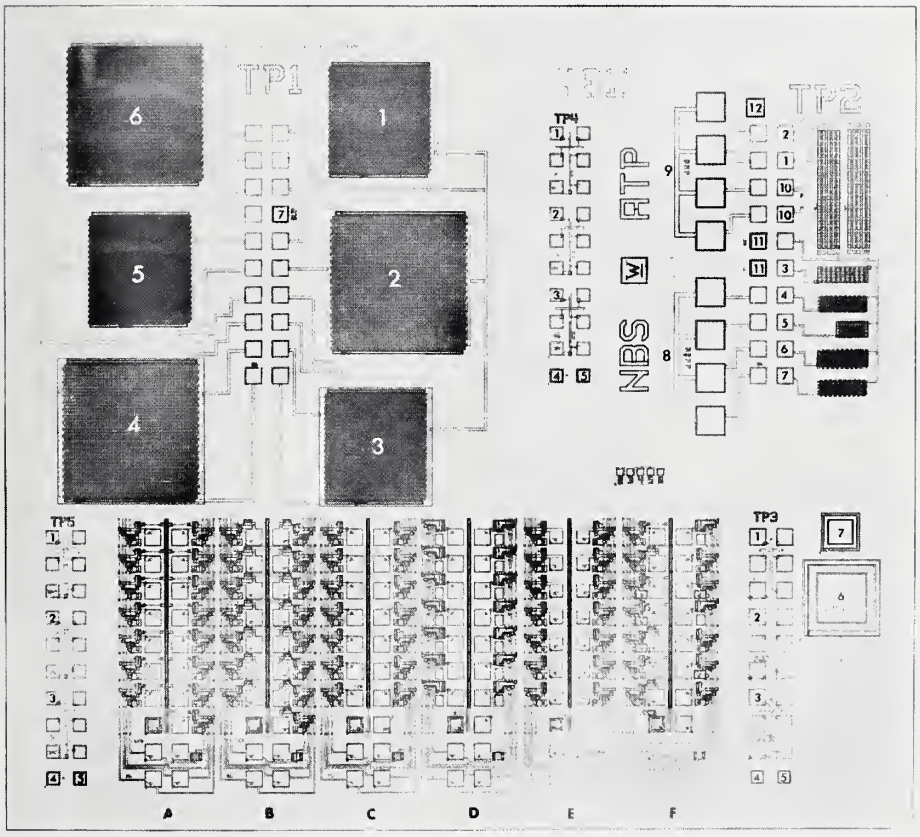

Figure 52. Computer layout of test pattern for evaluation of advanced test structures.

each 20-pad module contains 14 to 16 test circuits and measures approximately 20 mils (0.5 mm) by 62 mils (1.57 mm).

To illustrate the modularity concept of the advanced test structure array, a circuit featuring all the connections necessary to construct a 2 by N test module is shown in figure 51. Four pads located on the bottom of the module supply all the signals necessary to operate any of the capacitor or gated diode test structures through the four bus lines marked V_B, V_R, ϕ_R, and V_G. The innermost of the four vertical lines (V_G) is connected to the gates of all the diodes in the module. Although this line is not connected to capacitor structures, it runs the length of the module to allow contact to be made to diode circuits located above the capacitor structures. The second vertical line (ϕ_R) is connected to the gates of all the reset transistors located in the module. The third line (V_R) is a supply bus for the drain of the reset transistor switch. The outermost line (V_B) is a supply bus for the drain of the electrometer. A fifth common pad is connected to a long vertical contact stripe (V_S) which runs the length of the module and assures a uniform ground contact for all circuits regardless of their location. The pad (V_O) is a typical circuit output pad. The circuit shown in the figure is that of the standard gated diode structure. The module layout incorporates built-in crossunders and allows for all bus lines to run uninterrupted through the length of the module. With the use of this design approach, the construction of any 2 by N test module requires only one output pad per test structure, plus the five common bus pads described above.

The complete pattern, designated NBS/Ⓦ ATP, is shown in figure 52. The overall die (chip) size is 197 mils (5.00 mm) by 217 mils (5.51 mm). There are six advanced test structure modules, labeled A through F, located on the bottom of the test pattern. Module A contains 15 diode circuits each featuring an on-chip 1-kΩ load resistor. The post-processing value of the resistance of this resistor can be obtained directly by measuring the resistance between the circuit output and substrate pads. Module B consists of 15 diode circuits each featuring an on-chip load transistor. The size of this active load device is identical to that of the output electrometer. Complete access to the source, gate, and drain of this device is available via the output and substrate pads. Module C contains 14 diode circuits, each requiring an external load resistor. One of the 14 circuits also allows direct access to the diode diffusion and electrometer gate. Module D consists of 14 capacitor circuits, each requiring an external load resistor for circuit operation. As with diode module C, one of the 14 circuits allows direct access to the capacitor and electrometer gate. Module E is identical to module C with the exception that the probe pads are 3.2 mils (80 μm) square instead of the standard 4-mil (100-μm) square pads found on all other modules. Module F is a composite module which includes all the circuits found in modules A through D. In addition, three new versions of the diode circuit were added which are not found in any other module. These circuits are similar to the three diode circuits in modules A, B, and C except that the diode area was greatly increased to provide a means for studying the effect of diode area on the circuit characteristics.

The conventional test structures are grouped into five modules, labeled TP1 through TP5 in figure 52. Module TP1 contains six polysilicon-metal resolution patterns and pinhole testers. Module TP2 contains two contact strings, five step-continuity testers, two bridge resistors, and two substrate contact windows. Module TP3 contains three cross-bridge resistors (NBS Spec. Publ. 400-36, pp. 45-46) and two capacitors for conventional capacitance-voltage measurements. Modules TP4 and TP5 each contain three cross-bridge resistors; various sizes of lines and contact arms are utilized in the nine cross-bridge structures in order to permit study of the effects of size on results obtained with this structure.

(D. McCarthy*, B. Godwin*, M. L. Lonky*, D. S. Herman*, J. Victorey*, and J. Acevedo*)

7.8. Test Pattern Design and Analysis for SOS/LSI

This task was undertaken to develop a comprehensive test pattern for characterizing and monitoring a large scale integration (LSI), silicon-on-sapphire (SOS) process and other mask-compatible processes (NBS Spec. Publ. 400-25, pp. 44-45). During this final period of experimental work, the software for test-

*Work performed at Westinghouse Defense and Electronic Systems Center under NBS Contract No. 6-35766. NBS contact for additional information: M. G. Buehler.

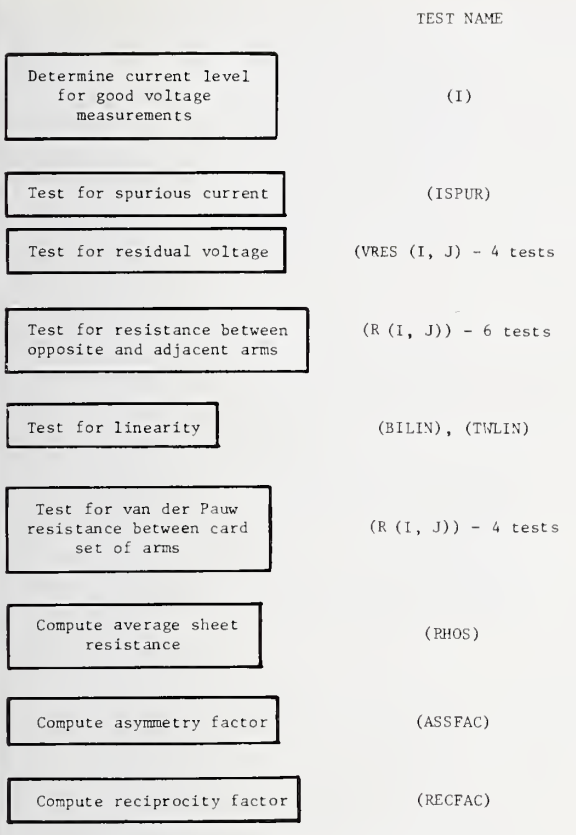

Figure 53. Complete test sequence for ungated van der Pauw test structure.

ing the automatically testable structures in quadrants 1, 2, and 4 of the pattern was generated and used.

All the software necessary for creating and using the test programs has been completed so that any collection of the structures contained in the pattern may be tested with only very small programming effort. It is only necessary to know the key parameters indicating the tests desired to obtain a working version of a test program. These include the pin connections and the desired limits for the tests. The user does not have to be familiar with the details of the testing hardware or the test programming syntax to obtain a working program. An extensive report on this work is being prepared.

The following relatively complete example of the testing cycle through preliminary data reduction serves to illustrate the use of the programming concepts. Since it is reasonably straightforward and concise, the procedure for testing the ungated van der Pauw

Table 10 — Initial Parameters and Contact Pad Identification for Testing Ungated van der Pauw (Cross) Sheet Resistors

A. Initial Parameters	
Specified applied voltage	(VAPP)
Minimum tolerable test current	(IMIN)
Maximum tolerable test current	(IMAX)
Maximum tolerable spurious current	(ISPURM)
Maximum acceptable residual voltage with no current	(VIϕ)
Maximum acceptable resistance between arms	(RAMX)

B. Contact Pad Identification		
Location	Number	Symbol
Upper left pad	1	PUL
Lower left pad	2	PLL
Upper right pad	3	PUR
Lower right pad	4	PLR
Isolated pad	5	PXX

(cross) sheet resistor structures (see sec. 7.2.) in quadrant 1 is described.

The heart of the entire procedure is the test block. Each structure has several types of test blocks which may be suitable for the particular application of interest. The test block for the ungated van der Pauw structure of quadrant 1 is mnemonically named UVDP1. The block diagram of the complete test sequence, which is appropriate for use when the sheet resistance of the material is unknown, is shown in figure 53. Other test blocks for this structure, which are less complete, may be used if less information is desired.

In performing the test, the parameters listed in table 10 are specified together with the appropriate pin numbers used in contacting the structure. The actual tests performed by the tester are shown in the block diagram of figure 54. The current to be used for the tests is first determined by applying the specified voltage (VAPP) to each set of arms and measuring the resulting current. If an average current between (IMIN) and (IMAX) cannot be supplied by the tester, then testing is halted and the next structure is started. Since the digital voltmeter employed has a resolution and accuracy of 100 μV, the sensed voltage must be at least 100 mV in order to achieve 0.1-percent accuracy. This requires an applied voltage of 10 V.

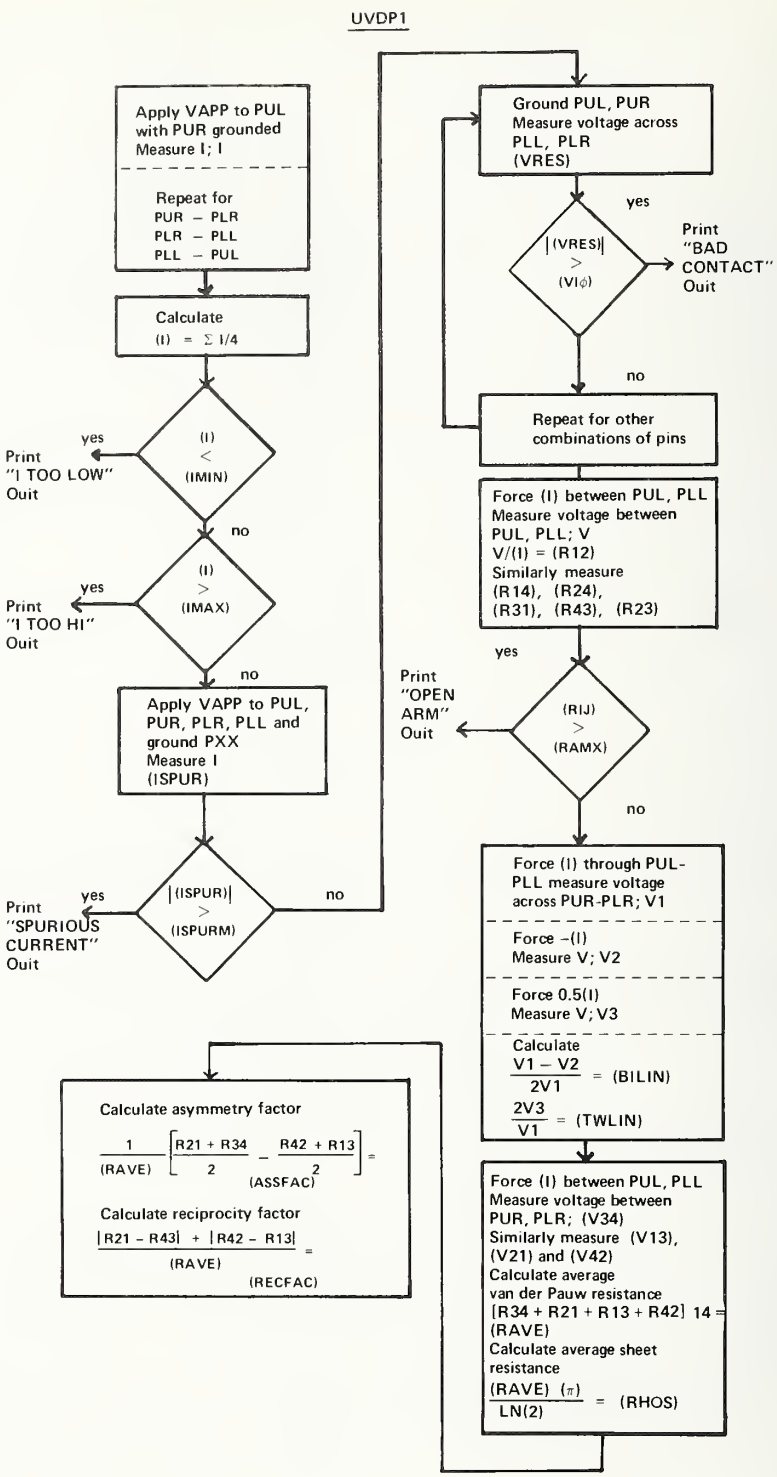

Figure 54. Flow chart for complete UVDP1 test sequence.

The structure is tested next for spurious current. Such currents are generally relatively small for SOS structures, but can be very significant for bulk silicon structures. In this test VAPP is applied to the four pads of the structure (PUL, PLL, PUR, and PLR) and a fifth, nominally isolated, pad (PXX) is grounded. The current between the structure and the nominally isolated pad is measured; if this spurious current exceeds a specified value (ISPURM), testing is halted.

Next, a test is done to ensure that the resistances of the contacts to the arms are sufficiently low that they can force the voltage sensing system to ground in the time allowed for the measurement. This is done by grounding two of the arms and measuring the voltage between the remaining two. If the contact resistance is excessive, the digital voltmeter is effectively open circuited and measures a large voltage. If the magnitude of this voltage, VRES, exceeds the specified maximum (VIϕ), a bad contact is assumed, and testing is halted.

The two-point resistances between each set of arms are measured next. These data are valuable for determining the structural integrity of the arms and also provide a direct internal check on the van der Pauw results if there is no appreciable contact resistance. If the resistance of any arm, RIJ, is greater than the specified maximum (RAMX), testing is halted. This maximum resistance is provided mainly to ensure that the voltage sensing system is not loading the structure during the measurement.

If the testing reaches this point, a test for linearity and bilaterality is done. This test consists of measuring the van der Pauw voltage at the current level found for this structure, at the negative of this value, and at half of this value. Two parameters, TWLIN and BILIN, are calculated to reflect the linearity and bilaterality of the measurements, respectively.

Finally, the actual van der Pauw measurements are performed. These consist of measuring the van der Pauw voltages between four different sets of arms. The sheet resistance, RHOS, and the asymmetry and reciprocity factors, which represent the quality of the structure and of the material, are calculated.

Test blocks are combined to obtain a final modular test program. For the particular example described here, four different van der Pauw sheet resistor structures were to be tested in the same program. From a test program point of view, these structures differ primarily by the pins used. The final test program consisted of the UVDP1 test block repeated four times with only the pin numbers and the structure identifiers changed. It is, of course, necessary to have the appropriate software to effect this integration.

Diagnostic messages are printed on the console during the test execution. These messages describe the faults, structure, and the test block used for the test. If many messages are obtained, something is seriously wrong. Following test execution, the results are presented in computer-generated wafer maps, histograms, or tables, as appropriate.

Measurements were made on a variety of the type I test structures. The results of measurements on the two gated van der Pauw sheet resistors were particularly interesting because they show examples of strong failure of reciprocity. They also clearly show the limitations of the quasi-conventional methods of characterizing SOS films.

These measurements are all performed under constant current conditions. Several of the voltages appearing across the arms are plotted as a function of gate voltage in figure 55. Results from both structures are plotted on the same graph. These structures differ from each other only in the type of contact used; the undoped silicon under the gate is the same in both cases. The undoped silicon is of too high a resistance to be examined by this technique unless the gate voltage is such as to make the silicon conductive by the induced surface charge. For gate voltages near zero, no results are obtained; however, good results are obtained in the range of gate voltage where the surface is made reasonably conducting.

Three sets of curves are plotted for each device. The variation of the applied voltage as a function of gate voltage and the variation of the potential of the intersection are plotted on the same scale (10 mV/div), while the van der Pauw voltages for four different combinations of arms are plotted on the same gate voltage scale but on a 0.1-mV/div scale. The contacts used on these structures have a very small contact resistance. This is seen in the fact that the voltage at the intersection is equal to one half the applied voltage (within 1 mV) at each gate voltage. This means that the field across the oxide at the intersection can be readily calculated from the applied voltage and the gate voltage. It

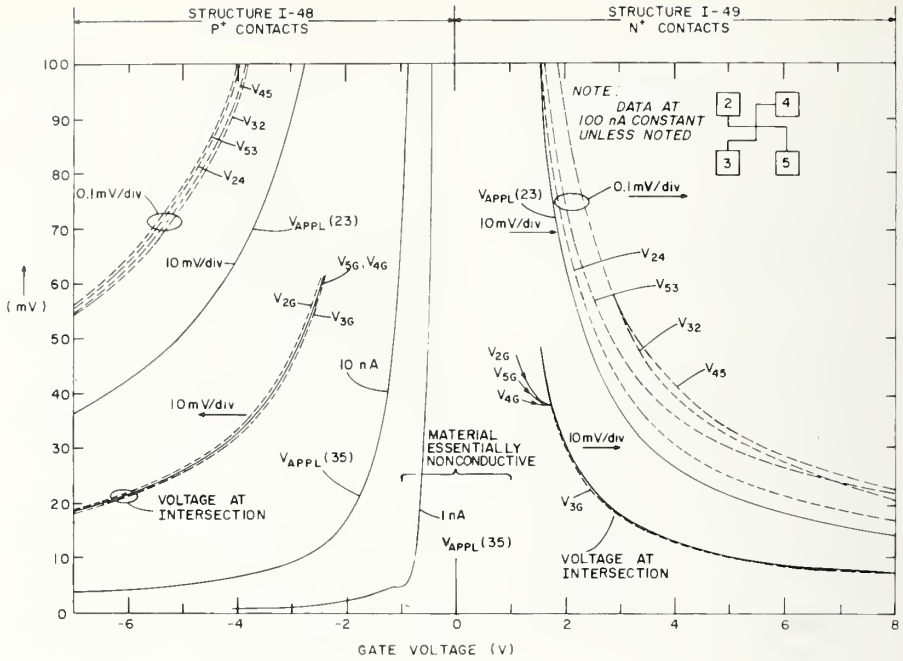

Figure 55. Performance of gated van der Pauw structures at room temperature. (See text for discussion.)

also means that over distances of the order of the 10-mil (0.25-mm) size of the structure that the voltage-current characteristic of the epitaxial silicon in the resistor structure is nonlinear.

On the other hand, serious deviations from the reciprocity demanded by linear systems are found in the van der Pauw voltage, particularly for the structure with n^+ contacts. Considering the highly defected structure of the silicon, it seems to be reasonable to assume the epitaxial silicon exhibits some anisotropy in its conductivity on a local scale. These results demonstrate that the diagnostic power of these test structures is considerable, although accurate testing is somewhat cumbersome and automatic testing of these structures requires special equipment.

(W. E. Ham+)

+Work performed at RCA Laboratories under NBS Contract No. 5-35916. NBS contact for additional information: M. G. Buehler.

8.1. Radioisotope Leak Test

Detailed analysis was completed of the results of the interlaboratory evaluation of the radioisotope method for testing hermeticity of semiconductor devices being developed by ASTM Committee F-1 on Electronics [43]. The purposes of this experiment were both to determine the precision (between-laboratory agreement) inherent in the radioisotope method when applied to production devices with commercially available test equipment and to generate a data base for further refinement of the draft method. To reduce the number of variables involved, one specific model of equipment was used so that all installations could follow the identical operational sequence in using their equipment to carry out the prescribed test procedure. The test procedure itself, however, can be performed with other suitable commercially available test equipment, although actual controls may vary. All equipment was serviced and calibrated prior to carrying out the test procedure.

The test specimens were 100, 14-lead, ceramic-glass, dual-in-line integrated circuit packages with a nominal internal free volume of 0.02 cm^3. The packages were selected to provide a range of leak sizes from less than 1×10^{-8} atm·cm^3/s* to about 5×10^{-5} atm·cm^3/s. Although the packages were selected from normal production lots, they were not subjected to fluid immersion at any time.

Even though it was not clear at the onset that real package leaks were sufficiently stable for such an exercise, the test specimens were circulated through 10 laboratories† with a final repeated test made by the first laboratory to close the loop. All specimens survived.

The radioactive gas used in the test procedure, krypton-85, is a radioisotope with a half life of approximately 10 years. Over 99 percent of the disintegrations involve the emission of beta particles with a maximum energy of about 0.7 MeV, and about 0.5 percent of the disintegrations leads to gamma emission with an energy of approximately 0.5 MeV. In use, the krypton-85 is diluted with nitrogen in the ratio of about 1 to 10^4 to obtain an increased quantity of test gas with a viscosity equivalent to that of air. For the test, the packages are first placed in an activation tank, which is then sealed and evacuated. The krypton-nitrogen gas mixture is pumped into the tank to a prescribed activation pressure. During a prescribed "soaking" time, the gas passes through any package leaks and accumulates in the interior. At the end of the soaking time, the gas mixture is pumped from the activation tank and stored for reuse, the tank is vented, and the packages are examined with a gamma radiation counter to measure the amount of krypton-85 that remains in the interior.

The equation traditionally used to relate the gamma count rate to the leak rate is [44,45]:

$$Q = \frac{R P_o^2}{SKT(P_e^2 - P_i^2)}, \qquad (13)$$

where Q is the leak rate (atm·cm^3/s), R is the count rate above ambient background (counts/min), S is the specific activity (μCi/atm·cm^3) of the gas mixture, K is the overall counting efficiency of the detector for the package type (counts/min·μCi), T is the soaking time, P_o is 1 standard atmosphere pressure, P_e is the activation pressure (atm absolute), and P_i is the initial internal package pressure (atm absolute). This formula assumes that the gas flow through the leak is laminar, that the gas accumulates within the package linearly in time, and that little pressure change occurs in the interior. No provision is included for gas escape after pressurization. Since the emphasis of this experiment was on measurements agreement rather than on absolute value, all but the last of these assumptions were not of consequence. To minimize the effect of gas escape from the package interior, count rate determinations were to be completed within a specified short (dwell) time.

In practice, the hermetic screening process is not a measurement procedure but is a de-

---

*Although the SI system of units is now preferred, present engineering practice uses the mixed units of atm·cm^3/s for leak rate, torr for vacuum, and psi for pressures near or greater than 1 atmosphere. Conversion factors are 1 atm·cm^3/s = 0.10133 Pa·m^3/s, 1 torr = 133.33 Pa, and 1 psi = 6892 Pa.

†The companies which participated in the experiment were the Burroughs Corp.; Fairchild Semiconductor; Hughes Aircraft; IBM Corp. (2 installations); IsoVac Engineering, Inc.; Lockheed Missiles and Space Co.; Motorola, Inc. (2 installations); and TRW Systems.

tection operation for indicated leak rates greater than some set value. Normally the radioisotope method is used as a fine leak test procedure with the rejection limit set at such a value as to allow the detection of some of the larger leak sizes [45]. However, the dynamic range for quantitative measurements with this procedure depends on the range of the rate meter. This range is generally about two orders of magnitude. To meet the objectives of the interlaboratory evaluation, two successive cycles were employed in order to obtain accurate count rates and to prevent overfill with the radioactive gas. The first cycle was a test for the range of leak sizes greater than 1×10^{-6} atm·cm^3/s, and the second cycle was a fine leak test for the indicated range from 1×10^{-8} to about 1×10^{-6} atm·cm^3/s. Packages which unambiguously evidenced a leak greater than 1×10^{-6} atm·cm^3/s in the first cycle were set aside and assigned values as measured. Those packages which evidenced borderline values of about 1×10^{-6} atm·cm^3/s were retested in the second cycle along with the remaining packages which had passed the first cycle.

The count rate for each device was measured initially at each installation to establish the background level for each device. For the first cycle, the activation pressure was nominally 3 atm(abs) and the soaking time was 36 s with a final pump-down to 2 torr. Individual packages were measured in the counting station; all measurements were scheduled for completion within 15 min after removal from the activation tank. Actually, the time taken for completion ranged from 15 to 40 min. Leak rate values were calculated from eq (13).

The fine leak test was performed in the same manner as the first-cycle leak test. Pressurization was nominally 5 atm(abs); soaking time was determined from eq (13) based upon the particular value of indicated specific activity at each test site so that the count rate for a leak size of 1×10^{-8} atm·cm^3/s was about 1000 counts/min higher than the background count rate. The calculated soaking time was generally 12 to 18 min. Final venting pressure was 0.5 torr. Although not generally considered necessary for fine leakers, a 30-min time limit for completion of counting is good practice. Actual times ranged from 17 to 80 min.

After testing at each site, the specimens were deactivated of krypton-85 by storing them in a vacuum chamber for about 48 h. At each of the succeeding installations, background count rates before test were nominally 2000 counts/min or less for each device.

Of those borderline packages which evidenced leak rates of about 1×10^{-6} atm·cm^3/s in the first cycle, most exhibited a well-defined test value in the second cycle which was about one decade smaller than the value measured in the first cycle. In such cases, the fine leak values were assigned to them. The remaining borderline leakers exhibited large count rates of the order of 10^5 counts/min in the second cycle, in which cases the value measured in the first cycle was assigned. With this distinction, the between-laboratory agreement of whether leaks were greater than 1×10^{-6} atm·cm^3/s or not was 100 percent. This agreement would not have resulted had the borderline specimens not been retested in the fine leak cycle.

In the initial selection, 25 packages were identified as non-leakers (leak size less than 1×10^{-8} atm·cm^3/s). Of the 275 measurements on these packages, 261 (95 percent) confirmed the initial assignment. The 14 measurements which indicated leak sizes greater than 1×10^{-8} atm·cm^3/s were made on 10 packages; no more than two such measurements (of a total of 11) occurred on any package.

The average leak size and the sample standard deviation were determined for each test package from the 11 measured values of leak size; an indication of no leak (less than 1×10^{-8} atm·cm^3/s) was assigned a value of zero. The sample standard deviation is plotted in figure 56 as a function of average leak size; from this plot it is apparent that the imprecision increases systematically with leak size for both leak ranges. The data also show that no packages had leak sizes between 3×10^{-7} and 1×10^{-6} atm·cm^3/s. It is not clear whether this result occurred because of the selection process or whether it is reflective of the nature of the leaks in this type of package. The large dispersion for the range of leak sizes greater than 1×10^{-6} atm·cm^3/s is certainly affected by the variation in dwell times that occurred at some of the installations.

Regression calculations show that for both the fine and larger leak ranges the variation in between-laboratory reproducibility is well described by equations of the form

$$\log \frac{S_j}{x_o} = a_0 + a_1 \log \frac{\bar{x}_j}{x_o}, \qquad (14$$

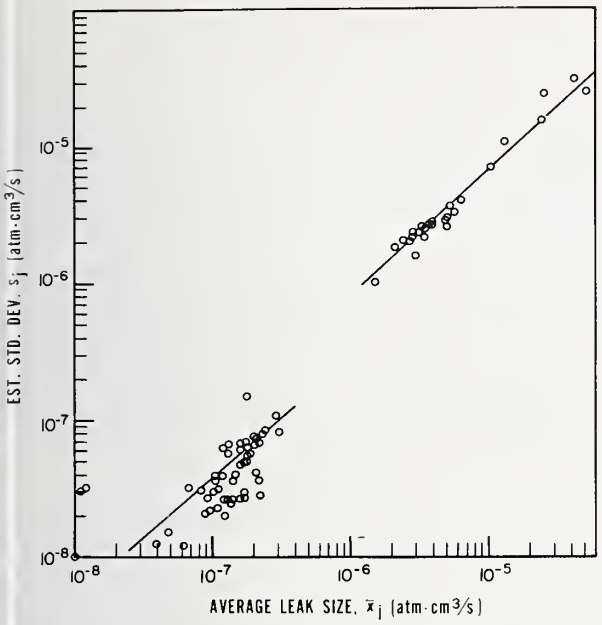

Figure 56. Computed sample standard deviations, s_j, of measured leak sizes for all test leaks as a function of average leak size, $\bar{x}_j$. (The solid lines are calculated from eq (14).)

where s_j is the sample standard deviation and $\bar{x}_j$ is the average leak size of the jth test package. Values of the regression coefficients a_0 and a_1 and the normalization leak size x_o are listed in table 11, together with the correlation coefficient of the fitted lines. The regression lines are plotted in figure 56; note that they are not continuous over the entire leak size range covered.

More detailed examination of the data indicates that part of the overall systematic dependence of dispersion on leak size is the result of individual laboratory measurement biases. It is of interest to speculate on the precision that could possibly be obtained were laboratory biases eliminated. This possible precision was anticipated by taking the apparent precision at each laboratory and pooling the results for each test specimen. Specifically, a linear regression calculation of the form $x_{ij} = a + b\bar{x}_j$, where x_{ij} is the leak size measured by laboratory i on test specimen j, was applied to each laboratory's results. The residuals were calculated for each test specimen from each laboratory's regression line as $x_{ij} - \hat{x}_{ij}$, where $\hat{x}_{ij}$ is the expected value as calculated from the regression line for each laboratory at the corresponding value of $\bar{x}_j$. A standard deviation s_r was then calculated from all the residuals for each specimen and, again, a regression curve was fitted. Results are represented by curve a in figure 57 for the fine leak range and by curve a in figure 58 for the larger leak range. Actual precisions that were obtained in the test, when laboratory biases are included, as computed from eq (14), are given as curves b in the figures. From these results it would appear that the precision could be improved by a factor of about 2 if laboratory biases could be eliminated. Identification of the factors which cause this bias remains for further effort.

The actual precisions determined in this experiment are dependent on the guidelines imposed and on the type of test specimen used. Values would probably be affected by change in package materials and internal free volumes. However, these results demonstrate that an interlaboratory comparison of hermetic packages can be accomplished with this radioisotope method and that one can achieve a measurement precision which is greatly improved over the one or more orders of magnitude differences that have heretofore been the rule. Although the precision achieved

Table 11 — Regression Coefficients for Radioisotope Leak Test Results

	a_0	a_1	x_0, atm·cm³/s	Correlation Coefficient
Fine Leak Range	-0.280	0.839	10^{-8}	0.980
Gross Leak Range	-0.106	0.947	10^{-6}	0.989

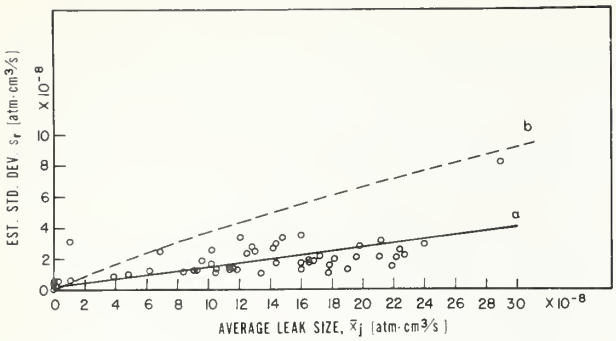

Figure 57. Computed sample standard deviations, s_r, of residuals for each test specimen in the fine leak range as a function of average leak size, $\bar{x}_j$. (Computed points are represented by open circles; the solid line is obtained from an equation of the form of eq (14). For comparison, the regression line for the measured sample standard deviations, s_j, is shown as the dashed line.)

here is probably better than that to be expected in the normal production environment, the guidelines imposed can be transferred readily and should lead to improvements there also. (S. Ruthberg[§])

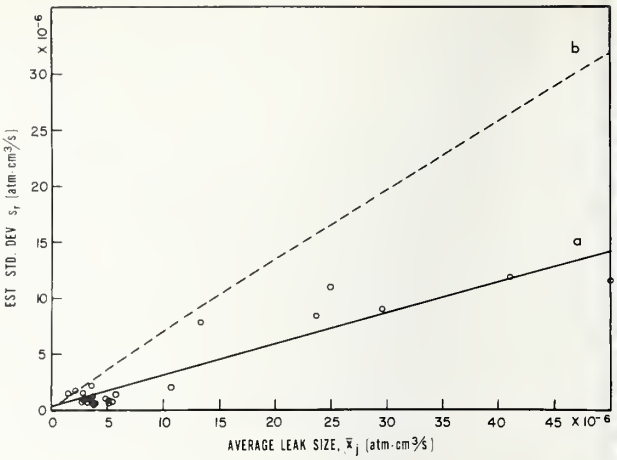

Figure 58. Computed sample standard deviations, s_r, of residuals for each test specimen in the gross leak range as a function of average leak size, $\bar{x}_j$. (Computed points are represented by open circles; the solid line is obtained from an equation of the form of eq (14). For comparison, the regression line for the measured sample standard deviations, s_j, is shown as the dashed line.)

[§] G. R. Neff, IsoVac Engineering, Inc., and B. P. Martin, IBM Corp., were co-leaders of the interlaboratory experiment.

9. DEVICE INSPECTION AND TEST

9.1. Scanning Acoustic Microscopy

Additional studies of resolution and contrast were conducted on the developmental scanning acoustic microscopes [46] at both Stanford University and Hughes Research Laboratories. In addition, modifications have been made to improve the instruments at both locations.

Stanford Project — Investigation of a selection of silicon and sapphire surfaces continued in order to improve the understanding of acoustic microscopy as applied to silicon devices. Stacking faults have been observed in epitaxial layers of silicon. Figure 59 shows a typical example, a stacking fault on the surface of a 25-μm thick, (100) epitaxial silicon layer, as viewed both by interference contrast (Nomarski) optical microscopy and by scanning acoustic microscopy. Although the acoustic micrographs are somewhat more coarse due to the lower resolving power and the presence of the scan lines, they seem to contain all of the important features contained in the optical image.

It has been found that small pinholes in a film, approximately one-quarter wavelength thick sputtered on a smooth surface, show up as very bright high contrast points in the image. This is to be expected on the basis of the work at Hughes on anti-reflection coatings on the sapphire lens surfaces (NBS Spec. Publ. 400-29, p. 83) [47]. An example of pinholes in a 1.5-μm thick borosilicate glass layer sputtered on flat polished sapphire is shown in figure 60. In this image the beam was focused at the surface of the glass layer; in addition to the pinholes, two scratches can be seen. Similar effects were also observed on silicon wafers covered with a 1-μm thick silicon dioxide layer.

These studies also revealed a dependence of the image on axial position of the focal point of the acoustic beam. Previous work at Hughes demonstrated that there were variations in contrast and contrast reversals as a function of the axial position (NBS Spec. Publ. 400-36, pp. 55-56). These differences were attributed to differences in levels at the surface of the test specimens and to the properties of the transducer-lens combination.

The present work showed that the strength of the returning signal can be strongly affected by the acoustic energy reflected from the various interfaces beneath the surface which, in turn, is strongly dependent on the angle of convergence of the incident beam. As the test specimen is translated along the axis toward the lens, the beam convergence at the liquid-specimen interface increases.

The focus of the beam can be moved from the surface at the liquid interface into the interior of the specimen when the specimen is accurately translated toward the lens. If this focal point coincides with an interface between two different materials, such as silicon dioxide and aluminum, the return signal changes in strength. For this focal condi-

a. Optical (Nomarski) photomicrograph. (Magnification: 120X.)

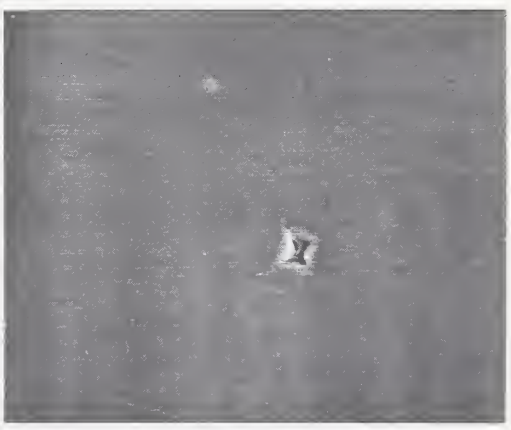

b. Acoustic (800-MHz) micrograph. (Magnification: 200X.)

Figure 59. Stacking fault on unoxidized [100] epitaxial silicon layer 25 μm thick grown on sapphire substrate.

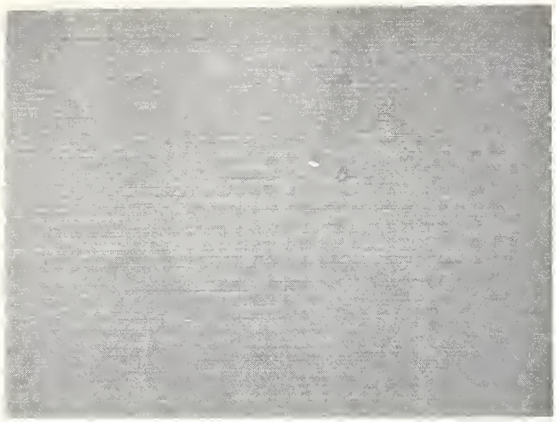

Figure 60. Acoustic micrograph of pinhole defects in a 1.5-μm thick borosilicate glass layer sputtered on a flat polished sapphire substrate. The acoustic beam is focused on the glass surface. (Magnification: 400X.)

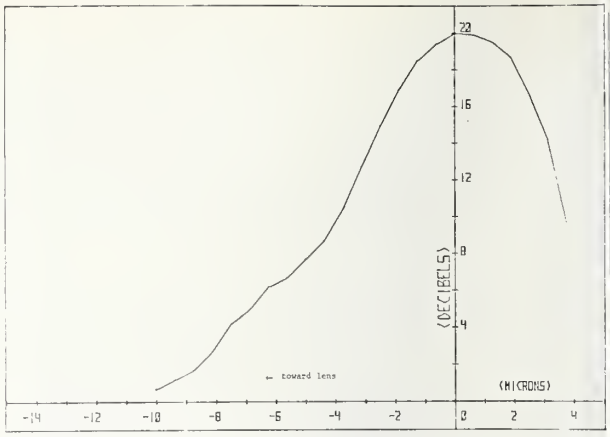

Figure 61. Computed strength of reflected acoustic signal as a function of axial position of single surface of sapphire. (At 0, acoustic beam is focused on the sapphire surface; negative values indicate motion of surface toward acoustic lens.)

tion, the image reveals structural information that is beneath the surface. Information of this kind is not accessible to other forms of microscopy.

Consider first the case of a single layer. A clean surface of sapphire, which has an impedance that is much larger than water, serves as an excellent reflector. The variation of the reflected signal as the surface is moved along the beam axis is shown in figure 61. At the point marked 0 on the figure the reflected signal is a maximum; at this point the beam is focused on the surface. As the specimen is moved from this point, either toward the lens or away from the lens, the return signal decreases in amplitude. This is a result of the defocusing of the beam at the reflecting surface. The width of the curve gives an effective "depth of focus" of the acoustic beam.

Figure 62 is a series of images of a silicon wafer covered with silicon dioxide. The islands (which show up as bright regions in fig. 62a and dark regions in fig. 62b) are composed of three layers: a 28-nm thick film of silicon dioxide covered by a 350-nm thick deposited layer of silicon nitride covered by a 200-nm thick deposited layer of silicon dioxide. The remainder of the slice is covered with a 1.56-μm thick silicon dioxide film thermally grown in a wet ambient at 1100°C for 5 h. In this process the level of the silicon is lowered and as a result the oxide-silicon interface for the regions outside the islands is 450 nm below that of the islands.

The surfaces of the islands are about 530 nm below the surface of the oxide layer. The image in figure 62a was made with the beam focused at the surface of the islands and the image in figure 62b was made with the focal point of the beam 10 μm below this surface.

The reversal of contrast in these images may be understood by referring to the measured curves of reflected signal as a function of axial distance shown in figure 62c. When the acoustic beam is directed on the thermal oxide, the response is given by the curve marked A, and when the beam is directed on the islands, the response is given by the curve marked B. The origin is the position of the specimen when the beam is focused on the top of the islands; negative distances represent translation of the specimen toward the lens. At the origin, the signal from the island areas is greater than that from the areas covered with thermal oxide so the island areas appear lighter as in figure 62a. When the specimen is moved 10 μm toward the lens, the signal levels are reversed and the islands appear darker as in figure 62b.

The reflected signal curves (fig. 62c) also show another interesting feature. To the left of the primary maximum, near the origin, the response curve has a steep slope. The signal changes by 1 dB for a translation of 150 nm. Since it should be possible to monitor changes in signal strength that are a fraction of a decibel, thickness changes of

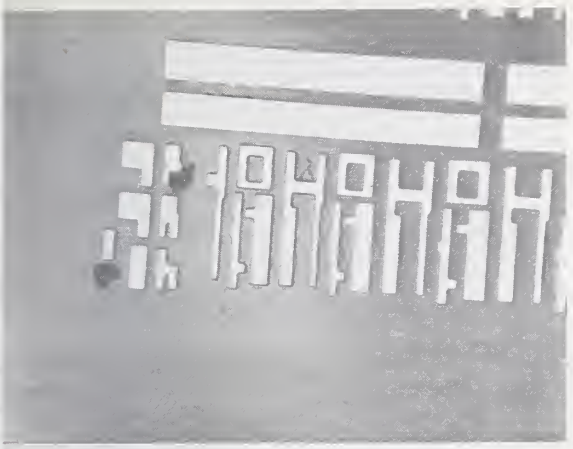

a. Beam focused on island surface.

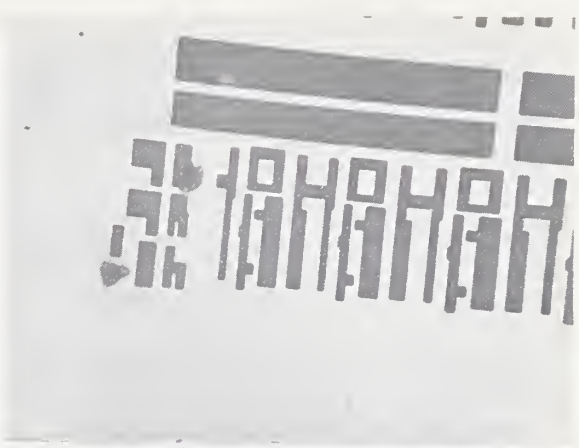

b. Beam focused 10 μm below island surface.

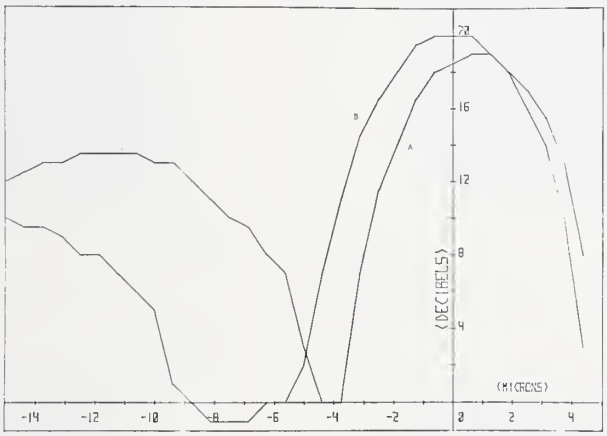

c. Reflected acoustic signal as a function of axial position. Origin represents focus of beam on island surface. Curve A: Off-island. Curve B: On-island.

Figure 62. Contrast reversal of acoustic micrographs of oxidized silicon pattern resulting from change in focal position.

few tens of nanometers should be detectable. Preliminary calculations indicate that sensitivity to thickness changes are greatest when, as in this case, the nominal layer thickness is about one-quarter of a wavelength.

It is not yet possible to define with precision the type of configuration that gives rise to the second peak, but it appears to be related to the value of the acoustic impedance of the layer as compared to the substrate. When the layer impedance is smaller than the impedance of the substrate, the low impedance layer acts to couple energy more efficiently into the substrate, and the second peak occurs when the focal point is moved in depth until it coincides with the interface. Aluminum layers on sapphire and silicon are examples of this case. When the impedance of the layer is higher than the impedance of the substrate, the presence of the layer increases the reflected signal. For that situation, a second peak is not always obtained. There is no evidence for a second peak with a gold layer on silicon, but there is for a layer of silicon nitride on silicon.

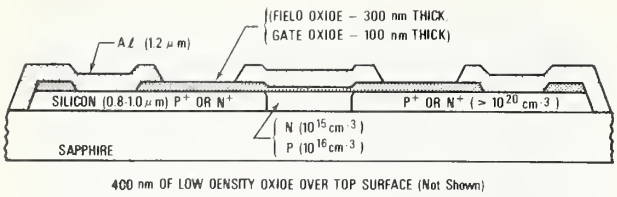

a. Depth profile of a transistor section of circuit.

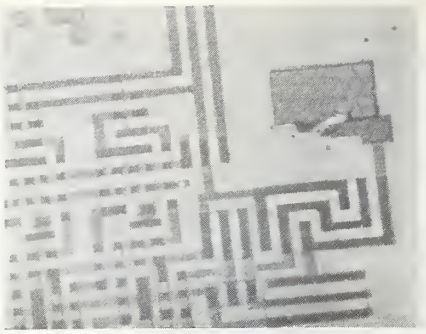

b. Acoustic micrograph with beam focused on sapphire surface. (Magnification: 225X.)

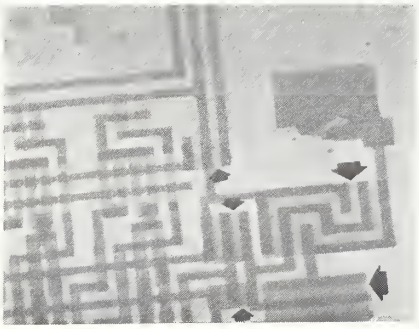

c. Acoustic micrograph with beam focused 2 μm below sapphire surface. Arrows indicate typical silicon islands. (Magnification: 225X.)

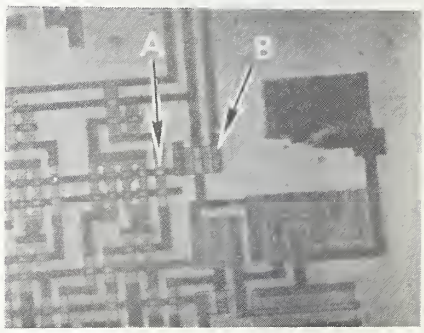

d. Acoustic micrograph with beam focused 4 μm below sapphire surface. A: Aluminum over 300 nm of oxide over silicon. B: Aluminum over silicon. (Magnification: 225X.)

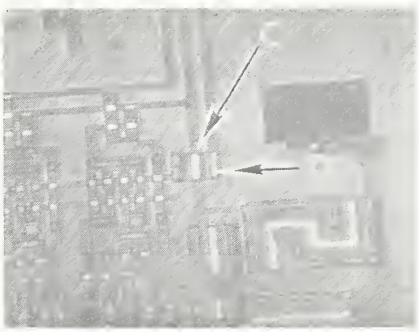

e. Acoustic micrograph with beam focused 6 μm below sapphire surface. C: Aluminum over 100 nm of oxide over silicon. D: Aluminum over silicon. (Magnification: 225X.)

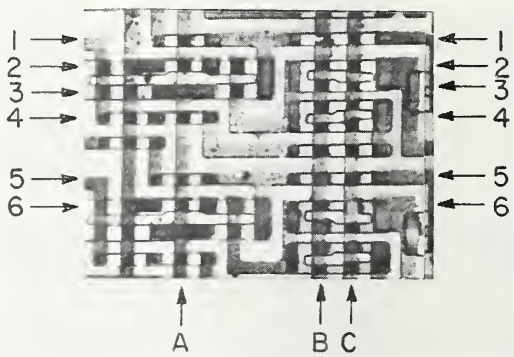

f. Acoustic micrograph of different portion of circuit showing different crossover characteristics at crossover C-6. (Magnification: 325X.)

Figure 63. Aluminum-gate, silicon-on-sapphire STDL-4 integrated circuit.

These results are illustrated by the images of a portion of an aluminum-gate, silicon-on-sapphire STDL-4 circuit [48] shown in figure 63. The depth profile of a transistor section of this circuit is shown in figure 63a. The image in figure 63b was made with the beam focused on the sapphire surface. The image there compares favorably with an optical photomicrograph. The aluminum layers overlaying the silicon appear dark since this combination effectively couples the energy into the sapphire substrate and reduces the reflected signal. Translation of the device 2 μm toward the lens results in an image (fig. 63c) that does not differ significantly from the previous image except that the silicon islands (arrows) show greater contrast to the sapphire. Translation an additional 2 μm toward the lens results in an image (fig. 63d) with contrast reversals in the regions where aluminum passes over silicon bars covered with 300 nm of silicon dioxide (such as A) and aluminum-silicon contacts (such as B). In the image obtained after an additional 2 μm translation toward the lens (fig. 63e), the gate electrodes of the transistors appear very bright. The gate electrode (such as C) is separated from the silicon by 100 nm of oxide while the source and drain electrodes (such as D) are applied directly to the silicon.

An image of a different part of this circuit (fig. 63f) illustrates the ability of the scanning acoustic microscope to observe features under the surface. The vertical line of metallization A exhibits regions of high contrast at the points where it crosses horizontal silicon bars such as those marked 1, 2, and 3. An illustration of why this is potentially important is seen where vertical line C crosses horizontal line 6. There is a dark square where the vertical and horizontal lines cross except for the crossing C-6. At this crossing, the dark square is missing, probably because of a defect in the structure at this point. Other features on this circuit which stand out clearly in the acoustic micrograph are: 1) the apparent bubble or ball in the center of the horizontal line 5 and 2) the apparent narrowing of vertical line B as it crosses horizontal line 1. Neither of these features was readily apparent on an optical photomicrograph of this portion of the circuit.

The principal improvement in the instrumentation is the addition of a microprocessor-based signal processing capability. In one instance the signal is stored one line at a time and the second derivative computed with the microprocessor. A portion of this second derivative is added to the original signal to form the final image. This provides significant edge enhancement and emphasizes those features that are dim if not unobservable in the unprocessed image. (C. F. Quate*)

Hughes Project — High resolution test targets have been used to measure the spatial frequency response of the scanning acoustic microscope [49,50]. The measurements of the acoustic contrast characteristics and gray scale present greater difficulties. First, image contrast may be obtained using either phase or amplitude information and it is conceivable that a combination of the two (not necessarily related) may be used to obtain greater contrast and possibly greater enhancement of detail than can be realized by using either type of information separately. Second, and fundamentally different from the light image system, the available material properties for producing layered structures do not permit the fabrication of a continuum of reflective properties through which contrast is achieved.

One way to realize a reflection gray-scale bar chart in a water immersion system is to fabricate a series of identical bars with increasing thickness up to one-quarter wavelength of a material with a large reflection coefficient, such as gold, on a highly absorbent substrate. In the absence of an easily obtainable substrate with this desirable property, the gold can be deposited on a substrate such as sapphire on which an acoustic anti-reflection coating (AARC) [47] has been deposited. This type of structure, illustrated in figure 64a, can suffice for a pulsed reflection experiment if all but the desired image signal is gated out and if the measurement is carried out at the characteristic frequency of the AARC. An alternative version of an acoustic gray-scale bar chart can be realized by depositing (sputtering) layers of light crown glass on sapphire in thickness increments from zero to one-quarter wavelength to achieve equal increments of amplitude or power reflection coefficient as illustrated in figure 64b. Both types of gray scale may be useful in examining the validity of the analytical predictions of the two systems, using metal-dielectric or solely dielectric materials. A gray-scale

*Work performed at Microwave Laboratory, Stanford University, under NBS Contract No. 5-35899. NBS contact for additional information: R. I. Scace.

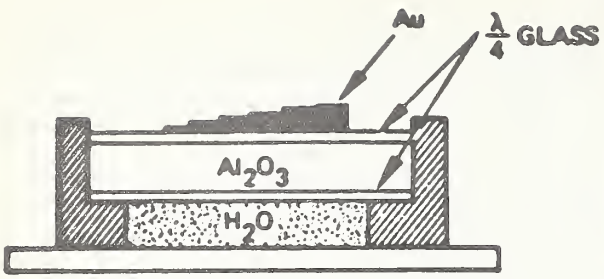

a. Gold bars on sapphire substrate with anti-reflection coating.

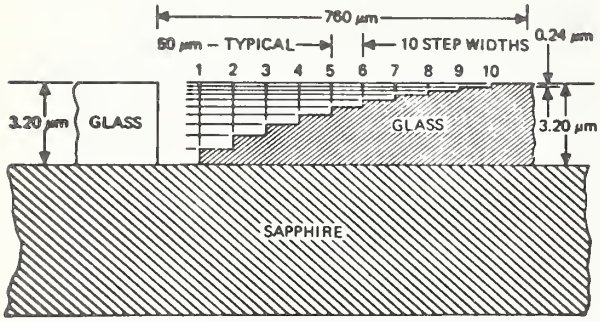

b. Glass layers on sapphire substrate

Figure 64. Cross sections of acoustic gray-scale test patterns for measurement of contrast characteristics of a scanning acoustic microscope.

pattern of the sputtered-glass type has been fabricated and is being tested. It should be noted that the dimensions given in figure 64b are appropriate for a frequency of about 375 MHz and scaling would be required if a different frequency were used.

A variety of electronic and mechanical improvements to the scanning acoustic microscope are being made. In particular, the hydraulic scan drive was converted to a direct mechanical drive (vertical scan direction), a simple adjustable specimen mount was built, and sample-and-hold circuitry to provide improved display capabilities was assembled.

(R. G. Wilson† and R. D. Weglein†)

9.2. Integrated Circuit Die Attachment Evaluation

The experimental investigation of the suitability of using the temperature response of the substrate diode in an integrated circuit to evaluate the integrity of the die attachment was completed. This method is similar

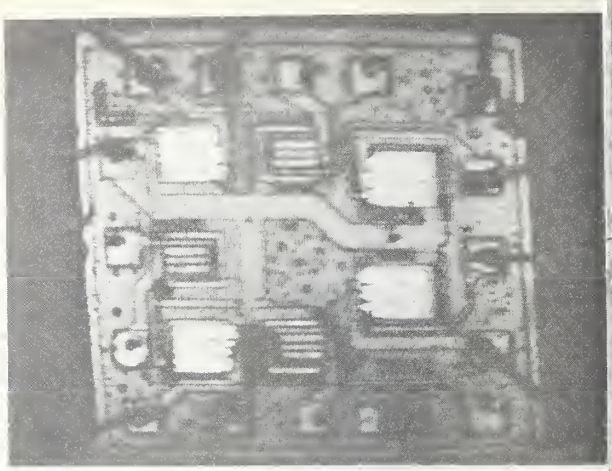

Figure 65. Laser scanner photoresponse image of integrated circuit used in this study. (Electrically active devices are light.)

to that previously developed for evaluating the integrity of the die attachment of transistors and diodes [51]. The circuit is pulsed for a time short compared with the thermal time constant of the case but longer than the thermal time constant of the device die. The temperature rise of the die is determined by the use of an appropriate temperature sensitive parameter. Since defects in the bond between the die and the header result in higher die temperatures, the amount of temperature increase above that which would be expected for a good bond gives an indication of the quality of the die attachment. In the present study, the voltage drop across the substrate diode with a fixed forward current was evaluated as the temperature sensitive parameter.

In the test devices, a voided region was introduced between the header and the die by making a circular depression on the header and bonding the die over the depression. The devices used for the investigation were integrated circuit transistor arrays. Each integrated circuit die consisted of seven common collector transistors on a common substrate. Four of the seven transistors on the die were connected after the die was bonded to the header as illustrated by the laser scanner photoresponse image in figure 65. The circuit dice were squares 50 mils (1.27 mm) on a side and were bonded with an eutectic al-

†Work performed at Hughes Research Laboratories under NBS Contract No. 5-35898. NBS contact for additional information: R. I. Scace.

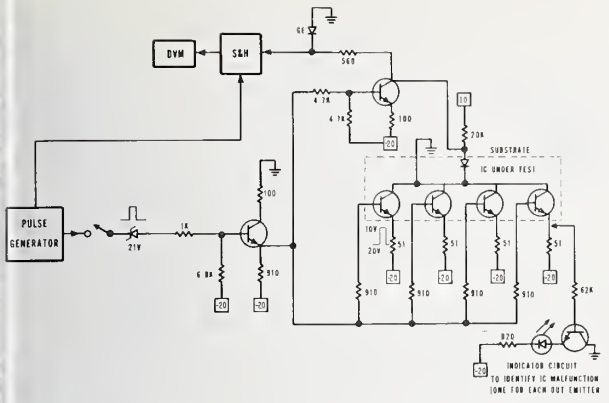

Figure 66. Circuit for evaluating integrated-circuit die-attachment integrity.

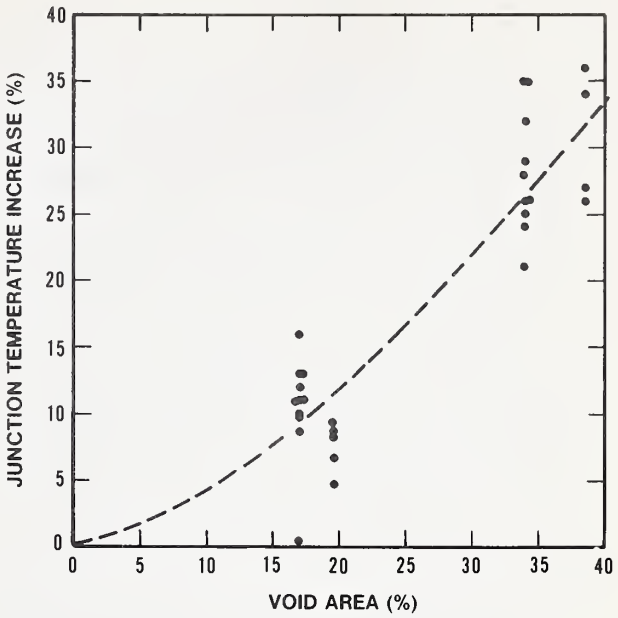

Figure 67. Percent increase in junction temperature as a function of intentional void area. (Solid dots: measured increase. Dashed line: estimated best fit to the data.)

loy over voids with diameters ranging from 23.5 to 35 mils (0.60 to 0.89 mm), thus representing bond deficient areas ranging from about 17 to 38 percent of the die area. In addition, 33 dice were successfully bonded to headers that had no voids to serve as control devices.

The temperature rises in both the voided and control devices were measured to determine the increase in die temperature as a function of void size. The schematic diagram of the circuit used to measure the temperature rise is shown in figure 66. Prior to heating, the voltage of the substrate diode was measured with a forward current of about 0.5 mA. To heat the die, a 12.8-ms wide pulse was applied to the bases of the four transistors which were connected in a common collector configuration and operated as emitter followers. During the heating pulse, the substrate diode was reverse biased to insure proper transistor action. After the heating pulse had been applied, the transistors in the integrated circuit were turned off and the voltage of the substrate diode was again measured with a forward current of 0.5 mA. A small delay was needed to allow transients to die out of the system. The temperature coefficient of the diode voltage was found to be -2.3 mV/°C by heating the entire device up to known temperatures with no heating pulses applied to the integrated circuit, and measuring the substrate diode voltage as a function of temperature. During the heating pulse, the circuit dissipated 8 W, but since the duty cycle was 0.8 percent, the average heat dissipation was 64 mW; because of this low average dissipation, special heat sinking was not required.

The results of this study are given in figure 67 where the percent increase in temperature is plotted as a function of the nominal void size. The spread in the data is fairly large. This is due mostly to variations in the quality of the die attach in those areas where there was no intentional void. The zero point on the graph was based on the average temperature rise for the control group. It can be seen that with the transient technique used in this study a void covering roughly 35 percent of the die area produced a 27.5 percent increase in the temperature rise over what it would be had there been no void. As had been noted in the previous study [51], steady-state thermal resistance measurements on these devices were much less sensitive; only a 10-percent increase in steady-state temperature rise was produced by a void covering 35 percent of the die area.

Substantial variations in the quality of the die attach were observed on some of these devices with the use of radiographic x-ray techniques. Several dice which had very large temperature rises (not included in fig. 67) appeared to be bonded to the header only along one side of the die. Unfortunately, the resolution of the radiographs was insuf-

ficient to permit quantitative determination of an actual void area.

These results suggest that, at least in some cases, the temperature response of the substrate diode can provide information regarding the quality of integrated circuit die attachment. (D. W. Berning)

9.3. Transistor Collector-Emitter Saturation Voltage[§]

Investigation of the measurement of transistor collector-emitter saturation voltage was undertaken to develop a standard method for determining this parameter which is important because it can be used to predict the performance of a transistor used in switching apparatus such as in dc to ac power inverters, chopping circuits, or logic circuits. It represents the "zero" logic level in many types of digital circuits. It is important to know how low the collector-emitter voltage becomes in saturation because during saturation the transistor passes the most current for the longest periods of time, and power dissipation at the collector can become excessive if the voltage drop is too high. When a system design is to be used in a radiation environment, it is important to know the change in saturation voltage as a result of radiation dose so that the design can accommodate the changed value. The experimental study was completed and a standard procedure has been proposed [52].

By definition [53], a transistor is operating in the saturation region when both the emitter-base and the collector-base junctions are forward biased. The collector-emitter voltage in this condition is usually represented in specification literature by the symbol $V_{CE(SAT)}$. This voltage is the sum of the junction saturation voltage and the resistive drops in the neutral regions of the transistor. The junction saturation voltage is the difference between the forward-biased junction voltages of the collector-base and the emitter-base junctions. This voltage is normally small and rather insensitive to variations in collector or base current because of its logarithmic dependence on these currents. There are three elements to the resistive drops but the most significant, particularly for power transistors, is usually that across the collector region. The collector region of many power transistors is lightly doped to obtain high breakdown voltages and the transistor is usually operated at high currents in saturation.

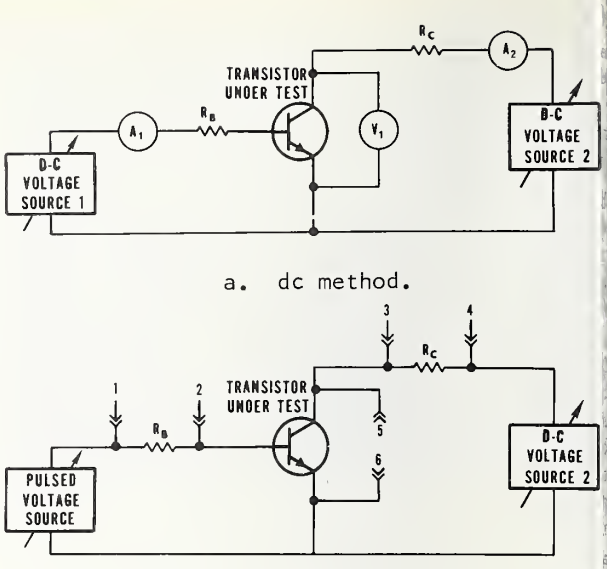

a. dc method.

b. Pulsed method.

Figure 68. Test circuit for measuring $V_{CE(SAT)}$.

In the application of a transistor in a circuit, it is not always necessary to know the actual value of $V_{CE(SAT)}$. Rather, it is frequently only important to know that for the bias conditions of interest, the collector-emitter voltage is less than a specified value. To determine this, it is necessary only to control the test conditions so that the measured value of $V_{CE(SAT)}$ is low enough to meet the specification. To measure a change in $V_{CE(SAT)}$, however, it is necessary to make the measurement twice with all of the important independent variables specified and carefully controlled. The purpose of the present work was to provide a method with test conditions defined thoroughly enough that accurate measurements of changes in $V_{CE(SAT)}$ can be made.

Circuits for making the measurement under dc or pulsed conditions are given in figure 68. The dc method is applicable for currents low enough to produce negligible heating in the junction, while the pulsed method is applicable for currents which would cause significant heating in the junction if not pulsed. In carrying out the measurement, the base and collector currents of the transistor under test are each in turn adjusted to be at a

[§] Principally funded by the Defense Nuclear Agency.

specified value. Then the collector-emitter voltage is measured.

Experiments were performed to determine the sensitivity of the measured $V_{CE(SAT)}$ to the ambient and junction temperatures, the base and collector currents and their ratio, and series resistance and other properties of the measuring circuit. Three transistor types were chosen for these experiments: a small-signal transistor (2N2222), a single-diffused power transistor (2N3055), and a triple-diffused power transistor (2N5840). These device types were selected to provide a wide variation in measured results for variations in the measurement conditions. Three devices of each type were used for each experiment. All were off-the-shelf commercial transistors. Though the number of devices used is small, the data indicate the trends in the effects of the variables and, as such, indicate which parameters are necessary to control carefully and which are not.

To simulate a rise in the ambient temperature, the transistors were placed in a heated oil bath whose temperature was controlled at approximately 10°C intervals from room temperature to 100°C during measurement of $V_{CE(SAT)}$. Sufficient time was allowed for the transistor to reach a steady-state temperature between measurements. The results showed that for ordinary measurements on most devices normal laboratory temperature conditions are adequate as deviations of less than 10°C result in changes in $V_{CE(SAT)}$ of less than 5 percent. However, when very precise measurements are required on certain transistors, especially transistors with a very low doping level in the collector region, greater control of the ambient temperature is required.

Based on the manufacturer's specified value of thermal resistance for these devices, the rise in junction temperature would not exceed 2 or 3°C at the low power levels of the saturation region if the transistor is properly mounted with a heat sink. Such a temperature rise would have a very small effect on the measured value of $V_{CE(SAT)}$. However, should the measurement be made in a condition where the transistor was not properly mounted on a heat sink, careful attention must be paid to the power dissipation during the measurement.

Measurements of the collector-emitter voltage were made for the three transistor types as a function of the base and collector currents. Variations in these currents affect the measurement in two ways. First, when the resistive drop across the collector region is the most significant contributor to $V_{CE(SAT)}$, a change in collector current produces a change in the measured value of $V_{CE(SAT)}$ which is approximately proportional to the change in collector current. Second, for some values of base and collector current, the transistor may operate in the active region instead of the saturation region. This will increase the measured value of V_{CE} by several hundred percent for changes in I_C of only tens of percent. Obviously, this value of collector-emitter voltage is not $V_{CE(SAT)}$. Assuring that the transistor is indeed operating in the saturation region during the measurement of $V_{CE(SAT)}$ is of utmost importance. In practice both the base current, I_B, and the collector current, I_C, to be used in performing the measurement are specified. The dc common emitter current gain, β, is the ratio of I_C to I_B. When the transistor is operating in the saturation region, this ratio is referred to as the forced gain, since both I_C and I_B are set in order to force the transistor to operate in saturation. It is convenient to consider a transistor to be in saturation if the forced β is much lower than the normal β of the transistor operated in the active region. When the forced β approaches the normal β of the transistor, small variations in I_C give increasingly larger variations in V_{CE}. Under these conditions, precise measurement of V_{CE} is difficult and it is doubtful whether the results represent $V_{CE(SAT)}$.

There are other practical considerations for measuring $V_{CE(SAT)}$ particularly in power transistors where the collector currents used can be many amperes so that even a small series resistance in the voltage measuring circuit can be a serious source of error. The use of Kelvin connections, in which the voltage measuring circuit is separated from the current driving circuit, can eliminate most of these series resistance problems. The voltage measurement is made with a very high impedance instrument so that there is a negligible amount of current in that portion of the circuit. There is a separate set of leads to which the current driving circuit is attached. If there is an extraneous resistance in the voltage measuring circuit, the voltage drop

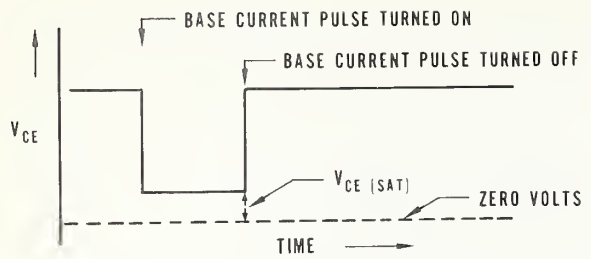

Figure 69. Voltage waveform as observed with an oscilloscope in the pulsed method.

across it is negligible. If there is an extraneous resistance in the current driving circuit, the voltage drop across it is not involved in the voltage measurement and therefore will not lead to an error in measuring $V_{CE(SAT)}$. Kelvin connections need be made only to the emitter and collector leads; no voltage measurement is made in the base circuit so that Kelvin connections are not required.

The effect of the series resistances in the circuit between the transistor and the point where the voltage sensing connection is made is not correctable by the use of Kelvin connections. The current provided by the current driving circuit causes a voltage drop across such a resistance which is measured by the voltage measuring circuit as part of $V_{CE(SAT)}$. An example of such a resistance is the resistance of the leads of the transistor. For this reason, it is important that contact be made reproducibly to the transistor within 3 mm of the transistor case. Another source of such a resistance is poor or dirty contacts. This source can be avoided by using a transistor holder which has good quality contacts which are kept clean.

Another source of error in the measurement of $V_{CE(SAT)}$ is variation in the measurement circuit itself. The current levels used, particularly for power transistors, require considerable power dissipation in the resistors in the collector circuit. Care should be taken to select resistors that are capable of handling this power without changing resistance. If the currents I_B and I_C are determined by

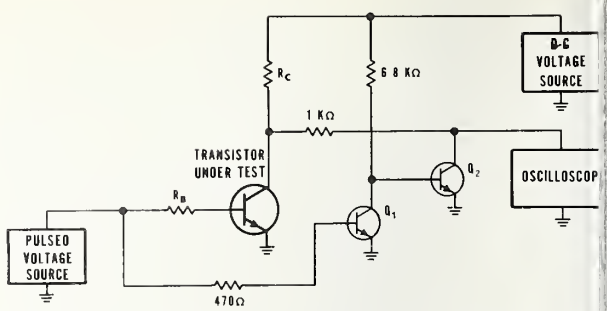

Figure 70. Measuring circuit with clamping circuit attached.

measuring the voltage drops across resistors in the base and collector circuits, it is particularly important to assure that these resistors do not heat up because of excessive power dissipation. A temperature drift in these resistors could cause serious error in the measurement of $V_{CE(SAT)}$ because the measurement would be made at the wrong values of I_B and I_C.

When the pulsed method is used, the voltage measurement of $V_{CE(SAT)}$ must be made with an instrument capable of measuring the voltage of one portion of a pulse with respect to the ground potential. A typical pulse is shown in figure 69. This measurement can be made with an oscilloscope if it is capable of accurately following the pulse from the high level which occurs when the current pulse is off to the low level of $V_{CE(SAT)}$ when the current pulse is on. If, however, the amplifiers in the oscilloscope saturate, an erroneous measurement of $V_{CE(SAT)}$ will be made. One way to avoid this is by application of a clamping circuit, such as that shown in figure 70, at the input of the oscilloscope. The effect of this circuit is to lower the voltage during the time the current pulse is off so that it is similar in magnitude to the value of $V_{CE(SAT)}$ when the current pulse is on. An oscilloscope can easily follow the new pulse shape without saturating.

(K. O. Leedy)

10. REFERENCES

Blackburn, D. L., Schafft, H. A., and Swartzendruber, L. J., Nondestructive Photovoltaic Technique for the Measurement of Resistivity Gradients in Circular Semiconductor Wafers, *J. Electrochem. Soc.* 119, 1773-1778 (1972).

Swartzendruber, L. J., Four-Point Probe Measurement of Non-Uniformities in Semiconductor Sheet Resistivity, *Solid-State Electronics* 7, 413-422 (1964).

Vieweg-Gutberlet, F., and Schönhofer, F. X., Grenzen der Anavendbarkirt des 4-Spitzen-Gleichstron-Messverfahrens an Silicium-Proben, Tiel I u. II, *Archiv. techn. Messen*, No. 369, 237-240 (October 1966) and No. 370, 259-262 (November 1966).

Blackburn, D. L., Koyama, R. Y., Oettinger, F. F., and Rogers, G. J., Measurement Techniques for High Power Semiconductor Materials and Devices: Annual Report for the Period January 1, 1976 - December 31, 1976, ERDA Report CONS/3800-2, pp. 4-21 (May 1977).

van der Pauw, L. J., A Method of Measuring the Resistivity and Hall Coefficient on Lamella of Arbitrary Shape, *Phillips Research Reports* 13, 1-9 (1958).

Sah, C. T., Forbes, L., Rosier, L. L., Tasch, A. F., Jr., and Tole, A. B., Thermal Emission Rates of Carriers at Gold Centers in Silicon, *Appl. Phys. Letters* 15, 145-148 (1969).

See reference 4, pp. 26-42.

Buehler, M. G., *Semiconductor Measurement Technology*: Microelectronic Test Pattern NBS-3 for Evaluating the Resistivity-Dopant Density Relationship of Silicon, NBS Special Publication 400-22 (June 1976).

Buehler, M. G., and Phillips, W. E., A Study of the Gold Acceptor in a Silicon p^+n Junction and an n-type MOS Capacitor by Thermally Stimulated Current and Capacitance Measurements, *Solid-State Electronics* 19, 777-788 (1978).

Buehler, M. G., *Semiconductor Measurement Technology*: Microelectronic Test Patterns: An Overview, NBS Special Publication 400-6 (August 1974), pp. 4-6, 12-19.

Kumar, R., Ladas, C., and Hudson, G., Characterization of Plasma Etching for Semiconductor Applications, *Solid State Technology* 19 (10), 54-59 (October 1976).

Thomas, R. N., Braggins, T. T., Hobgood, H. M., Takei, W. J., and Nathanson, H. C., Compensation of Extrinsic Si:In Detector Material by Neutron Transmutation of Silicon, *IRIS Specialty Group Meeting on Infrared Detectors*, U.S. Air Force Academy, Colorado, March 22-23, 1977. (Unpublished)

Baron, R., Young, M. H., Baukus, J. P., and Marsh, O. J., Properties of Si:In as an Extrinsic Detector Material, *IRIS Specialty Group Meeting on Infrared Detectors*, U.S. Air Force Academy, Colorado, March 22-23, 1977. (Unpublished)

Scott, M. W., Spectroscopic Investigation of Si:In, *IRIS Specialty Group Meeting on Infrared Detectors*, U.S. Air Force Academy, Colorado, March 22-23, 1977. (Unpublished)

Dearnaley, G., and Northrop, D. C., *Semiconductor Counters for Nuclear Radiations*, 2nd edition, pp. 150, 173 (E. & F. N. Spon Limited, London, 1966).

Kaiser, W., Electrical and Optical Properties of Heat-Treated Silicon, *Phys. Rev.* 105, 1751-1756 (1957).

Kaiser, W., Frisch, H. L., and Reiss, H., Mechanism of the Formation of Donor States in Heat-Treated Silicon, *Phys. Rev.* 112, 1546-1554 (1958).

Standard Test Method for Interstitial Atomic Oxygen Content of Silicon by Infrared Absorption, ASTM Designation F 121, *Annual Book of ASTM Standards*, Part 43 (ASTM, Philadelphia, 1978).

Baker, J. A., Oxygen in Silicon, Paper 82, The Electrochemical Society, Chicago, May 13-18, 1973. (Unpublished)

Johannessen, J. S., Spicer, W. E., and Strausser, Y. E., An Auger Analysis of the SiO_2-Si Interface, *J. Appl. Phys.* 47, 3028-3037 (1976).

Helms, C. R., Garner, C. N., Miller, J., Lindau, I., Schwarz, S., and Spicer, W. E., Studies of Si/SiO_2 Interfaces by Auger Sputter Profiling and Photoelec-

tron Spectroscopy Using Synchrotron Radiation, *Proc. 7th Intern. Vac. Congr. and 3rd Intern. Conf. Solid Surfaces*, Vienna, September 12-16, 1977, pp. 2241-2243.

22. Helms, C. R., Spicer, W. E., and Johnson, N. M., New Studies of the Si-SiO_2 Interface Using Auger Sputter Profiling, *Solid State Communications* 25, 673-676 (1978).

23. Blanc, J., Buiocchi, C. J., Abrams, M. S., and Ham, W. E., The Si/SiO_2 Interface Examined by Cross-Sectional Transmission Electron Microscopy, *Appl. Phys. Letters* 30, 120-122 (1977).

24. DiStefano, T. H., Field Dependent Internal Photoemission Probe of the Electronic Structure of the Si-SiO_2 Interface, *J. Vac. Sci. Tech.* 13, 856-859 (1976).

25. Raider, S. I., and Flitsch, R., Abstract: Stoichiometry of SiO_2/Si Interfacial Regions. I. Ultrathin Oxide Films, *J. Vac. Sci. Tech.* 13, 58 (1976).

26. Ham, W. E., The Measurement and Interpretation of the Electrical Properties of SOS, *Extended Abstracts* for the Fall Meeting of the Electrochemical Society, Las Vegas, Nevada, October 17-22, 1976, pp. 462-464.

27. Mayo, S., and Evans, W. H., Thermodynamic Considerations in the Use of Polysilicon Oxidation Tubes for Clean SiO_2-Film Preparation, *J. Electrochem. Soc.* 125, 106-110 (1978).

28. Mayo, S., and Evans, W. H., Development of Sodium Contamination in Semiconductor Oxidation Atmospheres at 1000°C, *J. Electrochem. Soc.* 124, 780-785 (1977).

29. Dietze, W., Hunt, L. P., and Sawyer, D. H., The Preparation and Properties of CVD-Silicon Tubes and Boats for Semiconductor Device Technology, *J. Electrochem. Soc.* 121, 1112-1115 (1974).

30. Chou, N. J., Osburn, C. M., and van der Meulen, Y. J., Auger Analysis of Chlorine in HCl- or Cl_2-grown SiO_2 Films, *Appl. Phys. Letters* 22, 380-381 (1973).

31. Bunghard, R. A., Gregory, B. L., Gwyn, C. W., and Derbinwich, G. F., Process Dependence of Radiation Effects in CMOS Integrated Circuits, Final Report, Sandia 75-0136, May 1975.

32. Nyyssonen, D., Linewidth Measurement with an Optical Microscope: The Effect of Operating Conditions on the Image Profile, *Appl. Optics* 16, 2223-2230 (1977).

33. Jerke, J. M., Hartman, A. W., Nyyssonen, D., Swing, R. E., Young, R. D., and Keery, W. J., Comparison of Linewidth Measurements on an SEM/Interferometer System and an Optical Linewidth-Measuring Microscope, *Proc. Soc. Photo-Optical Instrum. Engrs.* 100, *Developments in Semiconductor Microlithography II*, 37-45 (1977).

34. Swyt, D. A., and Rosberry, F. W., A Comparison of Some Optical Microscope Measurements of Photomask Linewidths, *Solid State Technology* 20 (8), 70-75 (1977).

35. Nyyssonen, D., Optical Linewidth Measurements on Silicon and Iron-Oxide Photomasks, *Proc. Soc. Photo-Optical Instrum. Engrs.* 100, *Developments in Semiconductor Microlithography II*, 127-134 (1977).

36. Kintner, E. C., Investigations Relating to Optical Imaging in Partially Coherent Light, Ph.D. dissertation, Univ. of Edinburgh, 1975.

37. Kintner, E. C., and Sillitto, R. M., Edge Ringing in Partially Coherent Imaging, *Optica Acta* 24, 591-605 (May 1977).

38. Jerke, J. M., Hartman, A. W., Nyyssonen, D., Rosberry, F. W., Swing, R. E., Swyt, D. A., and Young, R. D., Accurate Linewidth Measurements at the National Bureau of Standards, *Proc. Microelectronics Seminar - Interface '76*, Monterey, California, October 3-5, 1976, pp. 51-59 (Kodak Publication G-47).

39. Buehler, M. G., and Thurber, W. R., A Planar Four-Probe Test Structure for Measuring Bulk Resistivity, *IEEE Trans. Electron Devices* ED-23, 968-974 (1976).

40. Brown, D. M., Connery, R. J., and Gray, P. V., Doping Profiles by MOSFET Deep Depletion C(V), *J. Electrochem. Soc.* 122, 121-127 (1975).

41. David, J. M., and Buehler, M. G., A Numerical Analysis of Various Cross Sheet Resistor Test Structures, *Solid-State Electronics* 20, 535-543 (1977).

42. Buehler, M. G., and Sawyer, D. E., Microelectronic Test Patterns Aid Produc-

tion of Custom ICs, *Circuits Manufacturing* 17 (2), 46-56 (February 1977).

43. Ruthberg, S., Neff, G. R., and Martin, B. D., Radioisotope Hermetic Test Precision, *Proc. 1977 Internat. Microelectronics Symposium*, Baltimore, Maryland, October 24-26, 1977, pp. 131-137.

44. Cassen, B., and Burnham, D., A Method of Leak Testing Hermetically Sealed Components Utilizing Radioactive Gas, *Int. J. Appl. Radiation & Isotopes* 9, 54-59 (1960).

45. MIL-STD-883B, Test Methods and Procedures for Microcircuits, Method 1014.2, Seal, Test Condition B; MIL-STD-750B, Test Methods for Semiconductor Devices, Method 1071.1, Hermetic Seal, Test Condition B.

46. Quate, C. F., A Scanning Acoustic Microscope, *Semiconductor Silicon/1977*, H. R. Huff and E. Sirtl, Eds., pp. 422-430 (Electrochemical Society, Princeton, N.J., 1977).

47. Weglein, R. D., Acoustic Properties of Sputtered Glass at Microwave Frequencies *Appl. Phys. Letters* 29, 277-279 (1976).

48. Hagon, P. J., Milakim, K., and Seymour, R. H., Programmable Acoustic Signal Processing Devices, R & D Technical Report ECOM-05011-1 (February 1974). (AD 775-840)

49. Wilson, R. G., Weglein, R. D., and Bonnel, D. M., Scanning Acoustic Microscope for Integrated Circuit Diagnostics, *Semiconductor Silicon/1977*, H. R. Huff and E. Sirtl, Eds., pp. 431-440 (Electrochemical Society, Princeton, N.J., 1977).

50. Weglein, R. D., Wilson, R. G., and Bonnell, D. M., Scanning Acoustic Microscopy — Application to Fault Detection, *15th Annual Proceedings, Reliability Physics 1977*, Las Vegas, Nevada, April 12-14, 1977, pp. 37-43.

51. Oettinger, F. F., and Gladhill, R. L., Thermal Response Measurements for Semiconductor Device Die Attachment Evaluation, *Technical Digest, 1973 Int. Electron Devices Meeting*, Washington, D.C., December 3-5, 1973, pp. 47-50.

52. Leedy, K. O., Measurement of Transistor Collector-Emitter Saturation Voltage, NBSIR 77-1231 (June 1977).

53. Low Frequency Power Transistors, JEDEC Suggested Standard No. 10, January 1976. (Available from Engineering Department, Electronic Industries Association, 2001 Eye Street, N.W., Washington, D.C. 20006.)

SEMICONDUCTOR TECHNOLOGY PROGRAM STAFF

(on March 31, 1977)

Significant changes in assigned organizational units and telephone numbers have occurred between the end of the reporting period and the issue date of this report. Call the Electron Devices Division, (301) 921-3786, for current information.

Electronic Technology Division

(301) 921-3357

J. C. French, Chief
Miss B. S. Hope*
J. F. Mayo-Wells

Dr. W. M. Bullis, Asst. Chief for Semiconductor Technology
Mrs. M. L. Stream*
Mrs. E. J. Walters*+

Dr. A. H. Sher, Asst. Chief for Operations
R. L. Raybold
Mrs. T. J. Talbott
Mrs. E. Y. Trager*

Semiconductor Characterization Section

(301) 921-3625

Dr. J. H. Albers
F. H. Brewer
Dr. W. M. Bullis, Chief
Mrs. C. A. Cannon
Mrs. E. C. Cohen+
Dr. J. R. Ehrstein
Dr. K. F. Galloway
Mrs. A. D. Glover*
Mrs. F. C. Hoewing*
W. J. Keery
Dr. R. D. Larrabee
Mrs. K. O. Leedy
Dr. S. Mayo
Miss D. R. Ricks
R. I. Scace
H. A. Schafft
L. R. Williams

Semiconductor Processing Section

(301) 921-3541

Dr. M. G. Buehler, Chief
M. R. Doggett
R. L. Frisch
Miss D. L. Hines*
Dr. R. Y. Koyama
J. Krawczyk
T. F. Leedy
Y. M. Liu
R. L. Mattis
D. A. Maxwell
Dr. W. E. Phillips
L. A. Robinson
Dr. T. J. Russell
Dr. D. E. Sawyer
Dr. G. C. Taylor
W. R. Thurber

Electron Devices Section

(301) 921-3621

D. W. Berning
D. L. Blackburn
W. A. Cullins
Mrs. K. E. Dodson*
H. E. Dyson
G. G. Harman
H. K. Kessler
M. D. Nelligan+
Dr. D. B. Novotny
F. F. Oettinger, Chief
G. J. Rogers
S. Rubin
S. Ruthberg

---

* Secretary
+ Part Time

APPENDIX B

SEMICONDUCTOR TECHNOLOGY PROGRAM
PROGRESS REPORTS

A review of the early work leading to this Program is given in Bullis, W. M., Measurement Methods for the Semiconductor Device Industry — A Review of NBS Activity, NBS Tech. Note 511 (December 1969).

Progress reports covering the period July 1, 1968, through June 30, 1973, were published as NBS Technical Notes with the title, Methods of Measurement for Semiconductor Materials, Process Control, and Devices:

Quarter Ending	NBS Tech. Note	Date Issued	NTIS Accession No.
September 30, 1968	472	December 1968	AD 681330
December 31, 1968	475	February 1969	AD 683808
March 31, 1969	488	July 1969	AD 692232
June 30, 1969	495	September 1969	AD 695820
September 30, 1969	520	March 1970	AD 702833
December 31, 1969	527	May 1970	AD 710906
March 31, 1970	555	September 1970	AD 718534
June 30, 1970	560	November 1970	AD 719976
September 30, 1970	571	April 1971	AD 723671
December 31, 1970	592	August 1971	AD 728611
March 31, 1971	598	October 1971	AD 732553
June 30, 1971	702	November 1971	AD 734427
September 30, 1971	717	April 1972	AD 740674
December 31, 1971	727	June 1972	AD 744946
March 31, 1972	733	September 1972	AD 748640
June 30, 1972	743	December 1972	AD 753642
September 30, 1972	754	March 1973	AD 757244
December 31, 1972	773	May 1973	AD 762840
March 31, 1973	788	August 1973	AD 766918
June 30, 1973	806	November 1973	AD 771018

After July 1, 1973, progress reports were issued in the NBS Special Publication 400- subseries with the title, Semiconductor Measurement Technology:

Quarter Ending	NBS Spec Publ.	Date Issued	NTIS Accession No.
September 30, 1973	400-1	March 1974	AD 775919
December 31, 1973 March 31, 1974	400-4	November 1974	COM 74-51222
June 30, 1974	400-8	February 1975	AD/A 005669
September 30, 1974	400-12	May 1975	AD/A 011121
December 31, 1974	400-17	November 1975	AD/A 017523
March 31, 1975 June 30, 1975	400-19	April 1976	PB 251844
September 30, 1975 December 31, 1975	400-25	October 1976	PB 258555
March 31, 1976 June 30, 1976	400-29	April 1977	AD/A 040011
September 30, 1976	400-36	July 1978	PB 283482
December 31, 1976 March 31, 1977	400-38	This report	Not yet available
June 30, 1977 September 30, 1977	400-45	To be issued	Not yet available

After October 1, 1977, progress reports were issued as NBSIRs with the title, Semiconductor Technology Program, Progress Briefs:

Quarter Ending	NBSIR	Date Issued	NTIS Accession No.
December 31, 1977	78-1444	March 1978	PB 284809
March 31, 1978	78-1444-2	July 1978	PB 284478
June 30, 1978	78-1444-3	October 1978	PB 292681
September 30, 1978	79-1591	January 1979	PB 294846
December 31, 1978	79-1591-2	March 1979	PB 298063
March 31, 1979	79-1591-3	June 1979	PB 298064
June 30, 1979	79-1591-4	August 1979	Not yet available

APPENDIX C

COMPUTATION OF DARK-FIELD LINE IMAGES

E. C. Kintner*

The calculation of the image intensity distribution in a partially coherent imaging system is, in general, a difficult task. It can be simplified by describing the system in terms of a dimensionless abstract model which takes advantage of the properties of the Fourier transform and by making certain particular assumptions about the form of the object being imaged. The method outlined here has been described in some detail by Kintner [C-1] and discussed elsewhere by Hopkins [C-2] and by Ichioka and Suzuki [C-3].

Let positions in the object plane of a microscope be described by the dimensionless cartesian coordinates:

$$x = \frac{\rho_o}{\lambda} \bar{x} \tag{C-1a}$$

and

$$y = \frac{\rho_o}{\lambda} \bar{y} , \tag{C-1b}$$

where the geometrical coordinates are given by $\bar{x}$ and $\bar{y}$, ρ_o is the numerical aperture of the objective, and λ is the mean wavelength of the (quasi-monochromatic) illumination. Points in the image plane conjugate to (x,y) in the object plane are described by the same coordinates (x,y). Similarly, points in the pupil plane can be described by coordinates

$$\xi = \bar{\xi}/\rho_o \tag{C-2a}$$

and

$$\eta = \bar{\eta}/\rho_o , \tag{C-2b}$$

where $\bar{\xi}$ and $\bar{\eta}$ are the geometrical coordinates and again ρ_o is the numerical aperture. Where the Fraunhofer diffraction theory is valid, the coordinate system (ξ,η) corresponds to the Fourier-transform plane of the coordinate system (x,y).

The image spatial frequency spectrum $\mathcal{I}(\xi,\eta)$ is defined to be the Fourier transform of the image intensity distribution I(x,y) through the equations:

$$\mathcal{I}(\xi,\eta) = \iint_{-\infty}^{\infty} I(x,y) \exp\{2\pi i(x\xi + y\eta)\}\, dx\, dy \tag{C-3a}$$

and

$$I(x,y) = \iint_{-\infty}^{\infty} \mathcal{I}(\xi,\eta) \exp\{-2\pi i(x\xi + y\eta)\}\, d\xi\, d\eta . \tag{C-3b}$$

Similarly, if the complex amplitude transmittance (or reflectance) of the object is given by the function F(x,y), its spatial-frequency spectrum is given by the Fourier transform

---

* NBS-NRC Postdoctoral Research Associate, NBS Optics and Micrometrology Section, Mechanics Division.

$$F(\xi,\eta) = \iint_{-\infty}^{\infty} F(x,y) \exp\left\{2\pi i(x\xi + y\eta)\right\} dx\, dy \ . \qquad \text{(C-4)}$$

The imaging properties of the objective lens system may be described by the amplitude point-spread function K(x,y), whose Fourier transform is given by

$$K(\xi,\eta) = \iint_{-\infty}^{\infty} K(x,y) \exp\left\{2\pi i(x\xi + y\eta)\right\} dx\, dy \ . \qquad \text{(C-5)}$$

The function $K(\xi,\eta)$ has a special physical significance, because in Fourier optics it may be identified with the pupil function of the optical system. In the dimensionless coordinates used here, the radius $\rho = (\xi^2 + \eta^2)^{1/2} = 1$ corresponds to the edge of the optical pupil and simultaneously corresponds to the limiting spatial frequency detected by the objective lens system under coherent illumination.

Finally, in the presence of stationary partially coherent illumination, the mutual intensity of the illumination in the object plane may be described by the function J(x,y). Its Fourier transform

$$J(\xi,\eta) = \iint_{-\infty}^{\infty} J(x,y) \exp\left\{2\pi i(x\xi + y\eta)\right\} dx\, dy \qquad \text{(C-6)}$$

is called the "effective source," and, where certain conditions are met, it corresponds to the intensity distribution in the aperture of the condensing-lens system. Thus, for example, in a microscope system with matched numerical apertures between the objective and the condenser, the effective source is a uniform distribution which cuts off at the limiting radius $\rho = 1$.

With these definitions, it is possible to show that the image spatial-frequency spectrum produced by a specified optical system is given by the equation

$$I(\xi,\eta) = \iint_{-\infty}^{\infty} T(\xi+\xi',\eta+\eta';\xi',\eta')F(\xi+\xi',\eta+\eta')F^*(\xi',\eta')d\xi'd\eta' \ , \qquad \text{(C-7)}$$

where

$$T(\xi_1,\eta_1;\xi_2,\eta_2) = \iint_{-\infty}^{\infty} J(\xi'',\eta'')K(\xi_1+\xi'',\eta_1+\eta'')K^*(\xi_2+\xi'',\eta_2+\eta'')\, d\xi''\, d\eta'' \ . \qquad \text{(C-8)}$$

In eqs (C-7) and (C-8) the asterisk denotes complex conjugation. The function $T(\xi_1,\eta_1;\xi_2,\eta_2)$, called the transmission cross-coefficient [C-4], characterizes the complete optical system including condenser and objective. When the illumination is incoherent, it can be shown that the function T becomes the optical transfer function; similarly, for coherent illumination, the function becomes the product of the two pupil functions K and K^*. Therefore, eq (C-7) combines the attributes of the optical system with the attributes of the object in a manner which is both intuitively meaningful and practically useful.

If the object function varies in one dimension only (e.g., a straight edge), eqs (C-7) and (C-8) may be simplified into a one-dimensional form:

$$I(\xi) = \int_{-\infty}^{\infty} T(\xi+\xi',\xi')F(\xi+\xi')F^*(\xi')\, d\xi' \ , \tag{C-9}$$

where

$$T(\xi_1,\xi_2) = \iint_{-\infty}^{\infty} J(\xi'',\eta'')K(\xi+\xi'',\eta'')K^*(\xi_2+\xi'',\eta'')\, d\xi''\, d\eta'' \ . \tag{C-10}$$

Equation (C-10) still allows for a two-dimensional optical system.

Equation (C-9) is further simplified if the one-dimensional object is periodic (e.g., a grating). Then the object may be represented by a Fourier series, whose transform is a distribution of delta functions. If the periodic function is even, then the Fourier series consists of cosine terms only. Thus, an even periodic function with period $P = 1/\xi_p$ may be represented by the Fourier series

$$F(x) = \sum_{n=-\infty}^{\infty} a_n \cos(2\pi n\xi_p x) \ , \tag{C-11}$$

with $a_n = a_{-n}$ and whose Fourier transform is simply

$$F(\xi) = \sum_{n=-\infty}^{\infty} a_n \delta(n\xi_p - \xi) \ . \tag{C-12}$$

The coefficients $\{a_n\}$ are complex when the object function includes phase variations. (The infinite limits on the series simplify the presentation of the next step.)

Equation (C-12) may be inserted into eq (C-9), which after simplification becomes

$$\begin{aligned} I(\xi) &= \sum_{n=-\infty}^{\infty} \left\{ a_n a_o^* T(n\xi_\rho;0) + \sum_{n'=1}^{\infty} [a_{n+n'}, a^*_{n'}, T((n+n')\xi_p; n'\xi_p) \right. \\ &\quad \left. + a_{n-n'}, a^*_{-n'}, T((n-n')\xi_p; -n'\xi_p)] \right\} \delta(n\xi_p - \xi) \\ &= \sum_{n=-\infty}^{\infty} c_n \delta(n\xi_p - \xi) \ , \end{aligned} \tag{C-13}$$

with $c_n = -c_{-n}$. Therefore, the intensity in the image plane is given by

$$I(x) = \sum_{n=-\infty}^{\infty} c_n \cos(2\pi n\xi_p x) \ . \tag{C-14}$$

Since the intensity distribution in the image is necessarily real, the coefficients c_n are also real. When the series in eq (C-14) is evaluated, only two cosines must be calculated

directly; the remainder of the harmonics may be calculated by using a simple recurrence relation for the cosine function.

The use of a periodic object greatly simplifies the calculation of the intensity distribution in partially coherent imaging. In general, the calculation of the image intensity requires three separate integrations: (1) the integration over the source as given by eq (C-8) to determine the performance of the optical system; (2) the integration over the object spectrum as given by eq (C-7) to determine the intensity spectrum; and (3) the integration over the intensity spectrum as given by eq (C-3b) (the inverse Fourier transform) to obtain the intensity distribution itself. In practical calculations, these integrations can be intolerably tedious. The above analysis shows that with a one-dimensional periodic object, two of the three integrations, eqs (C-3b) and (C-7), reduce to discrete summations, eqs (C-13) and (C-14), thus eliminating the problems of convergence associated with numerical integration. Although infinite limits are specified for the summations in eqs (C-13) and (C-14), the function $T(\xi_1;\xi_2)$ vanishes for large values of the arguments, due to the finite extent of the pupil function and the source function. Therefore, the summations in eqs (C-13) and (C-14) may be truncated at predetermined limits without loss of accuracy.

So great are the advantages of using a periodic object that it is worthwhile to express even a non-periodic object in terms of a periodic model. This is readily accomplished if a large period is chosen so that the object is effectively isolated and does not interfere with its periodic neighbors. The periodic model may be compared directly with the non-periodic object to verify the accuracy of the approximation. It should be emphasized that this periodic approximation, which is so easily checked, is, in fact, the only approximation in the imaging calculation; all the other steps of the calculation are exact.

In practice, the image plane is sampled by a scanning slit, which must be convolved with the intensity distribution to obtain the distribution recorded by the scanning system. Since convolution in the image plane corresponds to multiplication in the pupil plane, it is convenient to multiply the intensity spectrum in eq (C-13) by the Fourier transform of the slit Thus, the intensity spectrum actually observed is

$$I_s(\xi) = S(\xi) \cdot I(\xi) = \frac{\sin(\pi w \xi)}{\pi w \xi} \cdot I(\xi) \ , \tag{C-15}$$

where w is the full width of the scanning slit in dimensionless coordinates.

Therefore, the complete calculation for the partially coherent imaging process is characterized by the equation

$$I_s(x) = c_o + 2 \sum_{n=1}^{\infty} c_n s_n \cos(2\pi n \xi_p x) \ , \tag{C-16}$$

where

$$c_n = a_n a_o^* T(n\xi_p;0) + \sum_{n'=1}^{\infty} a_{n+n'} a_{n'}^* T((n+n')\xi_p;n'\xi_p) + a_{n-n'} a_{n'}^* T((n-n')\xi_p;-n'\xi_p) \tag{C-17}$$

and

$$s_n = \frac{\sin(n\pi w \xi_p)}{n\pi w \xi_p} \ . \tag{C-18}$$

A periodic rectangular waveform as shown in figure C-1, which characterizes a periodic line object, is given by a Fourier series, eq (C-11), with coefficients

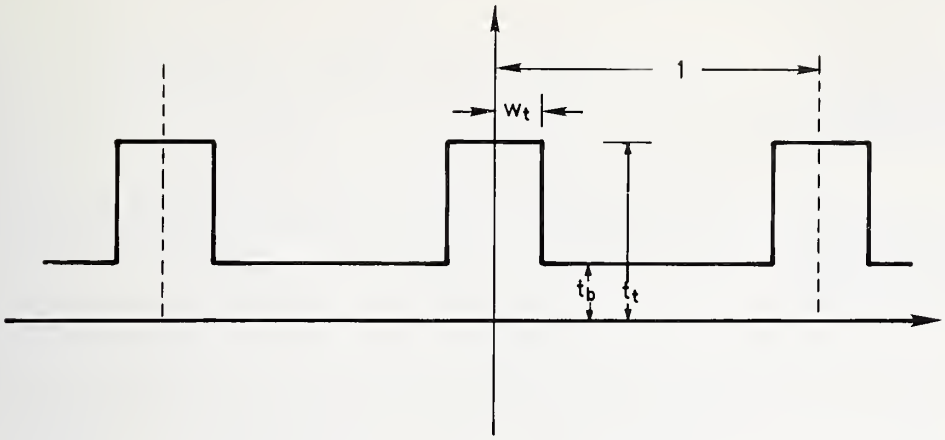

Figure C-1. A periodic rectangular waveform.

$$a_o = t_b + 2(t_t - t_b)\, w_t \tag{C-19a}$$

nd

$$a_n = \frac{(t_t - t_b)}{\pi} \cdot \frac{\sin(2\pi n w_t)}{n} . \tag{C-19b}$$

hen $w_t < 0.1$, each line is effectively isolated and behaves as a single line object. The uantities t_t and t_b may, of course, be complex to model a line object with phase variation.

lthough the procedures described above simplify the calculation of the image intensity distribution in partially coherent imaging, the integration for the function T describing the ptical system, eq (C-8) or eq (C-10), remains a formidable problem. It will be noted that his integration represents a generalized convolution of the source function J with the objective pupil function K. Where the source and objective apertures are circular and the objective pupil includes aberrations, this convolution has no simple solution and implies an xtremely tedious numerical integration. To avoid this, two alternative compromises are vailable.

irst, where the source aperture is small (less than the objective aperture), it is possible o reduce the integration to one dimension rather than two, in which case numerical integration becomes feasible. It is thus possible to test the effects of aberrations such as defocusing and spherical aberration. As the source size approaches the size of the objective perture, this model becomes less reliable.

econd, if all variations in the source aperture and objective pupil are suppressed (i.e., o aberrations), then the two-dimensional integration corresponds to the generalized convolution of three uniform circles; that is, the problem reduces to finding the area of the mutual intersection of the source aperture and the shifted objective pupils (see fig. C-2 and ef. [C-4]). This is a fairly strenuous exercise in logic and geometry, but it yields an efficient algorithm for the optical performance function T.

he above method may be extended to systems with annular sources (see fig. C-3). First, he function T_O is computed for a system including a source with radius equal to the outer adius of the annulus. Second, the function T_I is computed for a source with radius equal o the inner radius of the annulus. Then the difference between T_O and T_I yields the value

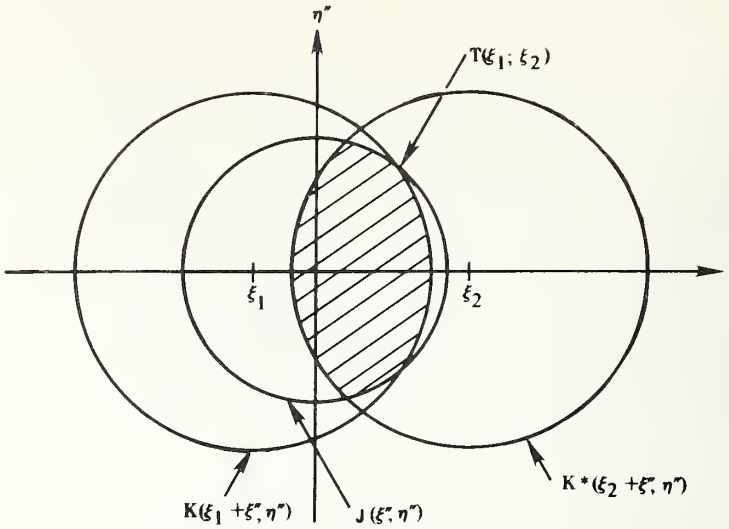

Figure C-2. The convolution for the transmission cross-coefficient.

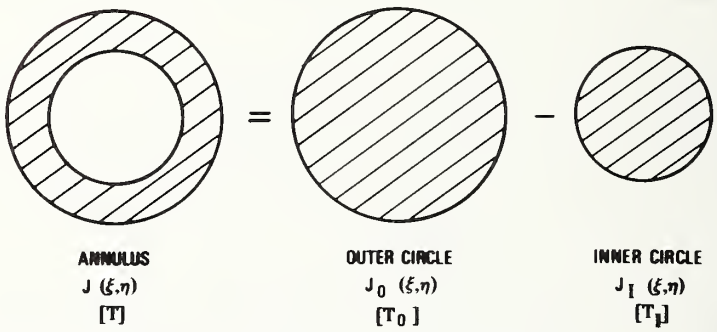

Figure C-3. An annular source obtained using two circular sources.

of T corresponding to the annular source. This method is entirely analogous to the method used to calculate the diffraction pattern of an annular aperture [C-5].

References:

C-1. Kintner, E. C., Investigations Relating to Optical Imaging in Partially Coherent Light Doctoral dissertation, University of Edinburgh, 1975.

C-2. Hopkins, H. H., On the Diffraction Theory of Optical Images, *Proc. Roy. Soc.* A217, 408 432 (1953).

C-3. Ichioka, Y., and Suzuki, T., Image of a Periodic Complex Object in an Optical System under Partially Coherent Illumination, *J. Opt. Soc. Am.* 66, 921-932 (1976).

C-4. Born, W., and Wolf, E., *Principles of Optics*, fifth edition, pp. 530-532 (Pergamon Press Inc., Elmsford, N.Y., 1975).

C-5. *Ibid.*, pp. 416-417.

NBS-114A (REV. 9-78)

U.S. DEPT. OF COMM. BIBLIOGRAPHIC DATA SHEET	1. PUBLICATION OR REPORT NO. Spec. Publ. 400-38	2. Gov't. Accession No.	3. Recipient's Accession No.

4. TITLE AND SUBTITLE

Semiconductor Measurement Technology: Progress Report, October 1, 1976 to March 31, 1977

5. Publication Date November 1979

6. Performing Organization Code

7. AUTHOR(S)

W. M. Bullis, Editor

8. Performing Organ. Report No.

9. PERFORMING ORGANIZATION NAME AND ADDRESS

NATIONAL BUREAU OF STANDARDS
DEPARTMENT OF COMMERCE
WASHINGTON, DC 20234

10. Project/Task/Work Unit No.

11. Contract/Grant No. See item 15.

12. SPONSORING ORGANIZATION NAME AND COMPLETE ADDRESS *(Street, City, State, ZIP)*

NBS - Washington, DC 20234; SSPO - Washington, DC 20376; DNA - Washington, DC 20305; ARPA - 1400 Wilson Boulevard, Arlington, VA 22209; ERDA - Washington, DC 20545; Naval Ocean Systems Center,

13. Type of Report & Period Covered Interim: Oct. 1, 1976 to March 31, 1977

14. Sponsoring Agency Code

15. SUPPLEMENTARY NOTES

ARPA Order 2397, Program Code 7D10; DNA IACRO 77-809; SSPO Order N0016476WR70036, Code SP-23; ERDA Task Order A021-EES; Naval Ocean Systems Center Order N0095377M009005.

☐ Document describes a computer program; SF-185, FIPS Software Summary, is attached.

16. ABSTRACT *(A 200-word or less factual summary of most significant information. If document includes a significant bibliography or literature survey, mention it here.)*

This progress report describes NBS activities directed toward the development of methods of measurement for semiconductor materials, process control, and devices. Both in-house and contract efforts are included. The emphasis is on silicon device technologies. Principal accomplishments during this reporting period included (1) refinement and extension of the analysis of the nondestructive, photovoltaic method for measuring radial resistivity variation of silicon slices; (2) development of a donor-addition technique for testing for the presence of X-levels in indium-doped silicon; (3) development of a precision, wet chemical etching procedure for use in conjunction with x-ray photoelectron spectroscopy for profiling silicon dioxide-silicon interfaces; (4) completion of thermodynamic calculations of equilibrium sodium density in oxidation atmospheres contained in polycrystalline silicon tubes; (5) initial extensions of the line-width measurement procedure to partially transparent and reflecting specimens and to submicrometer dimensions; and (6) completion of the development of a test pattern for characterizing a large-scale-integration, silicon-on-sapphire process. Also reported is other ongoing work on materials characterization by electrical and physical analysis methods, materials and procedures for wafer processing, photolithography, test patterns, and device inspection and test procedures. Supplementary data concerning staff and publications are included as appendices.

17. KEY WORDS *(six to twelve entries; alphabetical order; capitalize only the first letter of the first key word unless a proper name; separated by semicolons)*

Auger electron spectroscopy; die attachment; electrical properties; electronics; hermeticity; indium-doped silicon; infrared reflectance; integrated circuits; line-width measurements; oxidation; photolithography; photovoltaic method; power-device grade silicon; radioisotope leak test; resistivity variations; resistors, sheet; scanning acoustic microscope; semiconductor materials; semiconductor process control; silicon; silicon dioxide; silicon-on-sapphire; sodium contamination; test patterns; test structures; thermally stimulated current and capacitance; transistors; ultraviolet reflectance; $V_{CE(SAT)}$; x-ray photoelectron spectroscopy.

18. AVAILABILITY

☒ Unlimited

☐ For Official Distribution. Do Not Release to NTIS

☒ Order From Sup. of Doc., U.S. Government Printing Office, Washington, DC 20402, SD Stock No. SN003-003-02139-3

☐ Order From National Technical Information Service (NTIS), Springfield, VA. 22161

19. SECURITY CLASS (THIS REPORT) UNCLASSIFIED

20. SECURITY CLASS (THIS PAGE) UNCLASSIFIED

21. NO. OF PRINTED PAGES 95

22. Price $3.50

USCOMM-DC

NBS TECHNICAL PUBLICATIONS

PERIODICALS

JOURNAL OF RESEARCH—The Journal of Research of the National Bureau of Standards reports NBS research and development in those disciplines of the physical and engineering sciences in which the Bureau is active. These include physics, chemistry, engineering, mathematics, and computer sciences. Papers cover a broad range of subjects, with major emphasis on measurement methodology and the basic technology underlying standardization. Also included from time to time are survey articles on topics closely related to the Bureau's technical and scientific programs. As a special service to subscribers each issue contains complete citations to all recent Bureau publications in both NBS and non-NBS media. Issued six times a year. Annual subscription: domestic $17; foreign $21.25. Single copy, $3 domestic; $3.75 foreign.

NOTE: The Journal was formerly published in two sections: Section A "Physics and Chemistry" and Section B "Mathematical Sciences."

DIMENSIONS/NBS—This monthly magazine is published to inform scientists, engineers, business and industry leaders, teachers, students, and consumers of the latest advances in science and technology, with primary emphasis on work at NBS. The magazine highlights and reviews such issues as energy research, fire protection, building technology, metric conversion, pollution abatement, health and safety, and consumer product performance. In addition, it reports the results of Bureau programs in measurement standards and techniques, properties of matter and materials, engineering standards and services, instrumentation, and automatic data processing. Annual subscription: domestic $11; foreign $13.75.

NONPERIODICALS

Monographs—Major contributions to the technical literature on various subjects related to the Bureau's scientific and technical activities.

Handbooks—Recommended codes of engineering and industrial practice (including safety codes) developed in cooperation with interested industries, professional organizations, and regulatory bodies.

Special Publications—Include proceedings of conferences sponsored by NBS, NBS annual reports, and other special publications appropriate to this grouping such as wall charts, pocket cards, and bibliographies.

Applied Mathematics Series—Mathematical tables, manuals, and studies of special interest to physicists, engineers, chemists, biologists, mathematicians, computer programmers, and others engaged in scientific and technical work.

National Standard Reference Data Series—Provides quantitative data on the physical and chemical properties of materials, compiled from the world's literature and critically evaluated. Developed under a worldwide program coordinated by NBS under the authority of the National Standard Data Act (Public Law 90-396).

NOTE: The principal publication outlet for the foregoing data is the Journal of Physical and Chemical Reference Data (JPCRD) published quarterly for NBS by the American Chemical Society (ACS) and the American Institute of Physics (AIP). Subscriptions, reprints, and supplements available from ACS, 1155 Sixteenth St., NW, Washington, DC 20056.

Building Science Series—Disseminates technical information developed at the Bureau on building materials, components, systems, and whole structures. The series presents research results, test methods, and performance criteria related to the structural and environmental functions and the durability and safety characteristics of building elements and systems.

Technical Notes—Studies or reports which are complete in themselves but restrictive in their treatment of a subject. Analogous to monographs but not so comprehensive in scope or definitive in treatment of the subject area. Often serve as a vehicle for final reports of work performed at NBS under the sponsorship of other government agencies.

Voluntary Product Standards—Developed under procedures published by the Department of Commerce in Part 10, Title 15, of the Code of Federal Regulations. The standards establish nationally recognized requirements for products, and provide all concerned interests with a basis for common understanding of the characteristics of the products. NBS administers this program as a supplement to the activities of the private sector standardizing organizations.

Consumer Information Series—Practical information, based on NBS research and experience, covering areas of interest to the consumer. Easily understandable language and illustrations provide useful background knowledge for shopping in today's technological marketplace.

Order the **above** *NBS publications from: Superintendent of Documents, Government Printing Office, Washington, DC 20402.*

Order the **following** *NBS publications—FIPS and NBSIR's—from the National Technical Information Services, Springfield, VA 22161.*

Federal Information Processing Standards Publications (FIPS PUB)—Publications in this series collectively constitute the Federal Information Processing Standards Register. The Register serves as the official source of information in the Federal Government regarding standards issued by NBS pursuant to the Federal Property and Administrative Services Act of 1949 as amended, Public Law 89-306 (79 Stat. 1127), and as implemented by Executive Order 11717 (38 FR 12315, dated May 11, 1973) and Part 6 of Title 15 CFR (Code of Federal Regulations).

NBS Interagency Reports (NBSIR)—A special series of interim or final reports on work performed by NBS for outside sponsors (both government and non-government). In general, initial distribution is handled by the sponsor; public distribution is by the National Technical Information Services, Springfield, VA 22161, in paper copy or microfiche form.

BIBLIOGRAPHIC SUBSCRIPTION SERVICES

The following current-awareness and literature-survey bibliographies are issued periodically by the Bureau:

Cryogenic Data Center Current Awareness Service. A literature survey issued biweekly. Annual subscription: domestic $25; foreign $30.

Liquefied Natural Gas. A literature survey issued quarterly. Annual subscription: $20.

Superconducting Devices and Materials. A literature survey issued quarterly. Annual subscription: $30. Please send subscription orders and remittances for the preceding bibliographic services to the National Bureau of Standards, Cryogenic Data Center (736) Boulder, CO 80303.

U.S. DEPARTMENT OF COMMERCE
National Bureau of Standards
Washington, D.C. 20234